ANALYSIS OF LAMINATED CURVED BEAM WITH AND WITHOUT DEFECTS AND IMPERFECTIONS

by

WEI-TSEN LU

DISSERTATION

Submitted in partial fulfilment of the requirements

for the degree of Doctor of Philosophy in Aerospace Engineering at

The University of Texas at Arlington

August, 2019

Supervising Committee:

Dr. Endel V. Iarve, Supervising Professor

Dr. Erian Armanios

Dr. Seiichi Nomura

Dr. Andrey Beyle

Dr. Ashfaq Adnan

Dr. Shih-Ho Chao

Abstract

ANALYSIS OF LAMINATED CURVED BEAM WITH AND WITHOUT DEFECTS AND IMPERFECTIONS

Wei-Tsen Lu, PhD

The University of Texas at Arlington, 2019

Supervising Professor: Endel V. Iarve

Several studies have focused on the modeling and response characterization of composite structural members, with particular emphasis on composite curved beams. The class of curved beam is explored to determine mechanical response in primary aerospace structural applications. The present work focuses on developing analytical closed-form solutions for investigating composite curved beams with and without fiber waviness and delamination. The present work can efficiently characterize the structural behavior of composite curved beams under bending.

This work shows the development of a novel mathematical approach to predict structural performance by investigating axial stiffness, bending stiffness with consideration of shear deformation in composite curved beam. A modified Classical Lamination Theory (CLT) is proposed by considering cross-section effect of a beam. Finite Element (FE) analysis is employed to compare against the analytical results. Parametric study is conducted to investigate effects of radius of composite curved beam versus axial and bending stiffness. Ply stress variations are also studied for a composite curved beam under bending. The stress results obtained from numerical analysis show excellent agreement in comparison with present approach.

The present work also studied fiber waviness effect in composite curved beam. Fiber waviness has an adverse influence on the mechanical properties. The tensile, compressive strength, and fatigue life degrade significantly due to fiber waviness. The proposed method takes into account the degraded stiffness properties by considering various amplitude-length ratio of fiber waviness presented in curved beam. It can be concluded that for a composite curved beam with fiber waviness, the effect of stiffness reduction significantly increases if the amplitude-length ratio is between 0.6 and 1.0. Moreover, the present work provides an analytical solution to predict the interlaminar radial stress σ_r if fiber waviness is present. The analytical results show excellent agreement with results obtained from numerical analysis.

Delamination is considered as one of the dominant failure factor in composite and leads to substantial stiffness loses. The present work provides an analytical method for calculation of the strain energy release rate (ERR) of a delamination in a composite curved beam. In the present approach, we allow for a delamination which is not symmetric with respect to the middle span of the composite curved beam and can be located at any arbitrary interface.

ACKNOWLEDGEMENTS

This work could not have been done without supports and encouragement of numerous people to whom I would like to express my appreciation.

First, I would like to express my profoundly gratitude to my advising Professor Dr. Endel V. Iarve for devoting his invaluable time to guide me with constant encouragement. I am indebted for plentiful enlightening discussions and inspiring critiques, which makes me become a better researcher. I am also grateful to my distinguished professor and mentor, Dr. Erian Armanios, who always gives me great support and encouragement in every aspect. The knowledge I could always count on him and his support that made UT-Arlington feel like home. I am deeply appreciated his unconditional help and guide. I would also like to express my sincere appreciations to my committee members Dr. Seiichi Nomura and Dr. Ashfaq Adnan, for their helps and assistances not only in Ph.D. but the master program as well. In addition, the time and valuable feedback from Dr. Andrey Beyle and Dr. Shih-Ho Chao so generously provided has been instrumental in the successful completion of my research. I want to express my sincere appreciation to Dr. Stefan Dancila, who gave me unconditional support when I need help.

I would like to thank the entire faculty and staff of Mechanical and Aerospace Engineering Department for their helps. Special thanks go to Lanie, Flora, Ayesha, Kathy, Janet, Catherine, Wendy and Danette.

I would like to express my endless love to my parents and my best brother. This honor goes to my entire family.

I would like to thank my friends, Ray, Hari, Scott, and Kevin for their assistance in the dissertation and dedicated technical support.

I would like to express my special acknowledgement to my wife, Jean. Without her understanding and supports, this dissertation would not have been completed.

Finally, I want to express my deepest acknowledge to my mentor, Dr. Wen S. Chan. Without him, I couldn't pursue PhD at the beginning. I learned many things from him. He corrected my weakness and accompanied me, made my life colorful day after day. I will always consider him as my "Academic Father". He was a memorable person and everybody will miss him. How humble he was, how accomplished he was. I will make you proud because I am proud to say "It's my honor for having you to be my teacher". Thank you, thank you and thank you.

Table of Contents

List of Figures

List of Table

Chapter 1

LITERATURE SURVEY

1-1 Composite Curved Beam

The well-known beam theory for an isotropic beam is Euler-Bernoulli beam [1], which effectively demonstrates behavior of a beam under axial forces and bending. It is assumed that the section of the plane remains plane and perpendicular to the longitudinal axis after deformation. On the other hand, Timoshenko beam theory [2] takes shear deformation into account where the cross-section of the plane is no longer perpendicular to the longitudinal axis of the beam after deformation. Beams can be divided into two groups, straight and curved. The isotropic curved beam contains tangential σ_θ, radial σ_r, and shearing stress $\tau_{r\theta}$. The exact solution is derived from Timoshenko and Goodier [3] and Oden [4]. They provided the equilibrium equations for pressure on the circular boundary under axial loading and bending moment. However, among these studies, the formulas were developed to determine stresses for curved members by using isotropic material properties only.

In CLT, the stiffness of the composite laminate is approximated by an equivalent homogenized material property through the thickness of the entire beam. However, the through the thickness direction is ignored therefore it cannot be applied to composite curved beam because of lacking interlaminar stress. Therefore, Lekhnitskii [5] provided closed-form methods for obtaining transverse interlaminar stress in a composite curved beam under end bending moment and shearing load. Later on, Chung and Harold [6] provided the closed-form method for composite curved beam under axial loading. Therefore, the maximum delamination stress along radial direction $\sigma_{r_{max}}$ can be calculated by equating $\frac{d\sigma_r}{dr}$ zero [7, 8].

However, for Lekhnitskii's approach, pure bending and axial forces applied at the end are assumed so the boundary conditions are different from the composite curved beam. Consequently, the extension of the Lekhnitskii's approaches was presented [9-11]. Shenoi and Wang [9] concluded that the stacking sequence and radius of curvature have significant effects on delamination and radial stress, which is similar to [12, 13]. Vibrational formulations of beam problems are of two types [14]. For the first type, governing equations are derived by using force or moment balance. The second type is based on varied formulation and energy measure of a structure to formulate the governing equation. Energy-based method is extensively applied in nonlinear analysis of structural members. The strain energy for composite curved beam has been studied in [15-17]. The strain energy and the kinetic energy for the entire beam including rotary inertia are presented by [15], and the strain energy based on thin cross-section including high order terms in the binomial expansion are presented by [17]. Several authors also studied torsion effect for composite curved beam [18-20]. However, among these researches, the effect of stiffness under Narrow Beam (NB) assumption for composite curved beam has not been studied.

1-2 Fiber Waviness

Fiber waviness is considered a common imperfection occurring in the manufacturing process of composite structures especially for thick composite laminates of compound curvature and in the region where the thickness is changing [21]. The imperfection is caused by non-uniform distribution of pressure and mismatch of thermal expansion (CTE) between tooling material, matrix, and fiber.

This will cause longitudinal and transverse stresses in composite, including higher matrix contraction and fiber buckling as stated by Kantharaju [22]. Parameters on developing fiber waviness have been studied by Kugler and Moon [23]. They concluded that the influence of holding cure temperature is insignificant, but the cooling rate will affect the severity and the quantity of fiber waviness.

The concept of elastic moduli reduction for initial distortions of the unidirectional reinforcing layers was first provided by Bolotin [31]. In his analysis, Kirchhoff hypothesis was used to describe the deformation of thin layers or slightly twisted plates with initial irregulations. In connection with the study of layered reinforced media with random initial irregularities, reduction on the modulus of elasticity in tension along the fibers of unidirectional glass-reinforced plastics (GRP) is proposed by Tarnopol'skii et al. [32]. The shape of fiber irregularities is assumed to be a sinusoidal function. Bažant [33] advanced their approach by taking into account changes in wave amplitude due to radial forces. Three ideal cases of unidirectional fiber distributions were discussed. The first one is parallel, uniformly distributed fibers with sinusoidal curvature. The second one is not strictly parallel distributed fibers with sinusoidal curvature. The third one is when fiber waviness are equal in amplitude but in opposite directions.

Extensive investigations of stiffness loss due to fiber waviness was conducted in [34-36]. Lo and Chim [37] predicted the compressive strength of unidirectional composite with fiber waviness. Adams and Hyer [38] experimentally investigated multi-directional composite laminates under static compression loading. They observed that severe waviness induced a static strength reduction of 36 %, although the fiber waviness occurred in 0° ply and accounted for only 20 % of the load-carrying capacity of the laminate. Rai et al. [39] numerically investigated lamina modulus as a function of fiber waviness, which is similar to [40-43]. They concluded that fiber waviness, which occurs in 0° ply has significant influence on stiffness reduction. If fiber waviness occurs in $\pm 45°$ ply, the influence in stiffness reduction is more pronounced in torsional cases than bending cases.

Fiber waviness can occur in either in-plane or out-of-plane for a laminated beam [44]. The effects of out-of-plane fiber waviness for a lamina were further investigated by Hsiao and Daniel [45-47]. Three types of fiber waviness are considered including uniform, graded and localized fiber waviness. They concluded that tensile and compressive elastic properties and nonlinear behavior in composite materials can be significantly influenced by fiber waviness. Several researchers applied numerical method for investigating effects of fiber waviness. Seon [48] studied tape composite with fiber waviness by linear and nonlinear FE analysis. The nonlinear interlaminar stress-strain relations can improve the delamination onset prediction. He observed that the failure load for a rectangular tape with small amplitude fiber waviness under tension is higher compared to fiber waviness with large amplitude. Nikishkov et al. [49] conducted a numerical model to investigate progressive fatigue damage in composites with fiber waviness. However, most of analytical researches is not focused on out-plane fiber waviness for a laminated composite beam. Therefore, the object of this research is to develop a feasible and efficient approach to analyze composite curved beam with out-of-plane fiber waviness.

There is a type of composites where fiber waviness is built-in by design, namely textile [50] and braided composites [51]. The fiber waviness leads to same general property effects such as modulus and strength reduction [52-55]. However, it allows to produce composites with greatly improved properties in the transverse direction and, in the case of 3D reinforcement, also in the out-of-plane direction. A detailed review of the respective literature is beyond the scope of this work. It is worth mentioning that application of analytical methods has led to accurate estimates of stiffness properties of such materials as a function of fiber angulation and is addressed in a number of works including in [56-58].

1-3 Composite Curved Beam with Delamination

Three principle failure models are often to be found in a laminated composite – fiber failure, matrix cracking, and delamination [59]. Delamination is considered as one of the dominant failure factors in composites and leads to substantial stiffness loses [60, 61], and local compressive failure due to instability [62]. Delamination is driven by interlaminar stresses, *Interlaminar Shear Stress* (ILSS) and *Interlaminar Tensile Stress* (ILTS). When ILSS or ILNS grows over the critical value given from the material, the delamination starts to initiate and propagate. There are several affects have impacts on interlaminar stresses, including stacking sequence, Poisson's ratio mismatch, ply thickness [63], and free-edge effect [64-66]. The initiation of delamination usually occurs at the location with the highest ILTS.

Another essential factor to describe initiation and propagation of delamination is strain ERR. Double Cantilever Beam (DCB) test (ASTM D5228) [67] is the method for measuring Mode-I fracture toughness, and End-Notched Flexure (ENF) test (ASTM WK22949) [68] is the method for measuring Mode-II fracture toughness experimentally. Mode-I and Mode-II delamination can be also predicted accurately by analytical methods based on the plate theory and bridge-crack models [69-71]. Due to limit cases can be applied for pure Mode-I and Mode-II fracture, a mixed-mode approach based on non-linear and Timoshenko first-order shear theory is developed [72] for a straight beam. Considering a beam with an initial curvature, Lu et al. [73] considered a circumferential crack in composite curved beam under bending.

Superposition method of a perfect curved beam under bending and a cracked curved beam subjected to opening radial stress acting on the crack interface was applied. They assumed that if the crack is small and locates in the middle of the beam, the crack is considered in pure Mode-I. Based on their observations, the strain ERR reaches the maximum when the half crack angle approaches to $45°$, and the strain ERR decreases monotonically when the crack location approaches to outer curvature of the curved beam. Moreover, they studied the strain ERR for a large crack using FE analysis. They found that Mode-II becomes dominant when the crack tip reaches to $90°$. This conclusion is similar than the conclusion made by [74].

Roberta and Brian [75] developed an analytical approach based on bridged-crack model which deals with mixed-mode delamination in composite curved beam under bending. In their model, the strain ERR is calculated by considering the J-integral along a path surrounding the crack tip. It can be observed that regarding less small crack angle θ_c, strain ERR results using beam theory are accurate compared to FE results. The similar conclusion is made by Bruno et al. [76]. They concluded that as a matter of fact for a short crack, curved laminated beam theory is not appropriate. The strain ERR value between their model and FE results are within 8 % error except for very short crack, where $\theta_c < 5°$. However, among their approaches, only a crack which is symmetric with respect to the middle span of the curved beam can be applied. Therefore, the objective of this study is to develop an analytical analysis for a composite curved beam with a delamination locates in any arbitrary interface and hoop location.

Chapter 2

RESEARCH OBJECTIVES

Composite structures provide higher specific strength and stiffness than structures composed of metallic materials. Among various applications, one of the most important components are composite beams. Over the last three decades, composite beams have been widely used in automobile and aerospace applications. In aerospace industry, aircraft wings contain box structures which are typically assembled of stringers and spars. A number of different cross-sections “I”, “C”, and “Z” are considered, where the concept of composite curved beam is applied. While FE based computational approaches have been developed and widely used to address various types of composite structures, there is a need to develop more efficient and compact analytical methods. Development of such approaches for curved beam structures is the overarching goal of the present research. Three different approaches are applied to analysis of composite beams including conventional beam, Wide Beam (WB) and Narrow Beam (NB) assumptions. General beam method is derived from CLT which takes in-plane properties into account. For WB, twisting curvature is allowed so that$M_{xy} = 0$. On the other hand, twisting curvature is suppressed for NB, and $M_{xy} \neq 0$ *is* induced.

The first objective of this research is to apply the NB assumptions to composite curved beam. The formulation of axial and bending stiffness of composite curved beam can yield very different results using different beam assumptions depends on the cross-section of the beam. If the width to height ratio is small ($\frac{w}{t} \ll 6$), NB assumption has to be applied.

The second objective is to predict stiffness reduction and stress variation in composites curved beam due to out-of-plane local fiber waviness. Composite materials have defects and imperfections such as fiber waviness, delamination, porosity, and resin migration, which are caused by the manufacturing process [77]. Fiber waviness often can be found in thick composites [78]. Several factors can cause this defect including non-uniform cure pressure, resin shrinkage or pre-buckling. Fiber waviness has an adverse influence on the mechanical properties. The tensile, compressive strength, and fatigue life degrade significantly [79]. Most of the research focused on fiber waviness is performed in unidirectional flat composites, but fiber waviness in composite curved beam using analytical approaches is not addressed. The proposed research aims to fill this void. A FE analysis will be conducted to verify results. If fiber waviness is located near leg region of curved beam, the maximum tensile stress σ_r no longer located in the middle span of the composite curved beam.

The third objective is to predict failure load of composite curved beam with delamination under bending. In the past studies, the delamination can be only located symmetrically with respect to the middle span of the composite curved beam. The results show that the strain ERR results have good agreement compared with FE analysis. However, for a short crack ($\theta_c < 5°$), analytical results no longer satisfy the numerical results. Therefore, this research aims to fill the void. In the present research, we allow for a delamination which is not symmetric with respect to the middle span of the composite curved beam and it can be located at any arbitrary interface.

Chapter 3

OVERVIEW OF CLASSICAL LAMINATION THEORY

3-1 Lamina Stage

A Lamina contains fiber and matrix which is characterized as a single layer. It is an orthotropic material with principal material axes in the fiber direction. In lamina level, it is usually to consider material homogeneous, and average properties is used in the analysis. This type of analysis is called micromechanics and considered the unidirectional lamina as a quasi-homogeneous anisotropic material with averaged stiffness and strength. A thin-walled unidirectional lamina is generally under plane stress assumption. Stresses along the thickness direction are assumed to be zeros, $\sigma_3 = \tau_{13} = \tau_{23} = 0$. The stress/strain relationship is further reduced to

$$\begin{bmatrix} \sigma_1 \\ \sigma_2 \\ \tau_{12} \end{bmatrix} = \begin{bmatrix} Q_{11} & Q_{12} & 0 \\ Q_{12} & Q_{22} & 0 \\ 0 & 0 & Q_{66} \end{bmatrix} \begin{bmatrix} \varepsilon_1 \\ \varepsilon_2 \\ r_{12} \end{bmatrix} \tag{3-1}$$

where

$$\begin{aligned} \mathrm{Q}_{11} &= \frac{E_1}{1 - v_{12}v_{21}} \quad , \quad Q_{22} = \frac{E_2}{1 - v_{12}v_{21}} \\ Q_{12} &= \frac{v_{12}E_2}{1 - v_{12}v_{21}} \quad , \quad Q_{66} = G_{12} \end{aligned} \tag{3-2}$$

E_1 is Young's modulus along 1-direction (fiber direction).

E_2 is Young's modulus along 2-direction.

G_{12} is shear modulus along 1-2 plan.

v_{12} is Poisson's ratio associated with loading in 1-direction and produced strain in 2-direction.

v_{21} is Poisson's ratio associated with loading in 2-direction and produced strain in 1-direction.

For a general anisotropic material, 21 material constants exhibit extension/shear coupling behavior. For a general orthotropic material, 9 material constants exhibit no extension/shear coupling behavior. If a thin orthotropic material is considered, only 4 material constants required to fully describe material behavior of a 2-D orthotropic material, E_1, E_2, G_{12}, and v_{12}. In viewing Eqs. (3-1), $[Q]$ matrix is so-called the reduced stiffness matrix, no shear strain is induced when σ_1 is applied. In addition, no in-plane strains are induced if τ_{12} is applied. This implies that for 0° lamina, where no extension/shear coupling are presented.

3-2 Stress Transformation

Normally, the lamina principal axes (1 and 2) do not coincide with the loading axes (x and y). The stress components referred to the principal axes can be transferred in terms of loading axes. The following Eqs. (3-3) shows stress transformation from 1-2 axes to x-y axes.

$$\begin{bmatrix} \sigma_x \\ \sigma_y \\ \tau_{xy} \end{bmatrix} = [T_\sigma(-\theta)] \begin{bmatrix} \sigma_1 \\ \sigma_2 \\ \tau_{12} \end{bmatrix} \tag{3-3}$$

where

$$[T_\sigma(\theta)] = \begin{bmatrix} m^2 & n^2 & 2mn \\ n^2 & m^2 & -2mn \\ -mn & mn & m^2 - n^2 \end{bmatrix}$$

and $m = \cos\theta$, $n = \sin\theta$, the angle θ is measured positive counterclockwise from the x-axis to the 1-axis as shown in Figure 3-1.

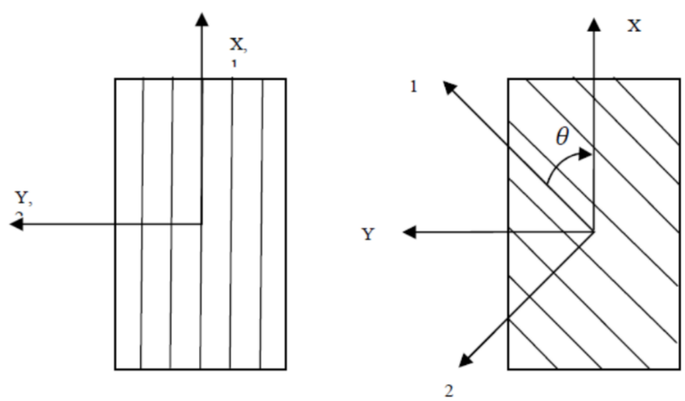

Figure 3-1 x-y coordinate system for a 0° lamina and 1-2 coordinate system for a θ° lamina.

The stress/strain relationship between transformed compliances as a function of the principal lamina compliances is given by

$$[\bar{S}]_{x-y} = [T_\varepsilon(-\theta)][S]_{1-2}[T_\sigma(\theta)] \qquad (3\text{-}4)$$

where

$$[T_\varepsilon(\theta)] = \begin{bmatrix} m^2 & n^2 & mn \\ n^2 & m^2 & -mn \\ -2mn & 2mn & m^2 - n^2 \end{bmatrix}$$

$$[S]_{1-2} = \begin{bmatrix} \frac{1}{E_1} & -\frac{v_{12}}{E_2} & 0 \\ -\frac{v_{12}}{E_2} & \frac{1}{E_2} & 0 \\ 0 & 0 & \frac{1}{G_{12}} \end{bmatrix}$$

The relationship of stiffness matrix in x-y coordinate system can be transformed to 1-2 coordinate system in terms of basic material constants E_1, E_2, v_{12}, and G_{12}.

$$[\bar{Q}]_{x-y} = [T_\sigma(-\theta)][Q]_{1-2}[T_\varepsilon(\theta)] \qquad (3\text{-}5)$$

3-3 Laminate Stage (Classical Lamination Theory)

The overall structural behavior of multidirectional laminate is a function of stacking sequence and material properties. The Classical Lamination Theory (CLT) for a multidirectional laminate predicts the behavior of the laminate based on several assumptions. First, the laminate is thin which means the lateral dimension is much larger than its thickness direction. Therefore, the plane stress assumption has to be followed, $\sigma_z = \tau_{xz} = \tau_{yz} = 0$. Second, displacements are small compared with the thickness of the laminate and displacements are continuous through the laminate. Third, cross-section remains normal to the middle surface after deformation, $\gamma_{xz} = \gamma_{yz} = 0$. Also, the normal distances from the middle surface remain constant, that is $\varepsilon_z = 0$. In general, each lamina and the entire laminate behave linearly elastic.

The displacements of the mid-plane are function of x and y:

$$u_0 = u_0(x, y) \qquad (3\text{-}6)$$

$$v_0 = v_0(x, y)$$

$$w_0 = w_0(x, y)$$

where u_0, v_0 and w_0 are displacements in the x, y, and z directions, respectively. The reference plane of a laminated plate locates at the mid plane of the plate. In general,

$$u = u_0 - z\frac{\partial w}{\partial x}$$

$$v = v_0 - z\frac{\partial w}{\partial y} \qquad (3\text{-}7)$$

where z is the through thickness coordinate.

A linear strain function across the thickness is assumed based on linear elastic behavior of the laminate. The strains at any given point can be expressed as functional of the reference plane strains and the laminate curvatures.

$$\begin{bmatrix} \varepsilon_x \\ \varepsilon_y \\ \gamma_{xy} \end{bmatrix} = \begin{bmatrix} \varepsilon_x^0 \\ \varepsilon_y^0 \\ \gamma_{xy}^0 \end{bmatrix} + z\begin{bmatrix} K_x \\ K_y \\ K_{xy} \end{bmatrix} \qquad (3\text{-}8)$$

$\varepsilon_x^0, \varepsilon_y^0, \gamma_{xy}^0, K_x, K_y$ and K_{xy} are mid-plane strains and curvatures can be expressed as

$$\varepsilon_x^0 = \frac{\partial u_0}{\partial x}$$

$$\varepsilon_y^0 = \frac{\partial v_0}{\partial y} \qquad (3\text{-}9)$$

$$\gamma_{xy}^0 = \frac{\partial u_0}{\partial y} + \frac{\partial v_0}{\partial x}$$

$$K_x = -\frac{\partial^2 w}{\partial x^2}$$

$$K_y = -\frac{\partial^2 w}{\partial y^2}$$

$$K_{xy} = -\frac{2\partial^2 w}{\partial x \partial y}$$

Once strain in k^{th} layer is obtained, the stresses in the k^{th} layer can be written as

$$\begin{bmatrix} \sigma_x \\ \sigma_y \\ \tau_{xy} \end{bmatrix}_{kth} = \left[\bar{Q}_{x-y}\right]_{kth} \left(\begin{bmatrix} \varepsilon_x^0 \\ \varepsilon_y^0 \\ \gamma_{xy}^0 \end{bmatrix} + z_{kth} \begin{bmatrix} K_x \\ K_y \\ K_{xy} \end{bmatrix} \right) \tag{3-10}$$

Based on Eqs. (3-10), even though the strain is linearly varied through the thickness direction of the laminate, the stress in each layer is discontinuous due to the varied transformed stiffness matrix $\left[\bar{Q}_{x-y}\right]_{kth}$. However, analyzing each layer individually is a cumbersome task. Because of the discontinuous variation of stresses, it is convenient to deal with the plate forces and plate moment instead of identifying individual layer. In laminate stage, the total force and moment resultants can be obtained by summing the effects for all layers as shown below.

$$\begin{bmatrix} N_x \\ N_y \\ N_{xy} \end{bmatrix} = \sum_{k=1}^{n} \int_{z_{k-1}}^{z_k} \begin{bmatrix} \sigma_x \\ \sigma_y \\ \tau_{xy} \end{bmatrix}_{kth} dz$$

$$\begin{bmatrix} M_x \\ M_y \\ M_{xy} \end{bmatrix} = \sum_{k=1}^{n} \int_{z_{k-1}}^{z_k} \begin{bmatrix} \sigma_x \\ \sigma_y \\ \tau_{xy} \end{bmatrix}_{kth} z\, dz \tag{3-11}$$

where z_k and z_{k-1} are the z-coordinates of the upper and lower surface in k^{th} layer. After integration, the plane force and moment resultants can be expressed as

$$\begin{bmatrix} N_x \\ N_y \\ N_{xy} \end{bmatrix} = [A] \begin{bmatrix} \varepsilon_x^0 \\ \varepsilon_y^0 \\ \gamma_{xy}^0 \end{bmatrix} + [B] \begin{bmatrix} K_x \\ K_y \\ K_{xy} \end{bmatrix}$$

$$\begin{bmatrix} M_x \\ M_y \\ M_{xy} \end{bmatrix} = [B] \begin{bmatrix} \varepsilon_x^0 \\ \varepsilon_y^0 \\ \gamma_{xy}^0 \end{bmatrix} + [D] \begin{bmatrix} K_x \\ K_y \\ K_{xy} \end{bmatrix} \tag{3-12}$$

where

$$[A] = \sum_{k=1}^{n} \left[\bar{Q}_{x-y}\right]_{kth} (z_k - z_{k-1}) \quad unit = lb/in$$

$$[B] = \frac{1}{2} \sum_{k=1}^{n} \left[\bar{Q}_{x-y}\right]_{kth} (z_k^2 - z_{k-1}^2) \quad unit = lb \tag{3-13}$$

$$[D] = \frac{1}{3} \sum_{k=1}^{n} \left[\bar{Q}_{x-y}\right]_{kth} (z_k^3 - z_{k-1}^3) \quad unit = lb - in$$

In viewing Eqs. (3-13), $[A]$, $[B]$ and $[D]$ matrix are functions of geometry, material properties and stacking sequence. They are the averaging elastic stiffness. $[A]$ is an extensional stiffness matrix relating in-plane loads to in-plane strains. $[B]$ is an extensional-bending coupling stiffness matrix relating in-plane load to curvatures and moments to in-plane strains. $[D]$ is a bending stiffness matrix. The relationship between force and moment resultants to the mid-plane strains and curvatures is shown below.

$$\begin{bmatrix} \bar{N} \\ \bar{M} \end{bmatrix}_{6x1} = \begin{bmatrix} A & B \\ B & D \end{bmatrix}_{6x6} \begin{bmatrix} \varepsilon^0 \\ K \end{bmatrix}_{6x1} \tag{3-14}$$

$$\begin{bmatrix} \varepsilon^0 \\ K \end{bmatrix}_{6x1} = \begin{bmatrix} a & b \\ b & d \end{bmatrix}_{6x6} \begin{bmatrix} \bar{N} \\ \bar{M} \end{bmatrix}_{6x1}$$

$$\begin{bmatrix} a & b \\ b & d \end{bmatrix}_{6x6} = \begin{bmatrix} A & B \\ B & D \end{bmatrix}^{-1}_{6x6}$$

where $[\bar{N}] = N, [\bar{M}] = M$ is shown in Eqs. (3-11). If mechanical loading and temperature loading are both considered, $[\bar{N}] = [N] + [N^T]$ and $[\bar{M}] = [M] + [M^T]$, where thermal induced loads $[N^T]$ and thermal induced moments $[M^T]$ is written as:

$$\begin{aligned} [N^T] &= \Delta T \sum_{k=1}^{n} [\bar{Q}_{x-y}]_{kth} [\alpha_{x-y}]_{kth} (z_k - z_{k-1}) \\ [M^T] &= \frac{\Delta T}{2} \sum_{k=1}^{n} [\bar{Q}_{x-y}]_{kth} [\alpha_{x-y}]_{kth} (z_k^2 - z_{k-1}^2) \end{aligned} \tag{3-15}$$

where α_{x-y} is the Coefficient of Thermal Expansion (CTE) and ΔT is the temperature difference.

Chapter 4

STIFFNESS AND STRESS INVESTIGATION OF COMPOSITE CURVED BEAM

4-1 Stiffness Model Formulation for Composite Curved Beam

The curved beam geometry shown in Figure 4-1 represents a rectangular cross-section with a mean radius R_m where $R_m = (R_o + R_i)/2$, and R_o is the outer radius and R_i is the inner radius of the curved beam. Beams usually are slender, and its dimension along the x-direction is greater than the other dimensions along y and z directions. The longitudinal axis is in the *x* or θ direction. The out-of-plane axis is in the *z* or *r* direction.

Assume line pp' is the mid-axis of the curved beam. In the k^{th} layer, the elongation after deformation is $(R_m + z)d\theta\ \varepsilon_\theta$. This elongation can be further describe in terms of mid-plane strain, ε^0, and curvature K, which is $(R_m + z)d\theta\ (\varepsilon^0 + z\,K)$. By equating above equations, the strain in any given point along θ direction can be expressed as

$$\varepsilon_\theta = \frac{R_m}{R_m + z}(\varepsilon^0 + z\,K) \tag{4-1}$$

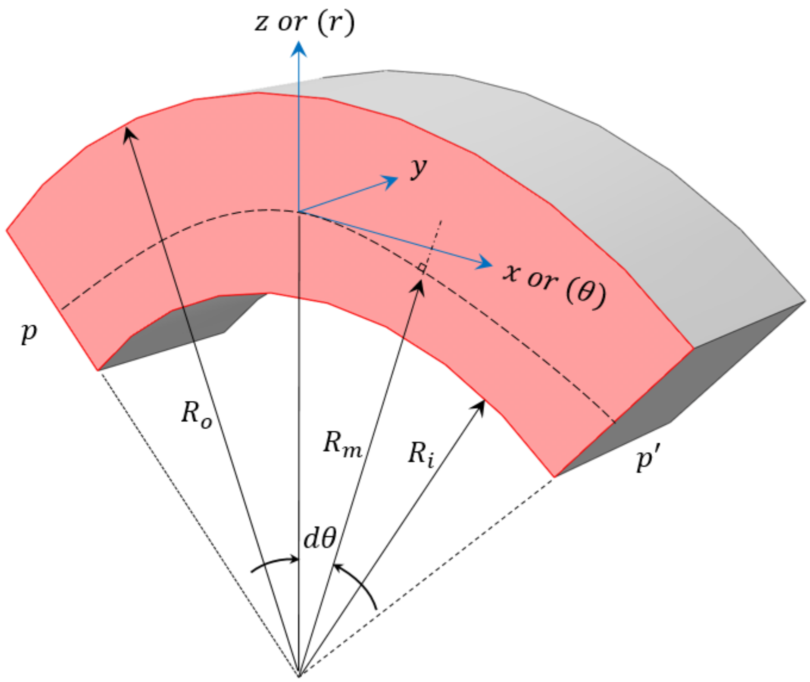

Figure 4-1 The configuration of the curved beam.

For a thick curved beam, shear deformation and rotary inertia are included in the derivation. The kinematical relationship for middle surface strain and curvature can be shown as

$$\varepsilon^0 = \frac{\partial u_0}{\partial x} + \frac{w_0}{R_m} \quad , \quad K = \frac{\partial \psi}{\partial x} \tag{4-2}$$

where

$$\gamma = \frac{\partial w}{\partial x} + \psi - \frac{u}{R_m} \tag{4-3}$$

and ψ is rotation between a line originally normal to the longitudinal direction to the out-of-plane direction, γ is the shear strain at the neutral axis. The force and moment resultants of the curved beam can be obtained by integrating stresses over the thickness of the beam.

$$[N] = \sum_{k=1}^{n} \int_{z_{k-1}}^{z_k} [\bar{Q}_{x-y}]_{kth} \frac{R_m}{R_m + z} (\varepsilon^0 + z\,K)\, dz = [\mathrm{A_c}]\varepsilon^0 + [B_c]K$$

$$[M] = \sum_{k=1}^{n} \int_{z_{k-1}}^{z_k} [\bar{Q}_{x-y}]_{kth} \frac{R_m}{R_m + z} (\varepsilon^0 + z\,K)\, z\, dz = [\mathrm{B_c}]\varepsilon^0 + [D_c]K \tag{4-4}$$

The averaging stiffness for a composite curved beam $[\mathrm{A_c}]$, $[\mathrm{B_c}]$, and $[\mathrm{D_c}]$ matrix can be expressed as

$$[A_c] = R_m \sum_{k=1}^{n} [\bar{Q}_{x-y}]_{kth} \ln \frac{R_m + z_k}{R_m + z_{k-1}}$$

$$[B_c] = R_m \sum_{k=1}^{n} [\bar{Q}_{x-y}]_{kth} \left[(z_k - z_{k-1}) - R_m \ln \frac{R_m + z_k}{R_m + z_{k-1}} \right] \tag{4-5}$$

$$[D_c] = R_m \sum_{k=1}^{n} [\bar{Q}_{x-y}]_{kth} \left[\frac{1}{2}(z_k^2 - z_{k-1}^2) - R_m(z_k - z_{k-1}) + {R_m}^2 \ln \frac{R_m + z_k}{R_m + z_{k-1}} \right]$$

The shear stiffness $[\overline{GA}_c]$ can be also describe as functional of R_m :

$$[\overline{GA}_c] = k_s R_m \sum_{k=1}^{n} (G_{13} \cos^2 \theta^k) \ln \frac{R_m + z_k}{R_m + z_{k-1}} \tag{4-6}$$

where $\mathrm{k_s}$ is the shear correction factor, typically taken as $5/6$ for rectangular cross-section. θ^k is the stacking sequence at the $\mathrm{k^{th}}$ layer. All the derivation can be found in detail from [13, 15, and 80].

4-2 Modified Stiffness Approach for Composite Beam

The cross-section of a beam can be categorized into three groups, general, wide, and narrow section. For a general beam which does not take the width to height ratio into account, since the twisting curvature K_{xy} is allowed, no twisting moment M_{xy} is induced. Therefore, the constitutive equation can be expressed as

$$\begin{bmatrix} \varepsilon_x^0 \\ K_x \end{bmatrix} = \begin{bmatrix} a_{11} & b_{11} \\ b_{11} & d_{11} \end{bmatrix} \begin{bmatrix} N_x \\ M_x \end{bmatrix} \tag{4-7}$$

where N_x is an applied force per unit width along x-direction and M_x is an applied moment per unit width. The axial stiffness is $\frac{1}{a_{11}}$, and the bending stiffness is $\frac{1}{d_{11}}$.

4.2.1. Wide Beam (WB)

If the width to height ratio is too small or too large, extra modifications should be considered. Considering a flat plate where the width to height ratio usually greater than 6, the lateral curvature, K_y is suppressed because of the flat cross-section under bending as shown in Figure 4-2. Since N_x and M_x are applied, $\varepsilon_x^0 \neq 0$ and $K_x \neq 0$. Moreover, due to flat plate geometry of the cross-section, mid-plane strains and curvatures in transverse direction are equal to zero. Hence, the resultants forces and moment in y and shear direction are induced.

$$\begin{gathered} \varepsilon_y^0 = \gamma_{xy}^0 = K_y = K_{xy} = 0 \\ N_y \neq 0, \;\; N_{xy} \neq 0, \;\; M_y \neq 0, \;\; M_{xy} \neq 0 \end{gathered} \tag{4-8}$$

The constitutive equation of a beam with wide cross-section can be expressed as

$$\begin{bmatrix} N_x \\ M_x \end{bmatrix} = \begin{bmatrix} A_{11} & B_{11} \\ B_{11} & D_{11} \end{bmatrix} \begin{bmatrix} \varepsilon_x^0 \\ K_x \end{bmatrix}$$

$$\begin{bmatrix} \varepsilon_x^0 \\ K_x \end{bmatrix} = \begin{bmatrix} A_{11} & B_{11} \\ B_{11} & D_{11} \end{bmatrix}^{-1} \begin{bmatrix} N_x \\ M_x \end{bmatrix} \tag{4-9}$$

$$A_x = A_{11} - \frac{B_{11}^2}{D_{11}}, \quad B_x = B_{11} - \frac{A_{11}D_{11}}{B_{11}}, \quad D_x = D_{11} - \frac{B_{11}^2}{A_{11}}$$

where A_x is axial stiffness, B_x is coupling stiffness, and D_x is bending stiffness.

In addition, the resultant force and moment in the transverse direction can be also obtained.

$$\begin{bmatrix} N_y \\ N_{xy} \\ M_y \\ M_{xy} \end{bmatrix} = \begin{bmatrix} A_{12} & B_{12} \\ A_{16} & B_{16} \\ B_{12} & D_{12} \\ B_{16} & D_{16} \end{bmatrix} \begin{bmatrix} A_{11} & B_{11} \\ B_{11} & D_{11} \end{bmatrix}^{-1} \begin{bmatrix} N_x \\ M_x \end{bmatrix} \tag{4-10}$$

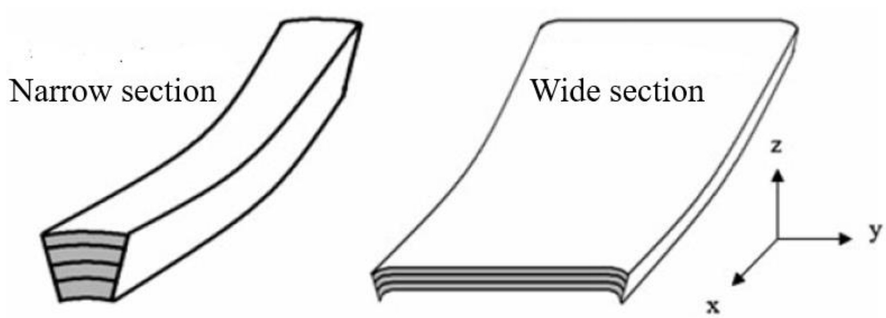

Figure 4-2 Deformed shape of laminated beam under pure bending with narrow and wide cross-sections.

4.2.2. Narrow Beam (NB)

If the width to height ratio of the cross-section is small as shown in Figure 4-2, the lateral curvature K_y is induced due to the effect of Poisson's ratio. For a beam under a bending moment M_x across the width of the beam, w, M_{xy} is induced. Since the loads per unit width is employed in the lamination theory, we have

$$\begin{gathered} \varepsilon_y^0 \neq 0, \qquad \gamma_{xy}^0 \neq 0, \qquad K_y \neq 0, \qquad K_{xy} = 0 \\ N_y = 0, \;\; N_{xy} = 0, \;\; M_y = 0, \;\; M_{xy} \neq 0 \end{gathered} \tag{4-11}$$

The overall 6 by 6 stiffness matrix in Eqs. (3-14) can be simplified to 3 by 3 matrix under the above assumptions.

$$\begin{bmatrix} \varepsilon_x^0 \\ K_x \\ K_{xy} \end{bmatrix} = \begin{bmatrix} a_{11} & b_{11} & b_{16} \\ b_{11} & d_{11} & d_{16} \\ b_{16} & d_{16} & d_{66} \end{bmatrix} \begin{bmatrix} N_x \\ M_x \\ M_{xy} \end{bmatrix} \tag{4-12}$$

M_{xy} can be expressed in terms of N_x and M_x due to suppressed curvature K_{xy}.

$$M_{xy} = -\frac{b_{16}}{d_{66}} N_x - \frac{d_{16}}{d_{66}} M_x \tag{4-13}$$

Substituting Eqs. (4-13) back to (4-12), the mid-plane strain and curvature along the x-direction are

$$\begin{gathered} \varepsilon_x^0 = \left(a_{11} - \frac{b_{16}^2}{d_{66}}\right) N_x + \left(b_{11} - \frac{b_{16} d_{16}}{d_{66}}\right) M_x \\ K_x = \left(b_{11} - \frac{b_{16} d_{16}}{d_{66}}\right) N_x + \left(d_{11} - \frac{d_{16}^2}{d_{66}}\right) M_x \end{gathered} \tag{4-14}$$

$$a^* = a_{11} - \frac{b_{16}^2}{d_{66}}, \qquad b^* = b_{11} - \frac{b_{16}d_{16}}{d_{66}}, \qquad d^* = d_{11} - \frac{d_{16}^2}{d_{66}}$$

In viewing Eqs. (4-14), the axial stiffness is obtained if only N_x is applied. Also, the bending stiffness is obtained if only M_x is applied. Thus, for bending case, $N_x = 0$, and for tension case, $M_x = 0$. The axial stiffness A_x and bending stiffness D_x for a composite beam with narrow cross-section are shown below.

$$A_x = \frac{d^*}{a^*d^* - {b^*}^2}, \quad B_x = -\frac{b^*}{a^*d^* - {b^*}^2}, \quad D_x = \frac{d^*}{a^*d^* - {b^*}^2} \tag{4-15}$$

4-3 Ply-Stress Investigation

In this section, two approaches are discussed for investigating stress distribution for the composite curved beam under bending. The first approach is developed by Lekhnitskii [5] and extended by William [8]. Figure 4-3 shows a curved beam subjected to shear force Q, axial force N, and bending moment M. The outer radius of the curved beam is denoted as *b,* and the inner radius of the curved beam is denoted as a. *r* is the distance from the center point O to any radial location of the curved beam. The width of the curved beam is denoted as *w*. If the composite material of the curved beam is assumed as continuous anisotropic material, the radial stress, tangential stress, and shear stress induced in the curved beam under end bending moment can be expressed as

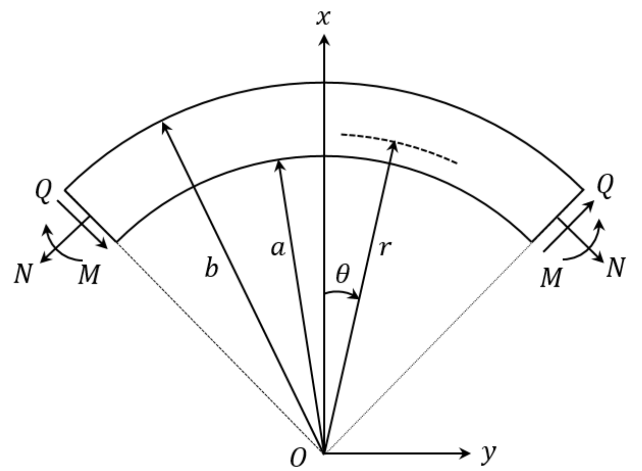

Figure 4-3 Geometry of curved beam under bending moment M, shear force Q, and axial force N.

$$
\begin{aligned}
\sigma_r(r) &= -\frac{M}{b^2wg}\left[1-\frac{1-\left(\frac{a}{b}\right)^{k+1}}{1-\left(\frac{a}{b}\right)^{2k}}\left(\frac{r}{b}\right)^{k-1}-\frac{1-\left(\frac{a}{b}\right)^{k-1}}{1-\left(\frac{a}{b}\right)^{2k}}\left(\frac{a}{b}\right)^{k+1}\left(\frac{b}{r}\right)^{k+1}\right] \\
\sigma_\theta(r) &= -\frac{M}{b^2wg}\left[1-\frac{1-\left(\frac{a}{b}\right)^{k+1}}{1-\left(\frac{a}{b}\right)^{2k}}k\left(\frac{r}{b}\right)^{k-1}-\frac{1-\left(\frac{a}{b}\right)^{k-1}}{1-\left(\frac{a}{b}\right)^{2k}}k\left(\frac{a}{b}\right)^{k+1}\left(\frac{b}{r}\right)^{k+1}\right]
\end{aligned}
\tag{4-16}
$$

where $k=\sqrt{\frac{E_\theta}{E_r}}$, E_θ is modulus along θ-direction, and E_r is modulus along r-direction. The parameter g can be expressed as

$$
g=\frac{1-\left(\frac{a}{b}\right)^2}{2}-\frac{k}{k+1}\frac{\left[1-\left(\frac{a}{b}\right)^{k+1}\right]^2}{1-\left(\frac{a}{b}\right)^{2k}}+\frac{k\left(\frac{a}{b}\right)^2}{k-1}\frac{\left[1-\left(\frac{a}{b}\right)^{k-1}\right]^2}{1-\left(\frac{a}{b}\right)^{2k}}
\tag{4-17}
$$

It is noticing that no shear stress $\tau_{r\theta}$ is induced for a composite curved beam under bending. In addition, both σ_r and σ_θ are independent of θ based on Eqs. (4-16).

The stress induced in the composite curved beam due to the end shear force Q can be written as

$$\sigma_r(r,\theta) = \frac{Q}{bwg_1}\frac{b}{r}\left[\left(\frac{r}{b}\right)^\beta + \left(\frac{a}{b}\right)^\beta\left(\frac{b}{r}\right)^\beta - 1 - \left(\frac{a}{b}\right)^\beta\right]\sin\theta$$

$$\sigma_\theta(r,\theta) = \frac{Q}{bwg_1}\frac{b}{r}\left[(1+\beta)\left(\frac{r}{b}\right)^\beta + (1-\beta)\left(\frac{b}{r}\right)^\beta\left(\frac{a}{b}\right)^\beta - 1 - \left(\frac{a}{b}\right)^\beta\right]\sin\theta \qquad (4\text{-}17)$$

$$\tau_{r\theta}(r,\theta) = \frac{Q}{bwg_1}\frac{b}{r}\left[\left(\frac{r}{b}\right)^\beta + \left(\frac{a}{b}\right)^\beta\left(\frac{b}{r}\right)^\beta - 1 - \left(\frac{a}{b}\right)^\beta\right]\cos\theta$$

where

$$\beta = \sqrt{1 + \frac{E_\theta}{E_r}\left(1 - 2v_{r_\theta}\right) + \frac{E_\theta}{G_{r\theta}}}$$

$$g_1 = \frac{2}{\beta}\left[1 - \left(\frac{a}{b}\right)^\beta\right] + \left[1 + \left(\frac{a}{b}\right)^\beta\right]\ln\frac{a}{b} \qquad (4\text{-}18)$$

and $G_{r\theta}$ is shear modulus and $v_{r\theta}$ is Poisson’s ratio.

It is noticing that radial stress, tangential stress, and shear stress are functional of r and θ. For isotropic material, the anisotropic parameter $\beta = 2$.

The second approach is provided by Gonz´alez-Cantero et al. [81, 82]. The CLT approach can provide stresses in θ and y directions under bending moment and axial forces for a composite curved beam. However, it is not capable to compute interlaminar radial stress σ_r using CLT. Therefore, they provided an analytical model to aim this void. A cylindrical coordinate system with radius *r* and the angle θ is shown in Figure 4-4, where R is the medium radius, r_{ii} and r_{oi} are the inner and outer radius of the i^{th} ply. Substituting Eqs. (4-5) into (3-14), the mid-plane strains and curvatures can be computed. For the bending case, $\bar{N} = 0$.

$$\begin{bmatrix} \varepsilon^0 \\ K \end{bmatrix}_{6x1} = \begin{bmatrix} a_c & b_c \\ b_c & d_c \end{bmatrix}_{6x6} \begin{bmatrix} \bar{N} \\ \bar{M} \end{bmatrix}_{6x1} \tag{4-19}$$

where

$$\begin{bmatrix} a_c & b_c \\ b_c & d_c \end{bmatrix} = \begin{bmatrix} A_c & B_c \\ B_c & D_c \end{bmatrix}^{-1}$$

The strains in any radial location can be obtained using Eqs. (3-8), and the tangential stress σ_θ in the k^{th} ply can be further calculated using stress/strain relationship in Eqs. (3-1).

$$\begin{bmatrix} \sigma_\theta \\ \sigma_y \\ \tau_{y\theta} \end{bmatrix}_{kth} = \begin{bmatrix} \bar{Q}_{11} & \bar{Q}_{12} & \bar{Q}_{16} \\ \bar{Q}_{12} & \bar{Q}_{22} & \bar{Q}_{16} \\ \bar{Q}_{16} & \bar{Q}_{26} & \bar{Q}_{66} \end{bmatrix}_{kth} \left(\begin{bmatrix} \varepsilon_\theta^0 \\ \varepsilon_y^0 \\ \gamma_{y\theta}^0 \end{bmatrix} + z \begin{bmatrix} K_\theta \\ K_y \\ K_{\theta y} \end{bmatrix} \right) \tag{4-20}$$

It is noticing that only in-plane (θ, y) stresses are obtained using CLT due to plane stress assumption as shown in Eqs. (4-20) where $\bar{Q}_{16}$ and $\bar{Q}_{26}$ are coupling terms due to Poisson's ratio. Once the tangential stress σ_θ is obtained, the out-of-plane stresses σ_r and $\tau_{r\theta}$ can be computed due to equilibrium.

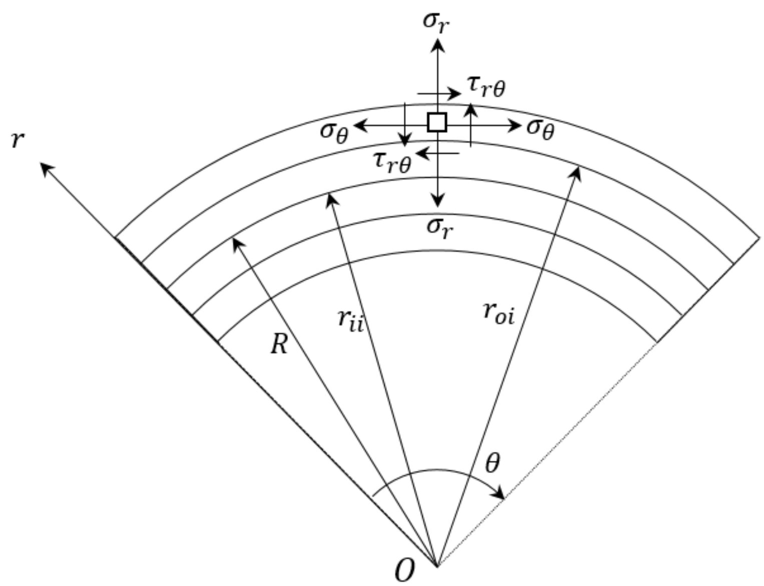

Figure 4-4 Definition of ply radius [65].

The elasticity equilibrium equations in polar coordinates system are shown as:

$$\frac{\partial \sigma_\theta}{\partial \theta} + \frac{1}{r}\frac{\partial (r^2 \tau_{r\theta})}{\partial r} = 0$$
$$\frac{\partial (r\sigma_r)}{\partial r} + \frac{\partial \tau_{r\theta}}{\partial \theta} = \sigma_\theta \quad (4\text{-}21)$$

Based on closed-form solutions provided by Lekhnitskii [5], composite curved beam exhibits no shear stress under pure bending moment. Thus, shear terms in Eqs. (4-21) is neglected. The radial stress σ_r can be expressed as

$$\sigma_{r,M}^{i} = \sigma_{r,M}^{i-1}(r_{oi},\theta)\frac{r_{oi}}{r} - \frac{N_l R (EA)_i M(\theta)}{wtrEI}\left[r_{oi} - r - \left(R + \frac{EI}{EV}\right) log\frac{r_{oi}}{r}\right] \quad (4\text{-}22)$$

where the stiffness EI, EV, and EA are bending stiffness, coupling stiffness, and axial stiffness given by:

$$EI = \frac{\Delta w}{A_c}, \quad EV = \frac{\Delta w}{B_c}, \quad EA = \frac{\Delta w}{D_c}, \qquad \Delta = A_c D_c - B_c^2 \tag{4-23}$$

The stiffness $(EA)_i$ is axial stiffness for a single ply, $(EA)_i = EA/N_p$, N_p is total number of plies for the composite curved beam. It should be noted that the radial stress $\sigma_{r,M}^i$ depends on the previous ply $i-1$. Therefore, initialize σ_r^0 with boundary condition is necessary and given by $\sigma_{r_M}^0(r_{i1}, \theta) = 0$.

A comparison between the stresses stated in Eqs. (4-20) and (4-22) and stresses using Lekhnitskii's [5] equation is presented in Figure 4-5. According to Figure 4-5(a), tangential stress distribution σ_θ is perfectly match with numerical results. However, significant errors between Eqs. (4-16) and (4-22) are obtained as shown in Figure 4-5(b). In addition, Eqs. (4-22) is very sensitive with the given total ply number. If the ply number is greater than 15 plies, inaccurate results will be obtained.

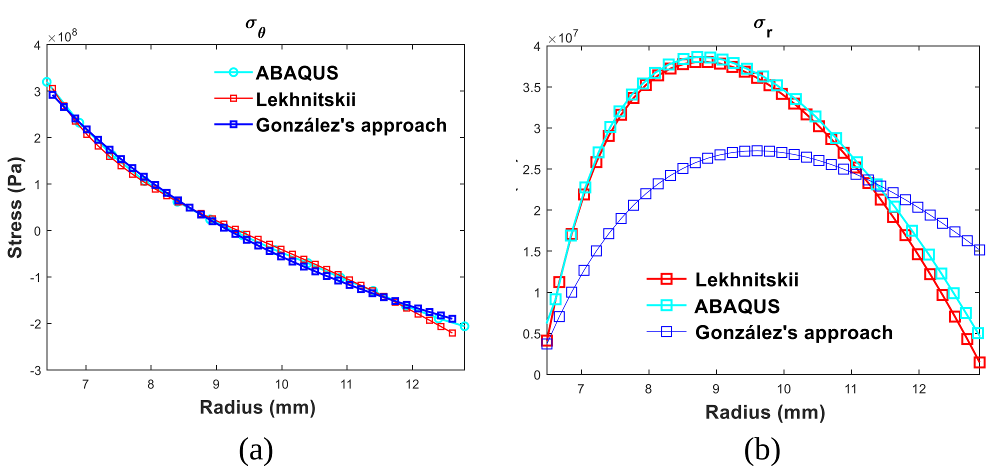

Figure 4-5 Stress distribution for a composite curved beam under bending (a) tangential stress σ_θ (b) radial stress σ_r

Therefore, modification is needed for Eqs. (4-22) to satisfy results obtained from ABAQUS [83] and Lekhnitskii's approach. After modification, it shows prefect agreement between analytical and numerical results as shown in Figure 4-6.

$$\sigma_{r.M}^{i}(r,\theta) = \sigma_{\mathrm{r,M}}^{\mathrm{i-1}}\left(\frac{r_i}{r_o}\right) + \frac{R_m Q(1,1) M(\theta)}{rEI}\left[r_o - r_i - \left(R_m + \frac{EI}{EV}\right)\log\frac{r_o}{r_i}\right] \qquad (4\text{-}24)$$

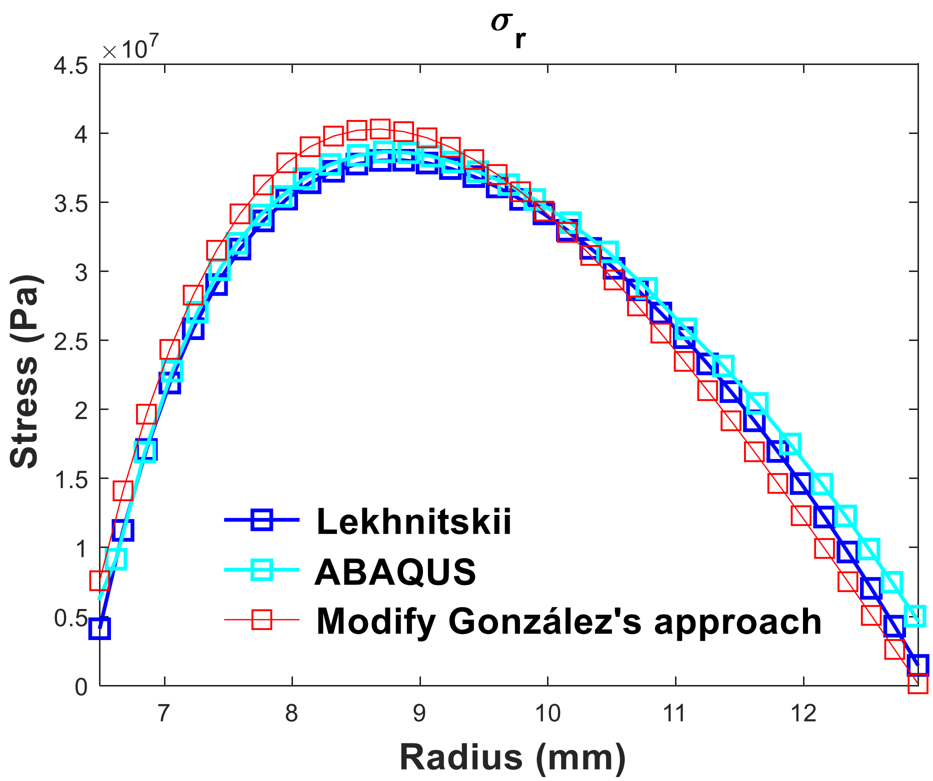

Figure 4-6 σ_r distribution for a composite curved beam under bending (Eqs. 4-24).

4-4 Effective Stiffness Results and Discussion

In this study, three different beam assumptions due to width to height ratio are discussed including general, wide, and narrow cross-section beams. A parameter study is presented in this section to describe behaviors of the beam using general, wide, and narrow assumptions, respectively. The inner radius of the composite curved beam is 6.4 mm and the outer radius is 12.988 mm. The width of the beam is 12.7 mm. Therefore, the mean radius R_m is 9.694 mm and the total thickness of the beam is 6.588 mm, which means it contains 36 plies and the ply thickness is 0.183 mm for IM7/8552 material. The material properties for IM7/8552 [84] are:

$$\mathrm{E}_1 = 157\ \mathrm{GPa} \qquad \mathrm{E}_2 = 8.96\ \mathrm{GPA} \qquad \mathrm{E}_3 = 8.96\ \mathrm{GPa}$$

$$\mathrm{G}_{12} = 5.08\ \mathrm{GPa} \qquad \mathrm{G}_{23} = 2.99\ \mathrm{GPa} \qquad \mathrm{G}_{13} = 5.08\ \mathrm{GPa}$$

$$\mathrm{v}_{12} = 0.32 \qquad \mathrm{v}_{23} = 0.5 \qquad \mathrm{v}_{13} = 0.32$$

where E_1, E_2, and E_3 are the Young's moduli of the composite lamina along the material coordinates. G_{12}, G_{23}, G_{13} and are the Shear moduli and ν_{12} , ν_{23}, and ν_{13} are Poisson's ratio with respect to the 1-2, 2-3 and 1-3 planes, respectively.

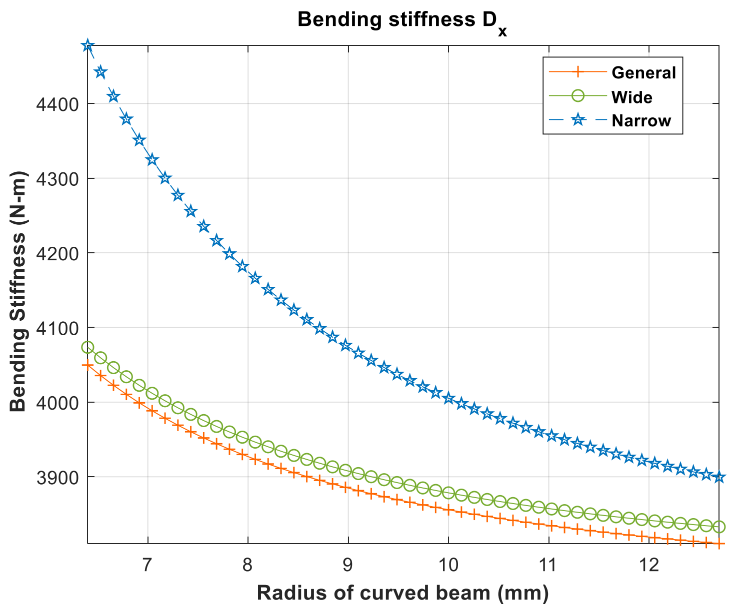

Figure 4-7 Difference between general (Eqs. 4-7), wide (Eqs. 4-9) and narrow (Eqs. 4-15) section for a beam with initial curvature.

Based on Figure 4-7, it could be seen that NB assumption provides higher bending stiffness in x-direction and general beam and WB provides lower stiffness. It also shows that bending stiffness decreases when the radius of curved beam increases.

Table 4-1 Bending stiffness comparison between beam with general, wide and narrow cross-section. The bending stiffness for a bema with and without curvature is also presented.

D_x	*General*			*Wide*			*Narrow*		
radius	curved	straight	% Diff.	curved	straight	% Diff.	curved	straight	% Diff.
6.4	4.0497	3.7409	8.25%	4.0735	3.7629	8.25%	4.4777	3.7409	19.70%
6.7	4.0154	3.7409	7.34%	4.039	3.7629	7.34%	4.3916	3.7409	17.39%
7.1	3.9868	3.7409	6.57%	4.0102	3.7629	6.57%	4.3206	3.7409	15.50%
7.4	3.9625	3.7409	5.92%	3.9858	3.7629	5.92%	4.2611	3.7409	13.91%
7.7	3.9419	3.7409	5.37%	3.965	3.7629	5.37%	4.2107	3.7409	12.56%
8.1	3.924	3.7409	4.89%	3.9471	3.7629	4.90%	4.1675	3.7409	11.40%

Table 4-2 (continued)

D_x	*General*			*Wide*			*Narrow*		
8.4	3.9085	3.7409	4.48%	3.9315	3.7629	4.48%	4.1303	3.7409	10.41%
8.7	3.895	3.7409	4.12%	3.9179	3.7629	4.12%	4.0979	3.7409	9.54%
9.1	3.883	3.7409	3.80%	3.9059	3.7629	3.80%	4.0695	3.7409	8.78%
9.4	3.8725	3.7409	3.52%	3.8952	3.7629	3.52%	4.0444	3.7409	8.11%
9.7	3.8631	3.7409	3.27%	3.8858	3.7629	3.27%	4.0222	3.7409	7.52%
10	3.8546	3.7409	3.04%	3.8773	3.7629	3.04%	4.0024	3.7409	6.99%
10.4	3.8471	3.7409	2.84%	3.8697	3.7629	2.84%	3.9847	3.7409	6.52%
10.7	3.8403	3.7409	2.66%	3.8628	3.7629	2.65%	3.9687	3.7409	6.09%
11	3.8341	3.7409	2.49%	3.8566	3.7629	2.49%	3.9543	3.7409	5.70%
11.4	3.8285	3.7409	2.34%	3.851	3.7629	2.34%	3.9413	3.7409	5.36%
11.7	3.8234	3.7409	2.21%	3.8459	3.7629	2.21%	3.9294	3.7409	5.04%
12	3.8187	3.7409	2.08%	3.8412	3.7629	2.08%	3.9186	3.7409	4.75%
12.4	3.8144	3.7409	1.96%	3.8369	3.7629	1.97%	3.9087	3.7409	4.49%
12.9	3.8105	3.7409	1.86%	3.8329	3.7629	1.86%	3.8996	3.7409	4.24%

Table 4-1 shows effective curved bending stiffness comparison between beam with general, wide and narrow cross-section to the straight beam. Unit of bending stiffness is N-m, and unit of the radius is mm. When the mean radius is getting smaller, the bending stiffness under NB assumptions has almost 20 % difference compared with the bending stiffness of a straight beam. It should be noticed that the bending stiffness for a straight beam under narrow assumption and general assumption are identical because the coupling stiffness $d_{16} = b_{11} = b_{16} = 0$ for a given unidirectional beam.

Table 4-3 and Figure 4-8 show the maximum tangential stress comparison using stiffness under three different beam assumptions for a curved beam under bending. The stress results are compared with σ_θ obtained from Lekhnitskii [5]. It can be concluded that narrow beam assumption has higher accuracy than stress results obtained using wide and general beam assumptions. Thus, narrow beam assumption is selected and will be implemented through rest of research since the cross-section of present beam, the width to height ratio is close to 2. It should be noticed that wide beam assumption is used for a regular composite thin plate. However, if the cross-section likes “I”, “Z”, or “C” is implemented defined as thin-wall structures, narrow beam assumption should be considered.

Table 4-3 Maximum tangential stress comparison between narrow, wide, and general section beam with closed-form solution provided by Lekhnitskii [5].

	Lekhnitskii	Narrow	Wide	General
σ_θ^{max} (MPa)	281.17	286.72	297.36	299.11
% Diff with Lekhnitskii	0 %	1.97 %	5.76 %	6.38 %

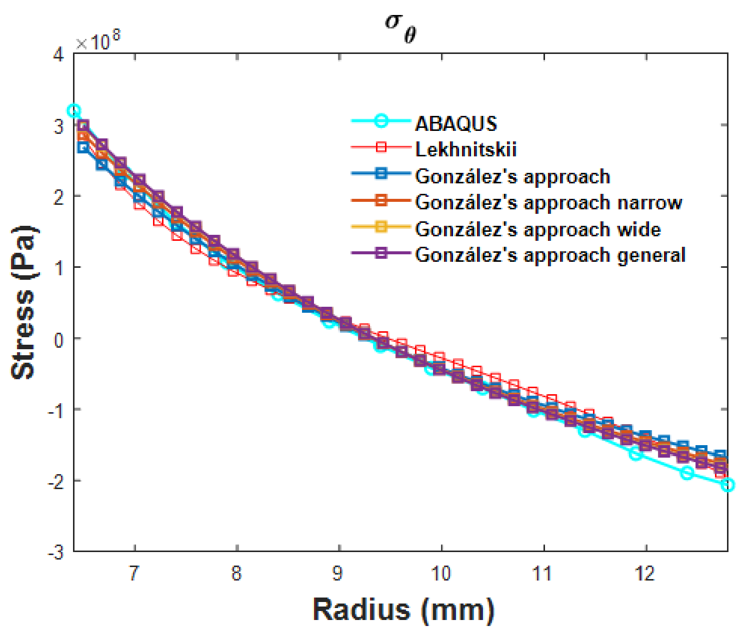

Figure 4-8 σ_θ comparison using stiffness under general, wide, and narrow beam assumptions.

Chapter 5

COMPOSITE CURVED BEAM WITH FIBER WAVINESS

Fiber waviness is a misalignment of the fibers in a ply. Fiber waviness usually occurs due to residual stress which occurred from tooling or pressure from the other layer. In addition, it can be caused by wrinkles or non-uniform consolidation pressure. Fiber waviness results in stiffness and strength loss and acts as a failure initiation in composite structures. This chapter describes the development of analytical methodology for predicting in-plane and out-of-plane fiber waviness in lamina or in laminate stage. The approach is based on definition of fiber waviness shape. The averaging moduli is evaluated by considering the shape of fiber waviness.

5-1 Effective Stiffness Properties for Straight In-Plane Lamina with Fiber Waviness

Fiber waviness can be expressed by a sinusoidal wave function in the 1-2 coordinate system as shown in Figure 5-1, where $R = A/L$ is a severity factor of the curvature of fiber waviness, A is the amplitude of fiber waviness, and L is the length of fiber waviness. As a result, the waviness angle ϕ can be introduced as

$$\phi = tan^{-1}\left[\pi R\, cos\frac{\pi x}{L}\right] \tag{5-1}$$

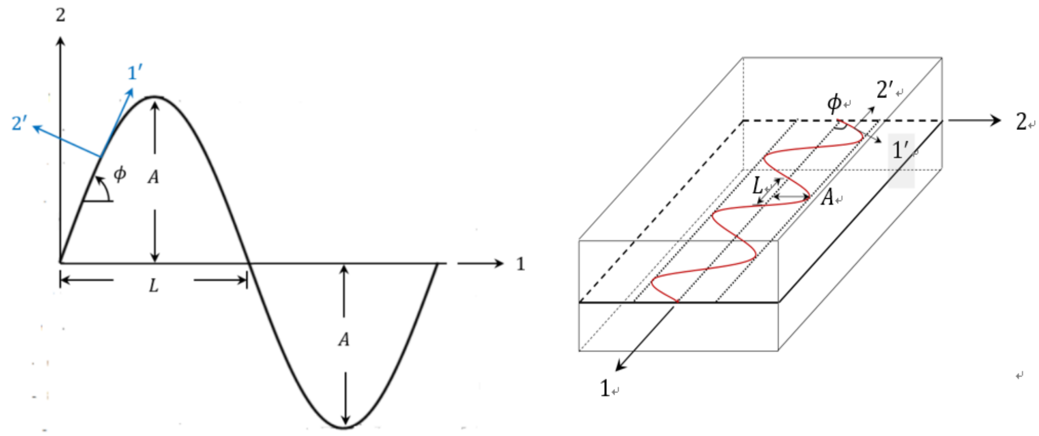

(a) (b)

Figure 5-1 (a) 2-D in-plane fiber waviness geometry. (b) 3-D in-plane fiber waviness geometry.

Fiber orientation is changed along fiber waviness direction. Therefore, the average compliance properties of 0° lamina $[S']$ can be computed by integrating fiber orientation where the direction is rotated based on sinusoidal function over the length L. Starts with compliance matrix for a 0° lamina without fiber waviness [S], the transformation and averaging results for $[S']$ are listed in Appendix A.

Since the average compliance matrix for 0° is obtained, by rotating with respect to the z-axis, in-plane compliance matrix $[\bar{S}']$ can be obtained. The equivalent properties with fiber waviness are:

$$\overline{E_1} = \frac{1}{\bar{S}'_{11}}$$
$$\overline{E_2} = \frac{1}{\bar{S}'_{22}} \tag{5-2}$$

$$\overline{G_{12}} = \frac{1}{\bar{S}'_{66}}$$

$$\overline{v_{12}} = -\frac{\bar{S}_{12}{}'}{\bar{S}'_{11}}$$

5-2 Effective Stiffness Properties for Straight Out-of-Plane Lamina with Fiber Waviness

The average compliance of a constant ply with fiber waviness S'_{ij} can be also rotated with respect to x or 1-direction by introducing an out of plane angle β as shown in Figure 5-2.

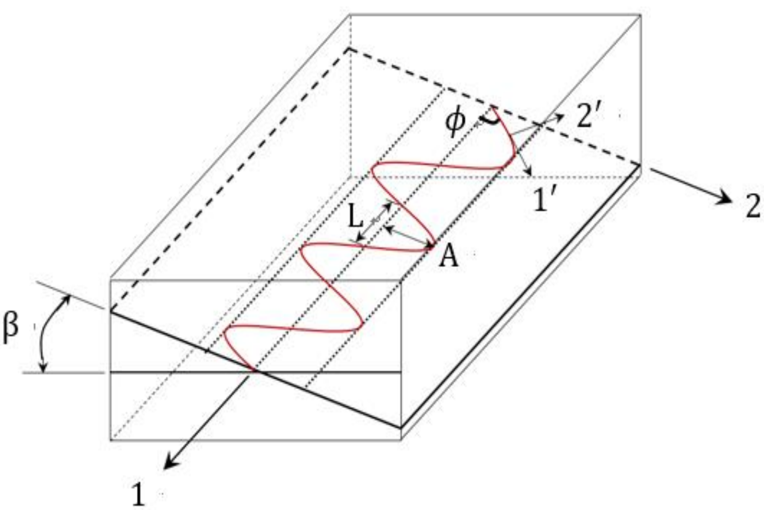

Figure 5-2 D out-of-plane fiber waviness geometry.

After rotating with respect to the x-axis, the out-of-plane compliance matrix $[S'']$ with average fiber waviness properties can be obtained using stress transformation as shown below.

$$[S''] = [T\varepsilon(-\beta)]_x [S'] [T_\sigma(\beta)]_x \tag{5-3}$$

where

$$[T_\sigma(\beta)]_x = \begin{bmatrix} 1 & 0 & 0 & 0 & 0 & 0 \\ 0 & m^2 & n^2 & 2mn & 0 & 0 \\ 0 & n^2 & m^2 & -2mn & 0 & 0 \\ 0 & -mn & mn & m^2 - n^2 & 0 & 0 \\ 0 & 0 & 0 & 0 & m & -n \\ 0 & 0 & 0 & 0 & n & m \end{bmatrix}$$

$$[T\varepsilon(\beta)]_x = \begin{bmatrix} 1 & 0 & 0 & 0 & 0 & 0 \\ 0 & m^2 & n^2 & mn & 0 & 0 \\ 0 & n^2 & m^2 & -mn & 0 & 0 \\ 0 & -2mn & 2mn & m^2 - n^2 & 0 & 0 \\ 0 & 0 & 0 & 0 & m & -n \\ 0 & 0 & 0 & 0 & n & m \end{bmatrix} \tag{5-4}$$

and $m = \cos\beta$ and $n = \sin\beta$. The average stiffness properties can be expressed as

$$\overline{E_1} = \frac{1}{S''_{11}}$$

$$\overline{E_3} = \frac{1}{S''_{33}}$$

$$\overline{G_{13}} = \frac{1}{S''_{55}} \tag{5-5}$$

$$\overline{\nu_{13}} = -\frac{S''_{13}}{S''_{11}}$$

5-3 Effective Stiffness Properties of Composite Straight Laminate with In-Plane and Out-of-Plane Fiber Waviness

In the previous section, the properties of a single layer with in-plane fiber waviness is considered. To evaluate the laminate performance, CLT approach can be used to obtain the average stiffness constant by considering of the summation with the average compliance with fiber waviness $[S']$ for a 0° unidirectional laminate or $[\bar{S}']$ for multi-directional laminate for each layer.

$$[A] = \sum_{k=1}^{n} \left[\overline{Q'}_{x-y}\right]_{kth} (z_k - z_{k-1})$$

$$[B] = \frac{1}{2}\sum_{k=1}^{n} \left[\bar{Q}'_{x-y}\right]_{kth} (z_k^2 - z_{k-1}^2) \tag{5-6}$$

$$[D] = \frac{1}{3}\sum_{k=1}^{n} \left[\bar{Q}'_{x-y}\right]_{kth} (z_k^3 - z_{k-1}^3)$$

where

$$\left[\bar{Q}'_{x-y}\right]_{kth} = [\bar{S}']^{-1} \tag{5-7}$$

Regarding with out-of-plane fiber waviness, the out-of-plane compliance matrix can be computed by rotating in-plane properties 90° with respect to x-axis. Thus, the stiffness tensor $[Q]$ for each ply can be obtained by inversing compliance matrix. Uniform out-of-plane fiber waviness is assumed. The amplitude of fiber waviness, A, remains constant along thickness direction. The average compliance for a lamina with in-plane fiber orientation is shown in Figure 5-3 and can be expressed as

$$[\bar{S}_{out}] = [\mathrm{T}\varepsilon(-\theta)]_{\mathrm{z}}[\mathrm{T}\varepsilon(-\beta)]_{\mathrm{x}}[S'][\mathrm{T}_{\sigma}(\beta)]_{\mathrm{x}}[\mathrm{T}\sigma(\theta)]_{\mathrm{z}}$$
$$[\bar{Q}'_{out}] = [\bar{S}_{out}]^{-1} \tag{5-8}$$

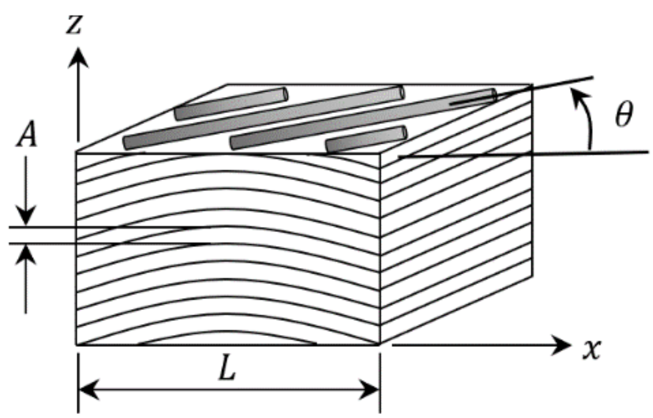

Figure 5-3 Out-of-plane fiber waviness in laminate stage with in-plane fiber orientation.

The equivalent [A], [B], and [D] matrix for a straight laminate with in-plane fiber orientation can be written as

$$[\mathrm{A}] = \sum_{k=1}^{n} [\bar{Q}'_{out}]^{kth}(z_k - z_{k-1})$$
$$[\mathrm{B}] = \frac{1}{2}\sum_{k=1}^{n} [\bar{Q}'_{out}]^{kth}(z_k^2 - z_{k-1}^2) \tag{5-9}$$

$$\mathrm{D} = \frac{1}{3}\sum_{k=1}^{n}\left[\bar{Q}'_{out}\right]^{kth}(z_k^3 - z_{k-1}^3)$$

It should be noticed that [A], [B], and [D] matrix have dimensions 6 by 6 instead of 3 by 3 because 3-D laminate behavior is considered.

5-4 Incremental Loading Scheme

The average stiffness properties alternate with the amplitude and length of fiber waviness. During the preceding of increasing the strain, the fiber waviness amplitude and fiber waviness length are changed, resulted in the effective moduli reduces. For a given loading, stress can be transformed from x-y plane to 1-2 coordinate system and 1′-2′ (along fiber direction) coordinate system. Therefore, the updated fiber waviness length and fiber length can be obtained. Based on sinusoidal assumption, the updated amplitude can be computed. Since average stiffness is functional of the amplitude and fiber waviness length, once the amplitude and fiber waviness length are updated based on incremental strain, the effective stiffness can be recalculated every iterations. The detail derivation is shown in Appendix B and stated in Figure 5-4. It should be noted that the effective stiffness result is very sensitive to the incremental strain. The total strain can be accumulated based on the given little incremental strain. That incremental strain, if tension is considered, it will lead to reduction of fiber waviness amplitude and increment of fiber waviness length. If the given incremental strain is too limit, insignificant changes for fiber waviness amplitude and length are observed. Consequently, there is no significant stiffness reduction if the applied incremental strain is too small. The practical incremental strain will be discussed later by comparing with numerical results.

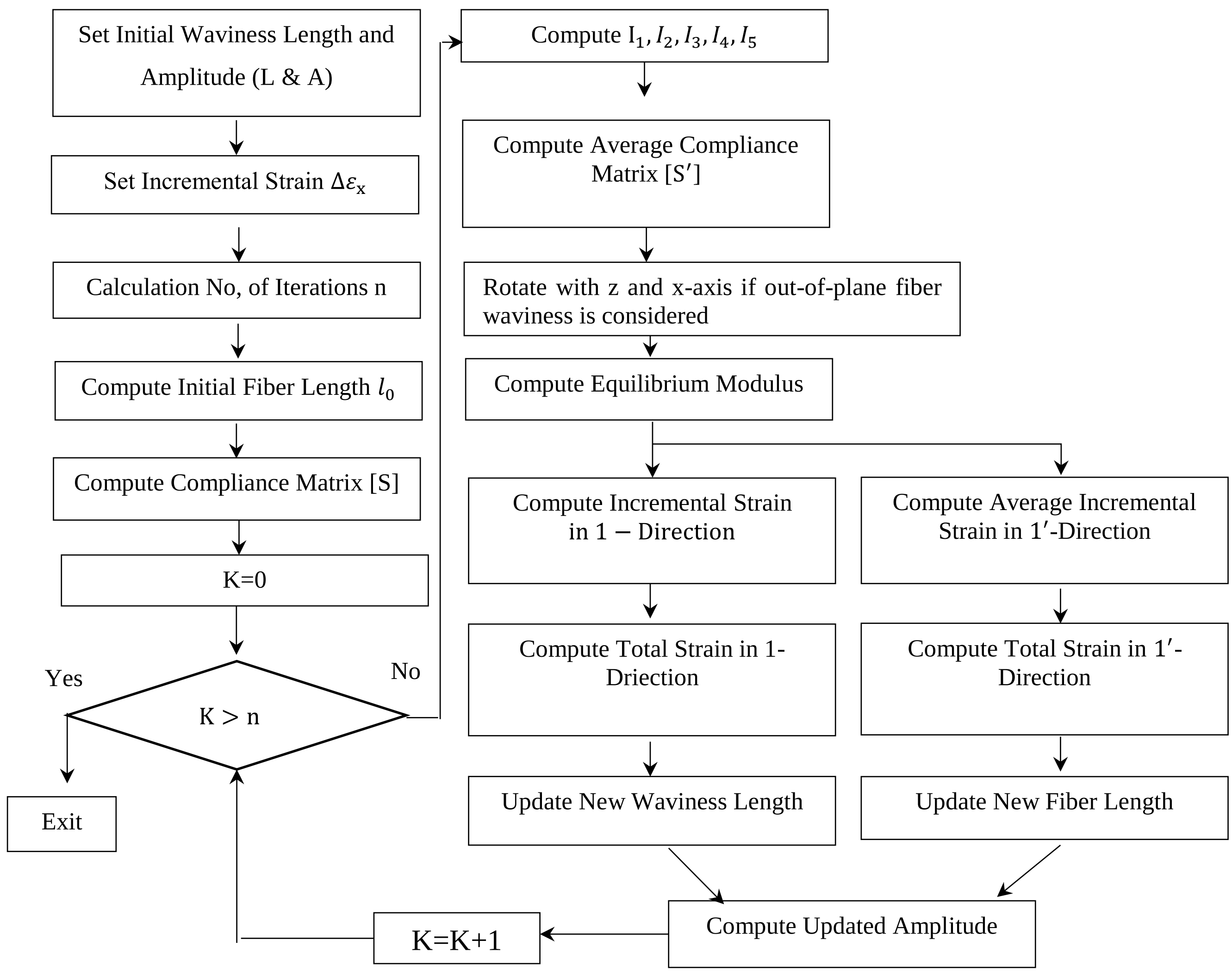

Figure 5-4 Flow chart for finding updated fiber waviness amplitude after every incremental strain.

5-5 Effective Stiffness Properties for Composite Curved Beam with In-Plane and Out-of-Plane Fiber Waviness

Curved Lamina with in-plane fiber waviness is shown in Figure 5-5(a). The average stiffness properties of curved lamina can be achieved by replacing $\left[\bar{Q}_{x-y}\right]_{kth}$to $\left[\bar{Q}'_{x-y}\right]_{kth}$ as shown in Eqs. (5-10). It should be noticed that the uniform fiber waviness is assumed in this section. However, a graded fiber waviness is often to be found and will be introduced for out-of-plane curved beam model.

$$\bar{A}'_{\mathrm{c}} = \mathrm{R_m} \sum_{k=1}^{n} \left[\overline{Q'}_{x-y}\right]_{kth} \ln \frac{R_m + z_k}{R_m + z_{k-1}}$$

$$\bar{B}'_{\mathrm{c}} = R_m \sum_{k=1}^{n} \left[\overline{Q'}_{x-y}\right]_{kth} \left[(z_k - z_{k-1}) - R_m \ln \frac{R_m + z_k}{R_m + z_{k-1}}\right] \tag{5-10}$$

$$\overline{D'}_{\mathrm{c}} = R_m \sum_{k=1}^{n} \left[\overline{Q'}_{x-y}\right]_{kth} \Big[\frac{1}{2}\left(z_k^2 - z_{k-1}^2\right) - R_m(z_k - z_{k-1}) + R_m^2 \ln \frac{R_m + z_k}{R_m + z_{k-}}$$

Out-of-plane fiber waviness is characterized by raising and falling in the manner of wavy layers. It will degrade the strength and fatigue performance of composite structure. In general, non-uniform fiber waviness is observed along the curved region instead of uniform fiber waviness distribution. Out-of-plane approach for straight laminate can be applied to here by adjusting amplitude and length for fiber waviness of each ply. The configuration of out-of-plane graded fiber waviness along the curved region is shown in Figure 5-5(b), where LA_{end}^{top} and LA_{end}^{bot} are the location of plies where the zero amplitudes are observed on the configuration. LA_{max} is the ply location where the maximum amplitude of fiber waviness is observed. Fiber waviness length, L, changes in thickness direction where $\mathrm{L}^{\mathrm{kth}}$ and $\mathrm{r}^{\mathrm{kth}}$ is the length of fiber waviness and the corresponding radius for a lamina in k^{th} layer.

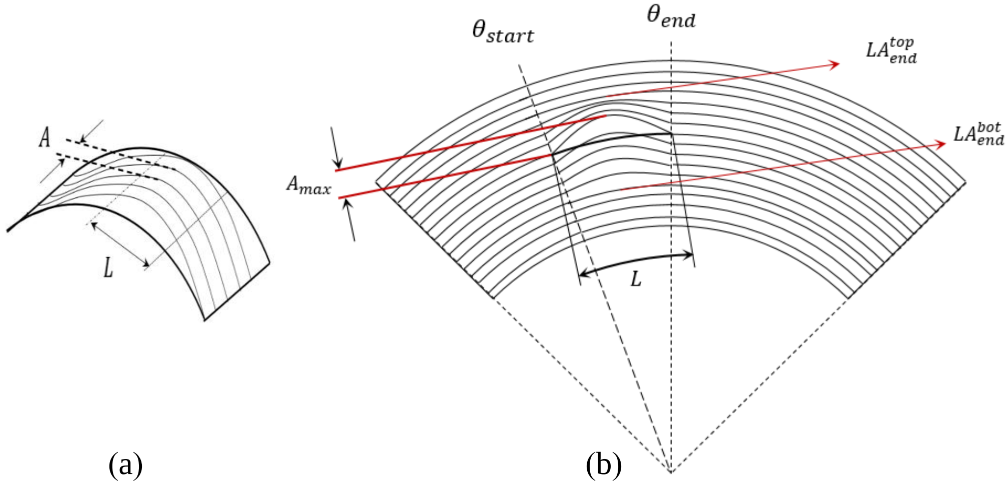

Figure 5-5 (a) In-plane fiber waviness in a curved lamina. (b) Out-of-plane fiber waviness in a curved beam.

$$\mathrm{L}^{\mathrm{kth}} = 2\pi r^{kth}\left(\frac{\theta_{end} - \theta_{start}}{360}\right) \tag{5-11}$$

The amplitude of fiber waviness, A_{max}, is the maximum amplitude can be observed. Thus, the amplitude varied respect to different layers can be obtained. The amplitudes below and above the location where contains the maximum amplitude A_{max} are

$$\mathrm{A_{low}} = \frac{A_{max}\left(ply^{th} - LA_{end}^{bot}\right)}{LA_{max} - LA_{end}^{bot}} \qquad \text{for ply}^{\text{th}} = \ LA_{end}^{bot}\ to\ LA_{max}$$

$$\mathrm{A_{upp}} = A_{max} - \frac{A_{max}(ply^{th} - LA_{max} + 1)}{LA_{end}^{top} - LA_{max}} \quad \text{for ply}^{\text{th}} \tag{5-12}$$

$$= \ LA_{max}\ to\ LA_{end}^{top} - 1$$

where $ply_{low}^{th} = LA_{end}^{bot} \sim LA_{max}$, and $ply_{upp}^{th} = LA_{max} \sim LA_{end}^{top} - 1$. Thus, the amplitude can be displaced as $Amplitude = [A_{low},\ A_{upp}]$ from bottom ply to the top ply of entire curved beam.

Substituting Eqs. (5-12) into (5-8), the effective stiffness properties for a composite curved beam with out-of-plane fiber waviness can be written as:

$$\overline{A'}_{\mathrm{c}} = \ \mathrm{R_m} \sum_{k=1}^{n} \left[\overline{Q'}_{out}\right]^{kth} \ln\frac{R_m + z_k}{R_m + z_{k-1}}$$

$$\overline{B'}_{\mathrm{c}} = \ R_m \sum_{k=1}^{n} \left[\overline{Q'}_{out}\right]^{kth} \left[(z_k - z_{k-1}) - R_m \ln\frac{R + z_k}{R + z_{k-1}}\right] \tag{5-13}$$

$$\overline{D'}_{\mathrm{c}} = \ R_m \sum_{k=1}^{n} \left[\overline{Q'}_{out}\right]^{kth} \left[\frac{1}{2}\left(z_k^2 - z_{k-1}^2\right) - R_m(z_k - z_{k-1}) + R_m^2 \ln\frac{R_m + z_k}{R_m + z_{k-1}}\right.$$

5-6 Maximum Radial Stress Prediction

In Eqs. (4-24), $Q(1,1)$ can be replaced to $[Q(1,1)_{out}]_{kth}$ in order to obtain equivalent stiffness in composite curved beam with fiber waviness. It should be noted that constant ply thickness is assumed in Eqs. (4-24). However, if fiber waviness is presented, ply thickness is going to be functional of the amplitude of fiber waviness in each ply. Therefore, Eqs (4-24) can be modified as

$$\sigma^{i}_{r.M}(r,\theta) = \sigma^{\mathrm{i-1}}_{\mathrm{r,M}}\left(\frac{r_{ii}}{r_{oo}}\right) + \frac{R_m[Q(1,1)_{out}]_{kth}M(\theta)}{rEI}\left[r_{oo} - r_{ii} - \left(R_m + \frac{EI}{EV}\right)\log\frac{r_{oo}}{r_{ii}}\right] \qquad (5\text{-}14)$$

where $r_{ii} = r_i + Amplitude_i$ and $r_{oo} = r_o + Amplitude_i$. $Amplitude_i$ is the amplitude of fiber waviness in i$^{\text{th}}$ ply.

5-7 Finite Element Analysis

5.7.1. In-Plane Straight Lamina with Fiber Waviness

In this section, a FE analysis of an in-plane lamina with a given ratio R is developed to study effects of fiber waviness with respect to Young's modulus along the x-direction. Isotropic material properties for fiber and matrix are implemented to modeling of composite behavior instead of using averaging stiffness properties. Multiple layers will be considered to avoid the edge effect. In this study, IM7/8552 carbon epoxy composite is used, where

$\mathrm{E}_1 = 157$ GPa $\quad$ $\mathrm{E}_2 = 8.96$ GPA $\quad$ $\mathrm{E}_3 = 8.96$ GPa

$\mathrm{G}_{12} = 5.08$ GPa $\quad$ $\mathrm{G}_{23} = 2.99$ GPa $\quad$ $\mathrm{G}_{13} = 5.08$ GPa

$\mathrm{v}_{12} = 0.32$ $\quad$ $\mathrm{v}_{23} = 0.5$ $\quad$ $\mathrm{v}_{13} = 0.32$

For IM7 fiber, $E_{1f} = 290\ GPa$ and$v_f = 0.2$, where E_{1f} is Young's modulus of fiber and v_f is Poisson's ratio of fiber. For 8552 epoxy, $E_m = 4.67\ GPa$ and $v_m = 0.37$, where E_m is Young's modulus of matrix and v_m is Poisson's ratio of matrix. The IM7 fiber diameter is $4\ \mu m$. Assuming the fiber volume fraction is 59.7 %, according to Figure 5-6, the matrix diameter d_m can be achieved by:

$$d_m = \frac{d_f n - V_f d_f n - V_f A}{2 V_f n} \tag{5-15}$$

where n is total ply number. For $n = 10$, $d_m = 1.3462\ mm$.

Uniform displacement 0.0008 mm is applied on the right surface. Lateral constrain is applied on the left surface. Vertical constrains are applied on the four corners so Poisson's ratio is allowed for upper and lower surfaces. It should be noted that L is half sinusoidal length. Plane stress CPS4 element is implemented.

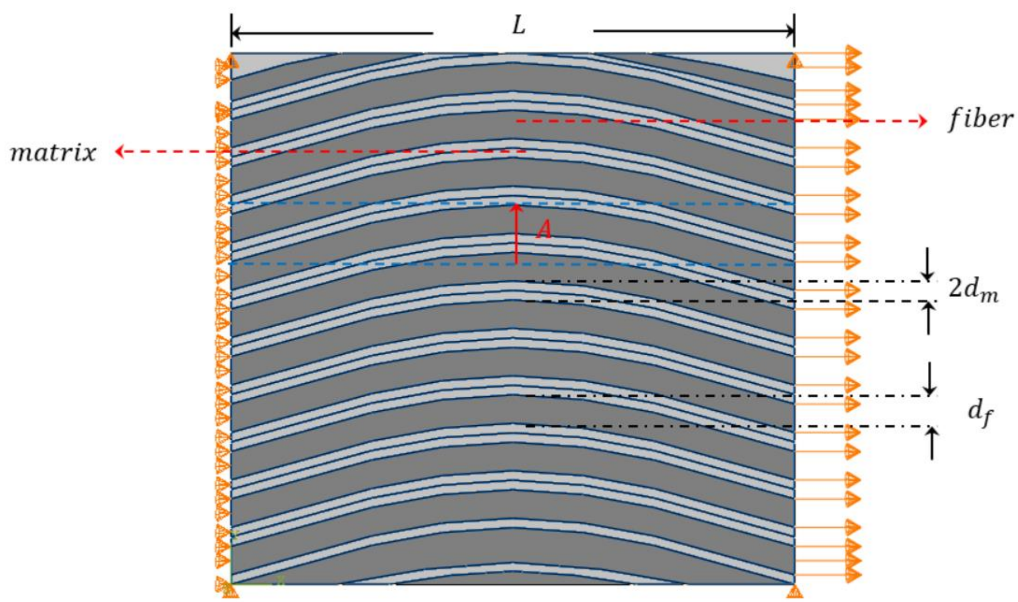

Figure 5-6 Geometry of in-plane fiber waviness.

The equivalent Young's modulus is calculated by average stress divided by average strain. The average stress is obtained from the total reaction force applied at the right surface.

$$\bar{E}_x = \frac{\frac{\overline{F_x}}{wh}}{\frac{L+u}{L} - 1} \tag{5-16}$$

where $\overline{F_x}$ is the total force along x-the direction, u is the applied displacement at the right surface and L is lengthe th of fiber waviness, w is the width of the plate and h is the height of the plate, where $h = n(2d_m + d_f) + A$. According to Figure 5-7, u_2 is symmetric with respect to vertical middle line of the lamina. Large contraction is observed for area under blue color as shown in Figure 5-7(b) due to Poisson's ratio effect. Poisson's ratio effect gradually increases when the fiber orientation approaches to zero. Based on the observation of Figure 5-8, the magnitude of shearing stress are identical on both size regarding vertical middle line but has opposite sign directions. Once the ratio $R = A/L$ is getting larger, shear failure will dominate instead of fiber or matrix failure.

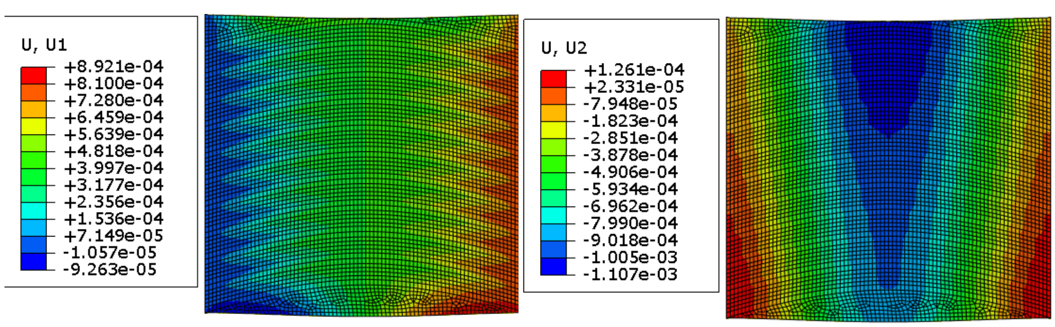

(a) (b)

Figure 5-7(a) Displacement along 1-direction. (b) Displacement along 2-direction.

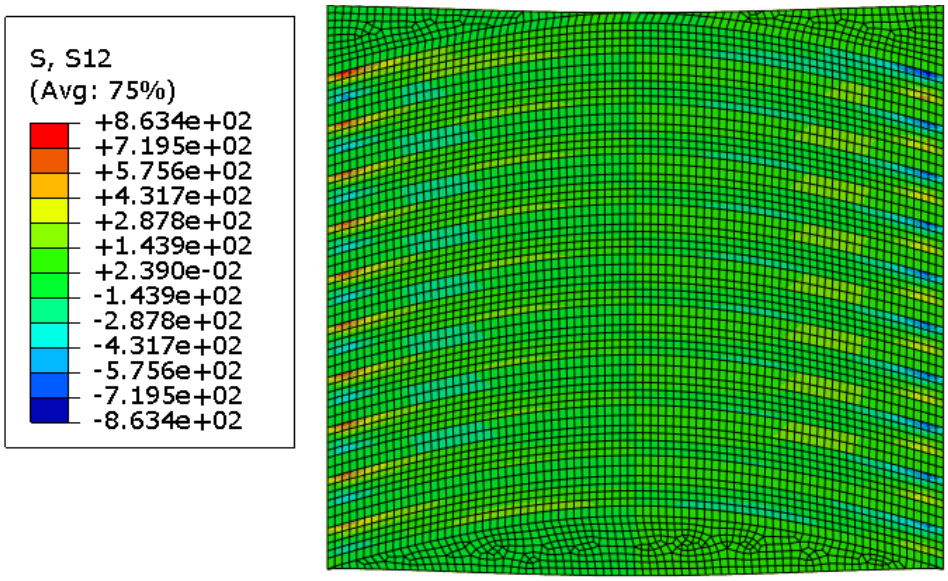

Figure 5-8 Shear distribution for an in-plane lamina with fiber waviness under tension.

5.7.2. Out-of-Plane Curved Laminate with Fiber Waviness

In this section, a 36 plies unidirectional curved laminate is assumed. The outer radius of the curved beam is 12.7 mm and the inner radius is 6.4 mm. 2-D plane strain linear element without fully integrated was employed. Convergence study was performed before finalizing the mesh density. A global mesh density in the order of 626 elements is established based on a mesh-convergence study to execute a linearly-static finite element analysis. A bending moment of 20 K-N is applied at the one end of the curved beam. On the other end, cantilever boundary condition is considered as shown in Figure 5-9(b). In order to ensure uniform longitudinal cross-section deformation along x-axis under the influence of a finite bending moment, a multi-points constraint is generated. A node with coupling constrains connected with the end surface was implemented to present a constant moment at the end surface of the curved beam. Additionally, all layers are perfectly bonded with upper and lower adjacent surfaces as shown in Figure 5-9(a). The model is first validated by assuming zero amplitude for all layers with isotropic material properties. The numerical stress results are compared with analytical approach provided by [5].

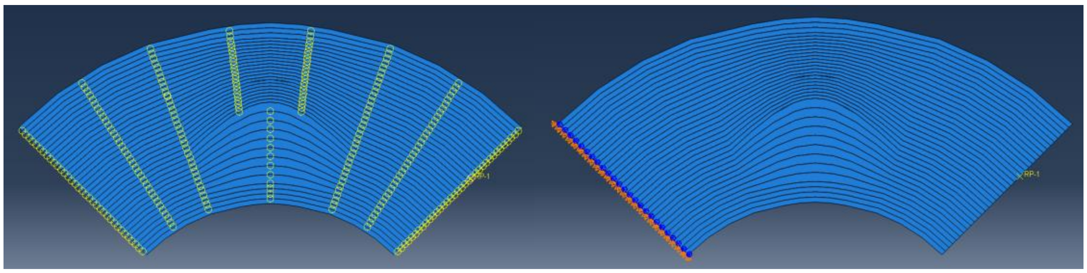

(a) (b)

Figure 5-9 (a) Perfect bonded layers (b) Boundary conditions and applied moment.

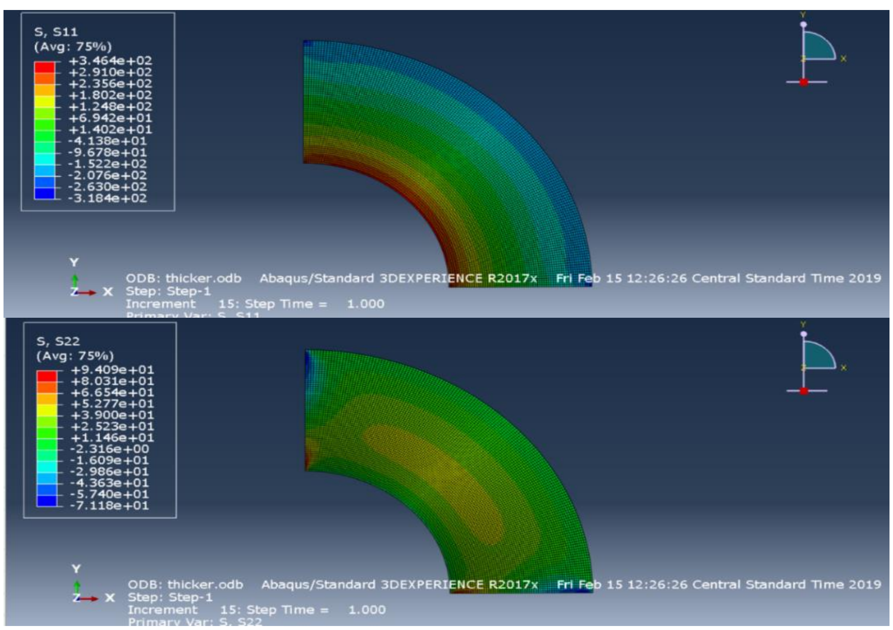

Figure 5-10 Finite Element analysis σ_1 and σ_2 results using isotropic material properties ($E = 30\ MPa$ and $v = 0.3$).

Table 5-1 Stresses comparison between analytical solution [5] and numerical solutions using isotropic material properties.

Isotropic validation	σ_θ (Pa)		σ_r (Pa)	
	min	max	min	max
Lekhnitskii [5]	$-1.9546e^8$	$3.0674e^8$	0	$4.15e^7$
ABAQUS	$-1.9305e^8$	$2.99e^8$	0	$3.98e^7$
% Diff.	1.23 %	2.52 %	0 %	4.27%

Table 5-2 Stresses comparison between analytical solution [5] and numerical solutions using composite material properties.

Composite validation	σ_θ (Pa)		σ_r (Pa)	
	min	max	min	max
Lekhnitskii [5]	$-2.20e^8$	$3.048e^8$	0	$4.028e^7$
ABAQUS	$-2.06e^8$	$3.20e^8$	0	$4e^7$
% Diff.	0.64 %	4.98 %	0 %	0.69 %

According to Table 5-1, results obtained from ABAQUS have great agreement with analytical results [5]. This model is further developed by using composite material properties. It should be mentioned that the anisotropic parameter k is introduced in the approach. For isotropic material, $k = 1$ and for current material, k is approximately equal to 4. The maximum radial stress using isotropic material properties is higher than anisotropic stress results about 5 %. According to Table 5-2, stresses results using composite material properties have great agreement between ABAQUS and analytical results.

5-8 Results and Discussion

5.8.1. In-Plane Fiber Waviness for 0° Lamina

In this section, stiffness reduction due to in-plane fiber waviness is studied. The average material properties varied with R are presented in Figure 5-11 and comparison between numerical and analytical Young's modulus along the x-direction results is shown in Table 5-3. Dramatic stiffness reduction is observed when fiber waviness ratio R changes from 0 and 0.3, about 85 % reduction in stiffness along the x-direction is observed. Since in-plane fiber waviness is assumed, no altered stiffness along the z-direction is observed. A specific point, $R = 0.72$ should be mentioned. At this kind of fiber waviness shape, the Young's modulus along the x-direction and y-direction are identical. When R reaches to infinity, the Young's modulus along the y-direction increases significantly due to most of fibers align in y-direction instead of x-direction.

Table 5-3 Numerical and analytical Comparison between Young's modulus reduction along the x-direction and fiber waviness parameter R.

R	$\bar{E}_x$ Analytical	$\bar{E}_x$ FEM	% Diff
0	$15.7\ \mathrm{E}^{10}$	$15.699\ \mathrm{E}^{10}$	0.0 %
0.1	$6.958\ \mathrm{E}^{10}$	$7.072\ \mathrm{E}^{10}$	1.61 %
0.2	$3.186\ \mathrm{E}^{10}$	$3.271\ \mathrm{E}^{10}$	2.59 %
0.3	$2.093\ \mathrm{E}^{10}$	$2.011\ \mathrm{E}^{10}$	4.07 %

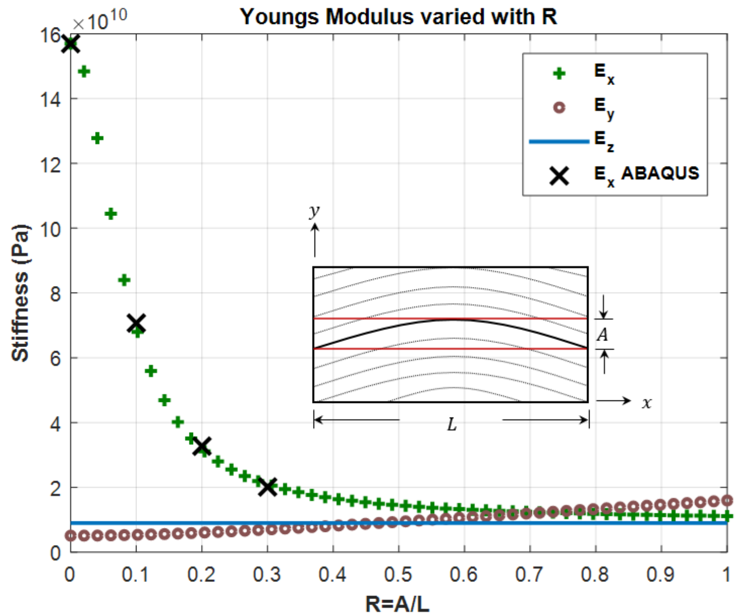

Figure 5-11 Comparison between Young's moduli and waviness parameter R.

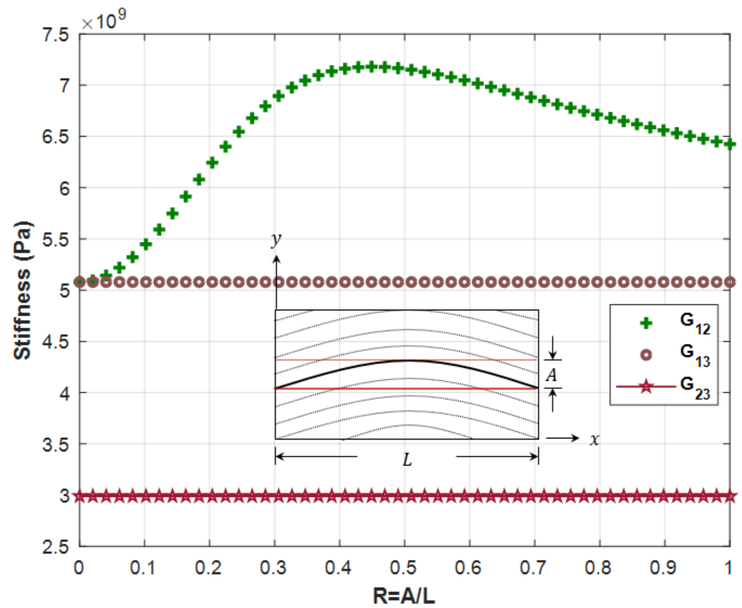

Figure 5-12 Shear moduli vs fiber waviness parameter R.

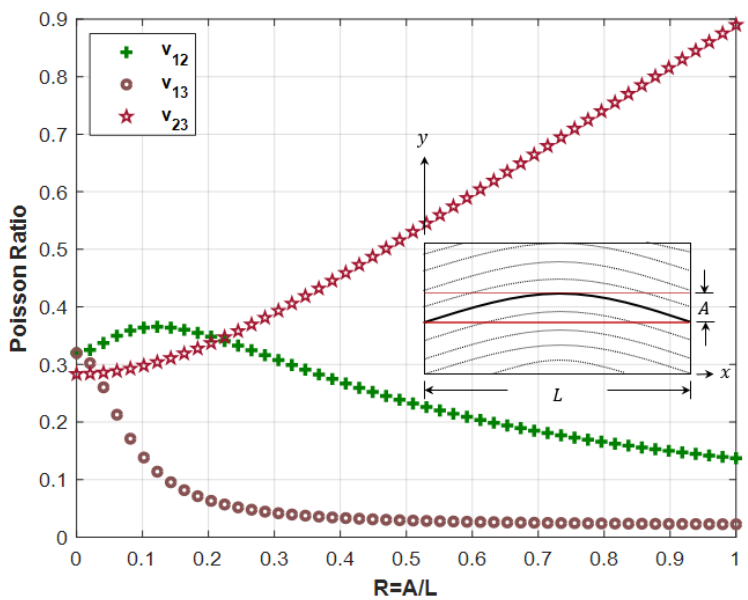

Figure 5-13 Poisson's ratios vs fiber waviness parameter R.

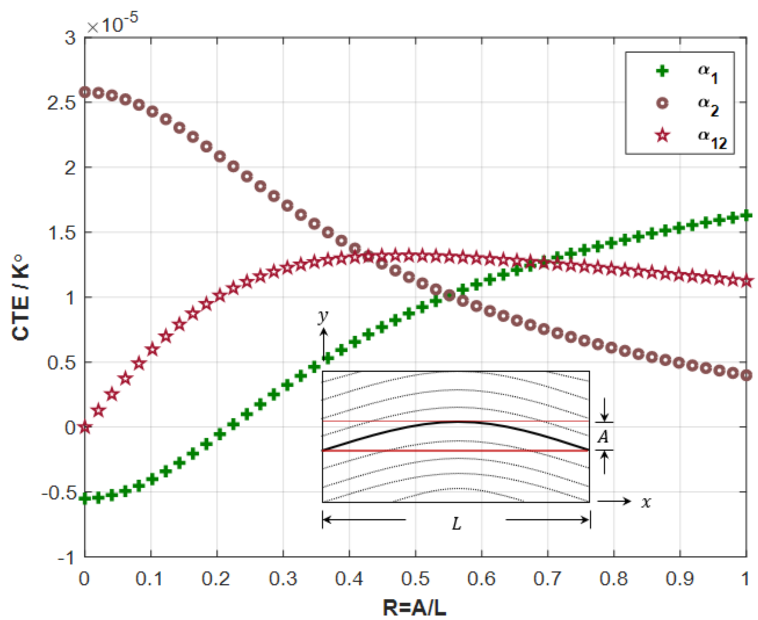

Figure 5-14 CTEs vs fiber waviness parameter R.

Shear modulus varies with respect to fiber waviness ratio R is shown in Figure 5-12. The maximum in-plane shear modulus G_{12} occurs at $R = 0.45$. It should be noted that G_{12} gradually decreases to its original value, which is given in material properties as R goes to infinity. There is no out-of-plane shear modulus changed since in-plane lamina with fiber waviness is considered. In-plane Poisson's ratio reaches to maximum value when $R = 0.1$ as shown in Figure 5-13. If loading is in the y-direction, v_{23} increase significantly since stiffness in the y-direction increases. The comparison between CTE and fiber waviness ratio R is presented in Figure 5-14 where α_1 increases and α_2 decreases dramatically when R increases.

5.8.2. In-Plane Fiber Waviness for $\theta°$ Lamina

In this section, Young's moduli, shear moduli, Poisson's ratios, and CTEs varied with respect to fiber waviness parameter R for a given lamina with designed fiber orientation angle θ will be discussed.

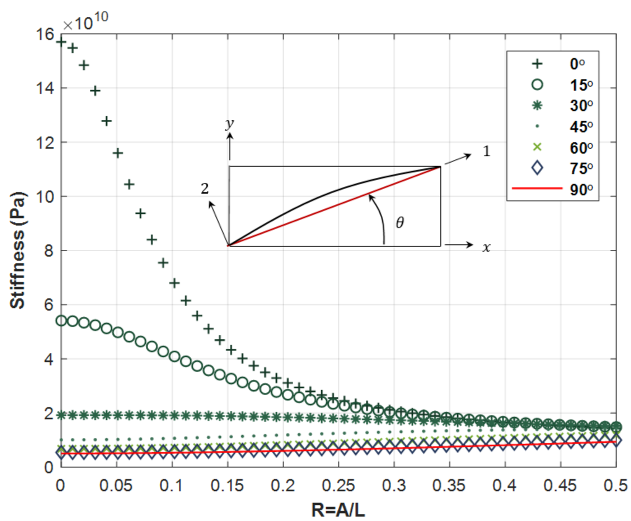

Figure 5-15 $\bar{E}_x$ vs waviness ratio, R with varied in-plane fiber orientation from $\theta = 0°$ to $90°$

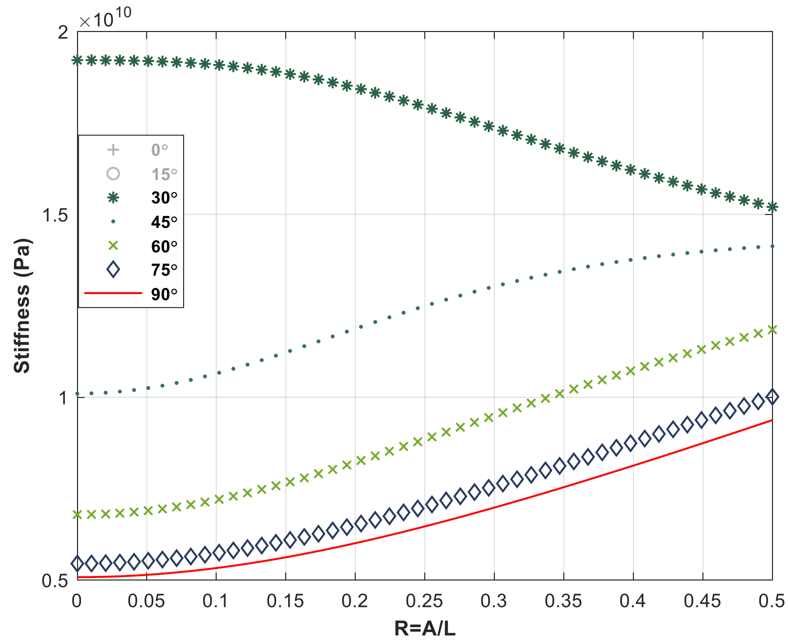

Figure 5-16 $\bar{E}_{\text{x}}$ vs R, $\theta = 30°$ to $90°$

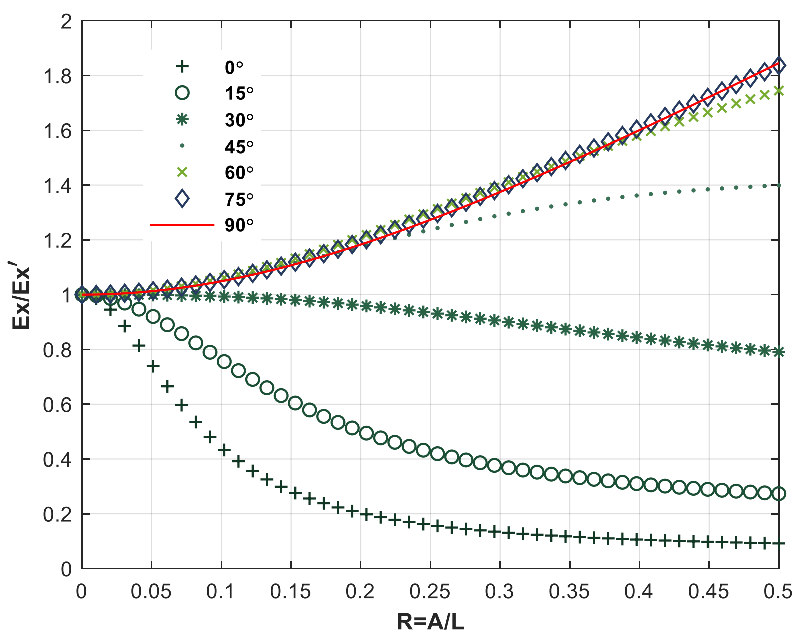

Figure 5-17 Normalized $\bar{E}_{\text{x}}$ vs R, $\theta = 0°$ to $90°$

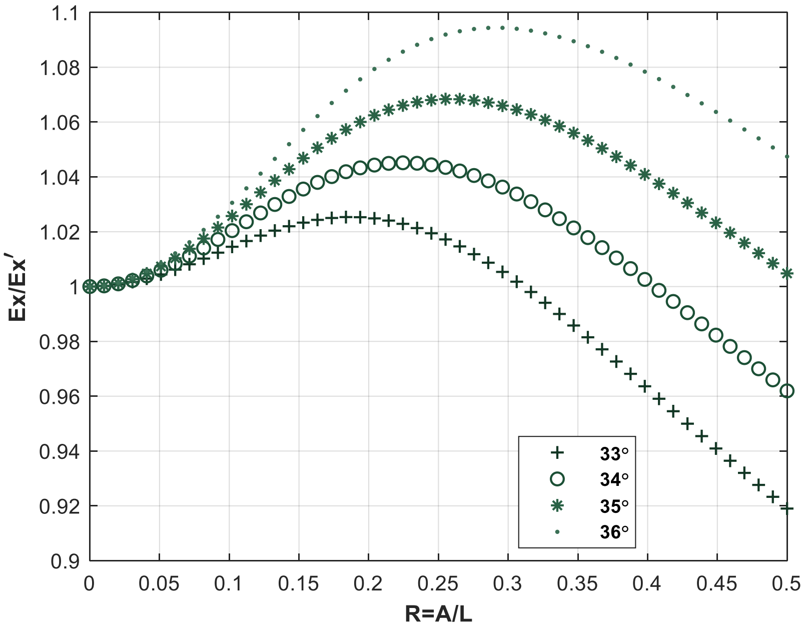

Figure 5-18 Normalized $\bar{E}_x$ vs R, $\theta = 33°$ to $36°$

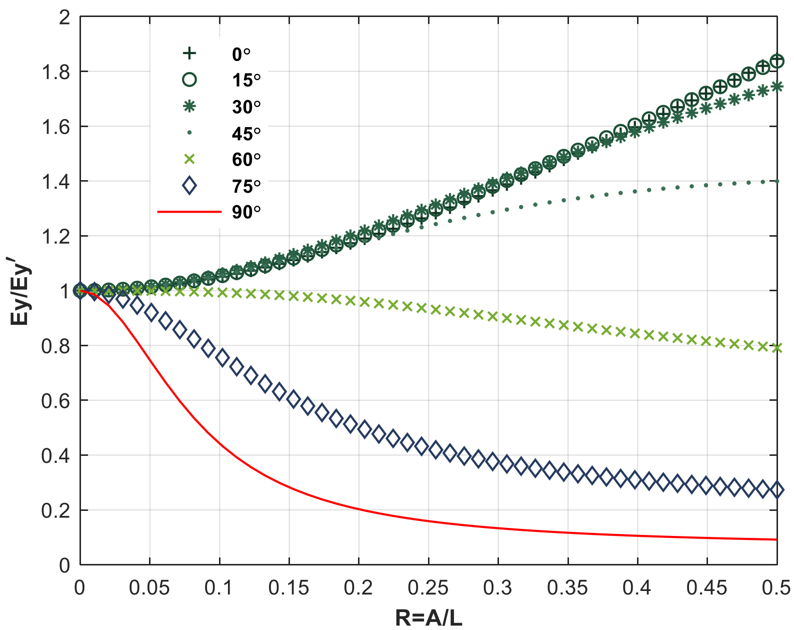

Figure 5-19 Normalized $\bar{E}_y$ vs R, $\theta = 0°$ to $90°$

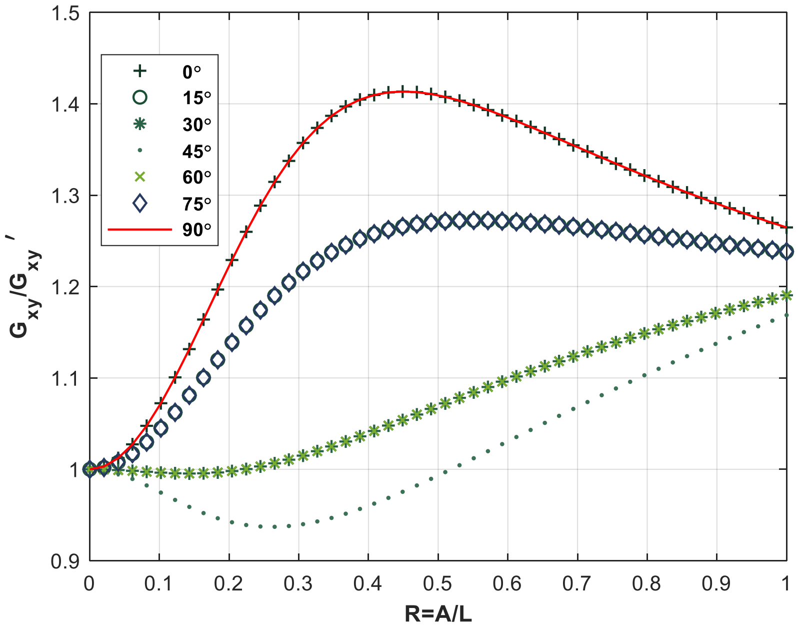

Figure 5-20 Normalized G_{xy} vs R, $\theta = 0°$ to $90°$

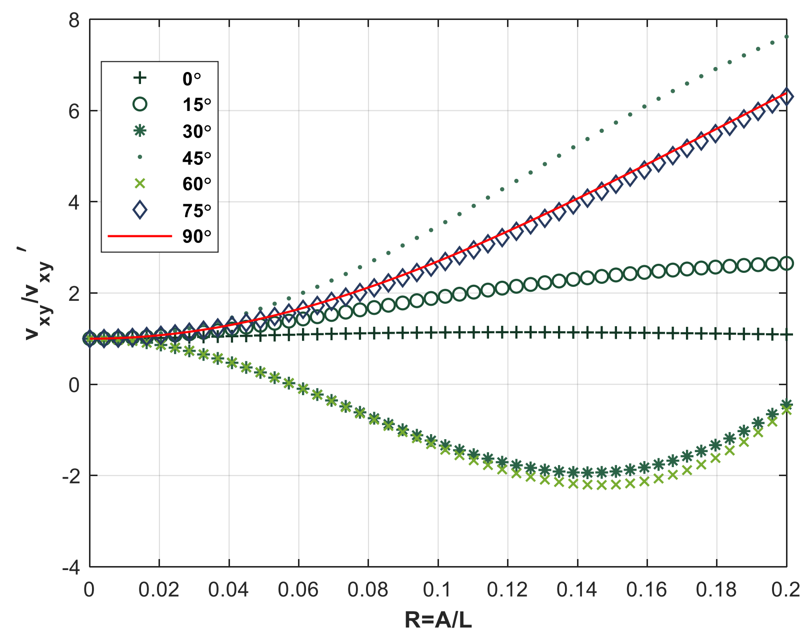

Figure 5-21 Normalized $\bar{v}_{xy}$ vs R, $\theta = 0°$ to $90°$

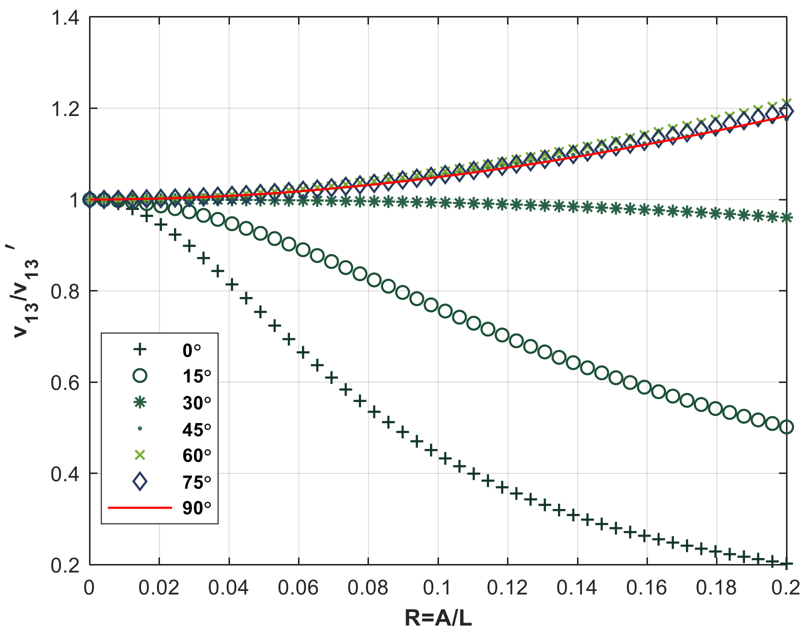

Figure 5-22 Normalized $\bar{v}_{xz}$ vs R, $\theta = 0°$ to $90°$

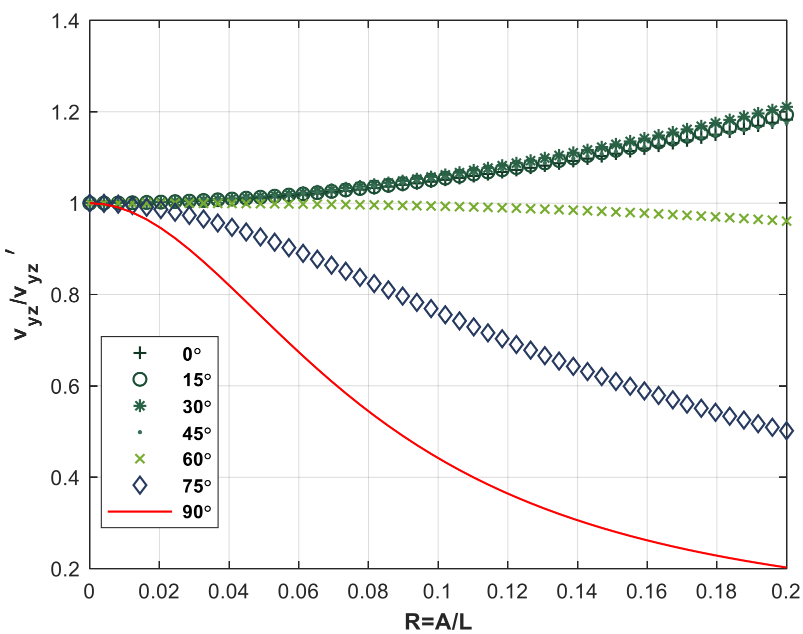

Figure 5-23 Normalized $\bar{v}_{yz}$ vs R, $\theta = 0°$ to $90°$

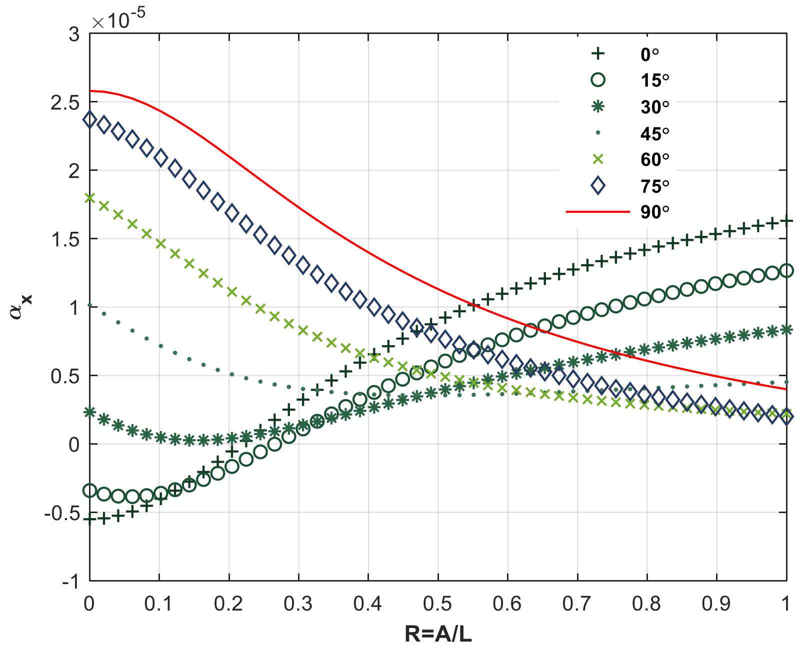

Figure 5-24 $\bar{\alpha}_x$vs R, θ = 0° to 90°

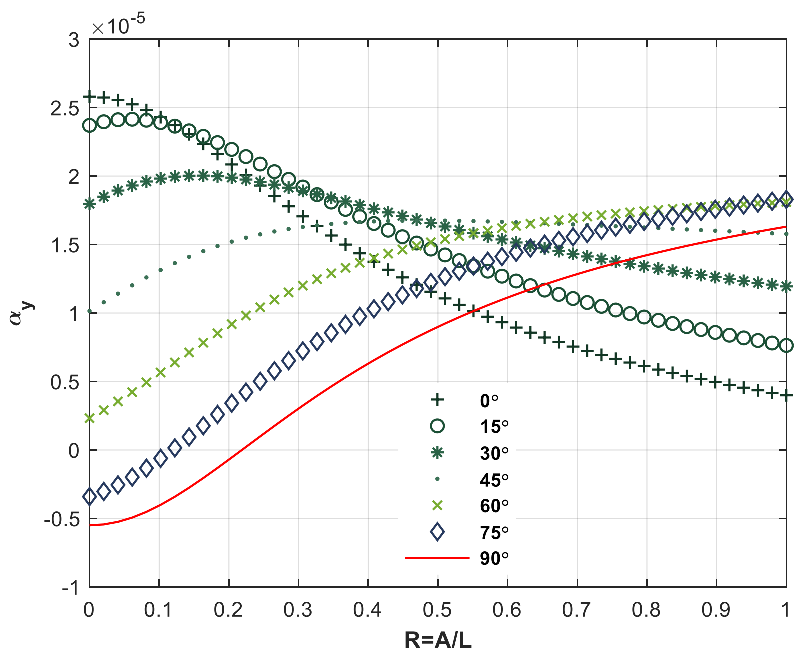

Figure 5-25 $\bar{\alpha}_y$vs R, θ = 0° to 90°

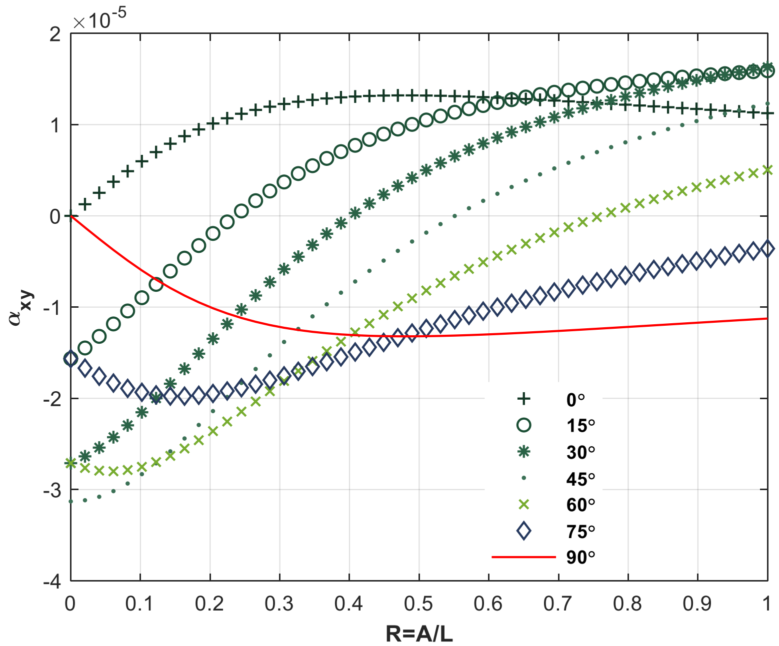

Figure 5-26 $\bar{\alpha}_{xy}$vs R, $\theta = 0°$ to 90°

Effective Young's modulus along x-direction is shown in Figure 5-15 with fiber orientation θ varied from 0° to 90°. When fiber orientation is 0°, significant stiffness reduction is observed as fiber waviness parameter R increases. When fiber orientation is 15°, approximately 64 % stiffness reduction is observed when R varies from 0 to 0.3. In can be concluded that stiffness reduction is significant for small degree of fiber orientation. Effective Young's modulus along x-direction is shown in Figure 5-16 with fiber orientation θ varied from 30° to 90°. Stiffness increment is observed when $\theta < 45°$ when R varies from 0 to 0.5 due to more portion of fibers align in y-direction than x-direction. The normalized Young's modulus versus R with θ varies from 0° to 90° is presented in Figure 5-17. According to Figure 5-17, stiffness along the x-direction increases when $\theta > 30°$. Figure 5-18 shows normalized Young's modulus along the x-direction verse R

whne θ varies from 33° to 36°. When $\theta = 34.5°$, the stiffness increment is less than 4 %. Effective Young's modulus along x-direction is shown in Figure 5-19 with fiber orientation θ varied from 0° to 90°. It should be noted that the normalized stiffness between $\bar{E}_{\mathrm{x}}$ and $\bar{E}_{\mathrm{y}}$ are compensate with each other. That is $\bar{E}_{\mathrm{x}}(0°) = \bar{E}_{\mathrm{y}}(90°)$, $\bar{E}_{\mathrm{x}}(15°) = \bar{E}_{\mathrm{y}}(75°)$, $\bar{E}_{\mathrm{x}}(30°) = \bar{E}_{\mathrm{y}}(60°)$, $\bar{E}_{\mathrm{x}}(45°) = \bar{E}_{\mathrm{y}}(45°)$ for an any given fiber waviness parameter R.

The normalized $\bar{G}_{xy}$ versus R for fiber orientation varies from 0° to 90° is shown in Figure 5-20. If lamina 1 has fiber orientation θ_1 and lamina 2 has fiber orientation θ_2, $\bar{G}_{xy}(\theta_1) = \bar{G}_{xy}(\theta_2)$ if $\theta_1 + \theta_2 = 90°$. Normalized $\bar{v}_{xy}$ versus R with θ varies from 0° to 90° is shown in Figure 5-21. When fiber waviness parameter R increases, it should be mentioned that the in-plane Poisson's ratio v_{12} is insignificant for a lamina with 0° fiber orientation but it is more pronounced for a lamina with 45° fiber orientation. Normalized $\bar{v}_{xz}$ and $\bar{v}_{yz}$ versus R with θ varies from 0° to 90° is shown in Figure 5-22 and Figure 5-23, respectively. Based on the observation, $\bar{v}_{xz}(\theta_1)$ and $\bar{v}_{yz}(\theta_2)$ are compensate with each other if $\theta_1 + \theta_2 = 90°$.

$\bar{\alpha}_x$ versus R for fiber orientation θ varies from 0° to 90° is shown in Figure 5-24. When $\theta < 30°$, negative CTE is observed when $R < 0.3$. When R is approximately equal to 0.3, zero CTE is observed as $\theta < 30°$. When $R > 0.3$, positive CTE is observed as $\theta < 30°$. This means deformation in x-direction is changed from contraction to expansion under thermal condition when $\theta < 30°$. For $\theta > 30°$, the $\bar{\alpha}$ behavior is opposite compared the ones has $\theta < 30°$. $\bar{\alpha}_{\mathrm{y}}$ versus R for fiber orientation θ varies from 0° to 90° is shown in Figure 5-25. It should be noted that the distribution for $\bar{\alpha}_{\mathrm{x}}$ and $\bar{\alpha}_{\mathrm{y}}$ for an any given R and θ is symmetric with respect to the horizontal line, when $\alpha = 10^{-5}/K°$. Finally, $\bar{\alpha}_{xy}$ versus R for fiber orientation θ varies from 0° to 90° is shown in Figure 5-26. It is more pronounced for $\theta > 75°$ because negative CTE is observed.

5.8.3. Effects of Fiber Waviness Parameter R

This section we discussed effect of fiber orientation with respect to fiber waviness ratio R. This section, effect of R with respect to fiber orientation is discussed. Normalized effective Young's modulus $\bar{E}_{\mathrm{x}}$ along the x-direction with respect to fiber orientation is shown in Figure 5-27. When fiber orientation increases from =0° to 90°, $\bar{E}_{\mathrm{x}}$ reduces significantly if no fiber waviness occurs. When $R > 0.5$, maximum $\bar{E}_{\mathrm{x}}$ occurs at $\theta = 30°$ due to more fibers align along in the longitudinal or x-direction. On the other hand, Normalized effective Young's modulus $\bar{E}_{\mathrm{y}}$ along the y-direction with respect to fiber orientation is shown in Figure 5-28 which has opposite distribution compared with $\bar{E}_{\mathrm{x}}$ distribution shown in Figure 5-27. For rest of $G_{xy}, G_{yz}, G_{xz}, v_{12}, v_{23}, v_{13}, \alpha_x, \alpha_y$ and α_{xy} fiber waviness parameter effects can be founded in APPENDIX C.

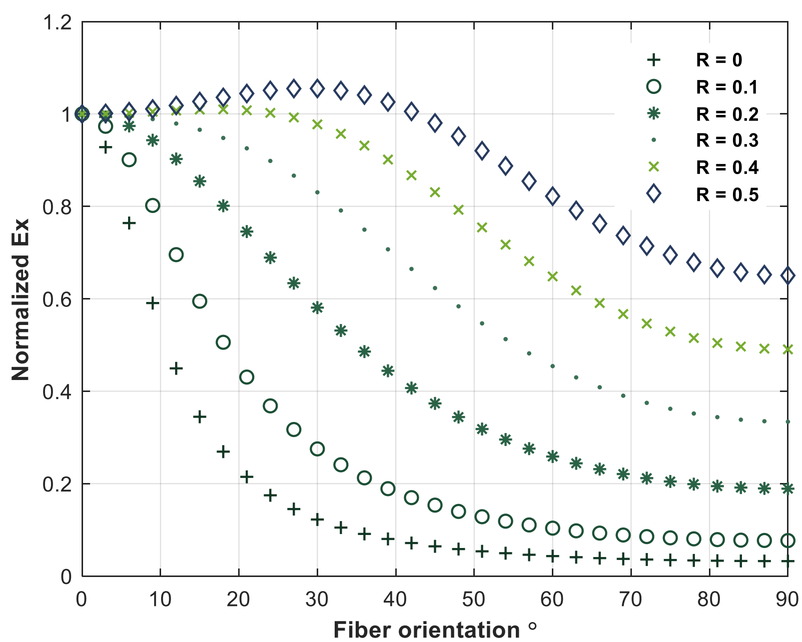

Figure 5-27 $\bar{E}_{\mathrm{x}}$ comparison between fiber orientation and waviness ratio R.

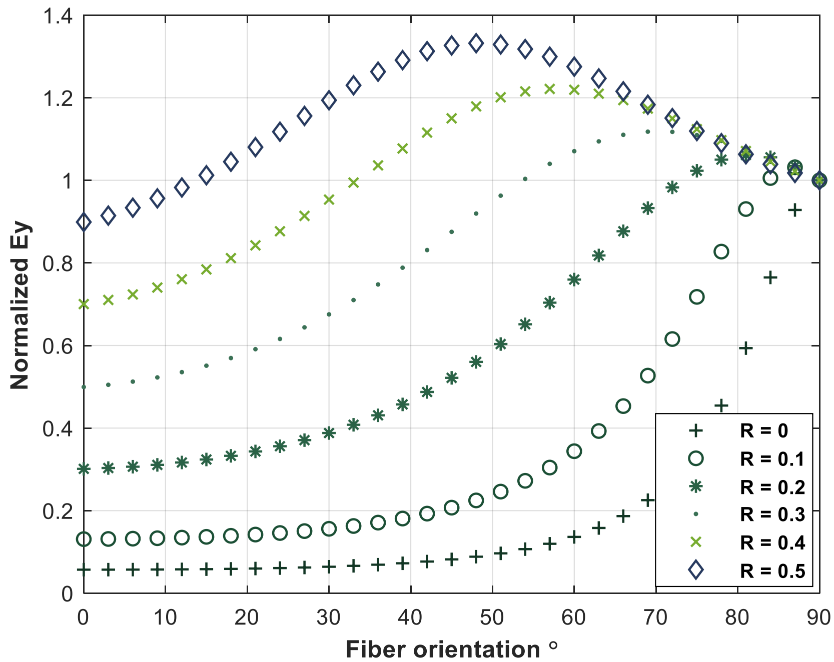

Figure 5-28 $\bar{E}_{\mathrm{y}}$ comparison between fiber orientation and waviness ratio R.

5.8.4. Incremental Load Study of In-Plane Fiber Waviness of 0° Lamina

During incremental loading, the fiber waviness amplitude, fiber waviness length, and fiber length are changed. As a result, the effective stiffness properties of the ply with fiber waviness is also changed. Therefore, it is necessary to recalculate material properties at each step of stress increment. In this section, a lamina with in-plane fiber waviness subjected with incremental tension and compression will be discussed. Numerical example with fiber waviness length $L = 3$ in, and fiber waviness amplitude $A = 1.5$ in is selected. Iterating process is terminated as applied σ_x reaches to $0.7\,X_T$, where X_T is tensile strength of IM7/8552, $X_T = 2811\,MPa$ and the subjected incremental tensile and compressive load is $\Delta\sigma_{\mathrm{x}}$ = 10 MPa. The first case, if tension is considered, the amplitude variation versus accumulated loading along x-direction is shown in Figure 5-29.

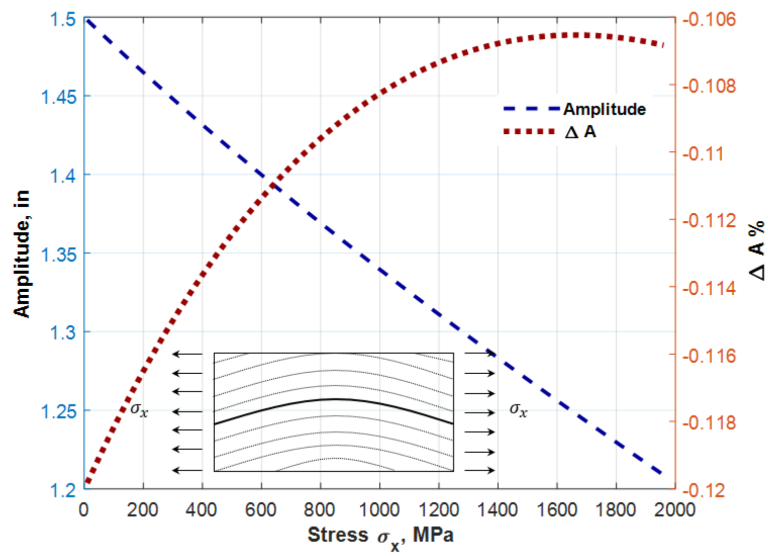

Figure 5-29 The amplitude, A, vs σ_x under tension for 0° lamina

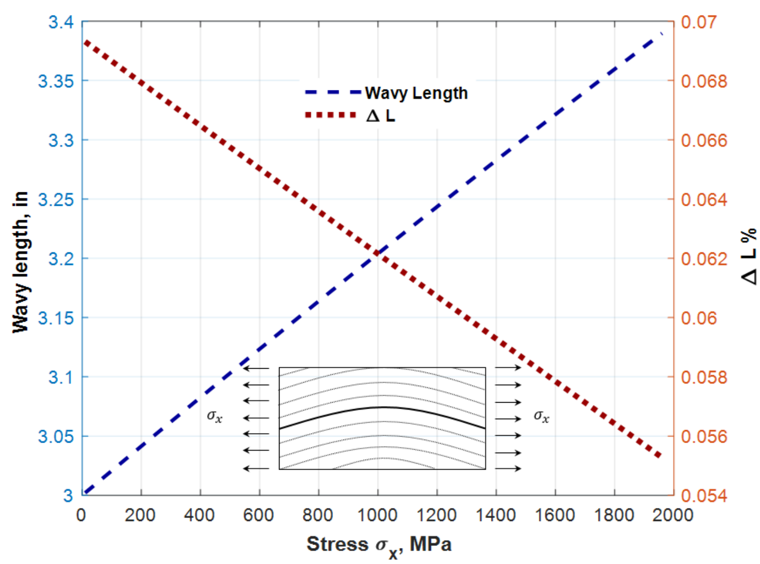

Figure 5-30 The wavy length L, vs σ_x under tension for 0° lamina

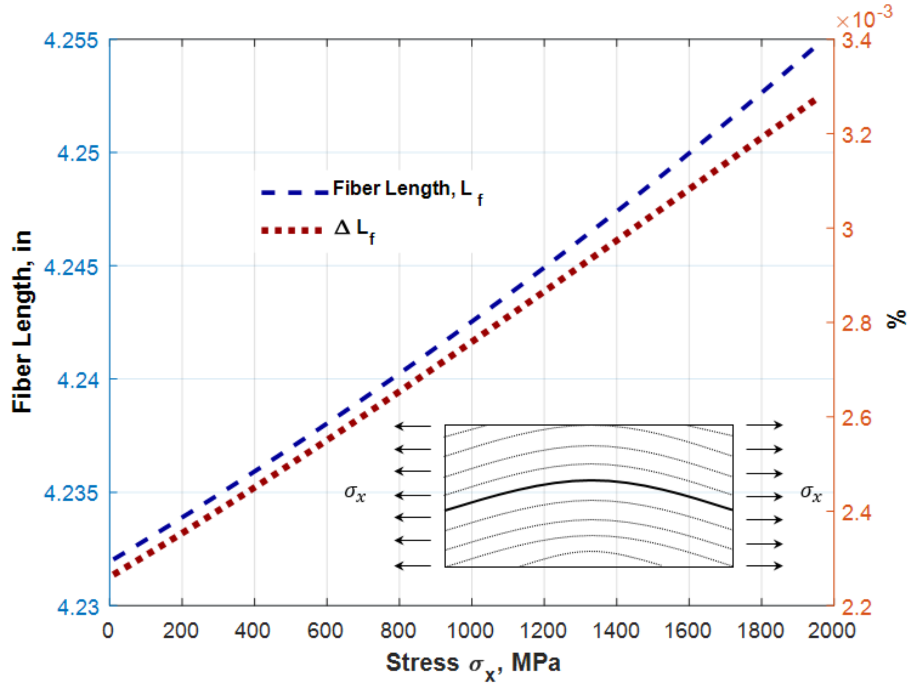

Figure 5-31 The fiber length, L_f, vs σ_x under tension for 0° lamina

According to Figure 5-29, the fiber waviness amplitude decreases as increasing loading in x-direction. The rate of changing the amplitude gradually increases and reaches to maximum -0.108 % when $\sigma_x = 1600$ MPa. Since small incremental stress is applied along x-direction, an incremental strain can be induced, so fiber waviness length can be updated. According to Figure 5-30, fiber waviness length increases when loading increases. The fiber waviness length increases 13.05 % from 3 in to 3.3916 in. However, the rate of changing fiber waviness length linearly decreases due to Young's modulus becomes stiffer. Young's modulus in longitudinal direction $\bar{E}_x$ increases with increasing σ_x. Note that the rate of change modulus raises with loading because more fibers align in the longitudinal direction. Therefore, updated fiber waviness length, fiber length, and the corresponding amplitude are sensitive to stiffness properties.

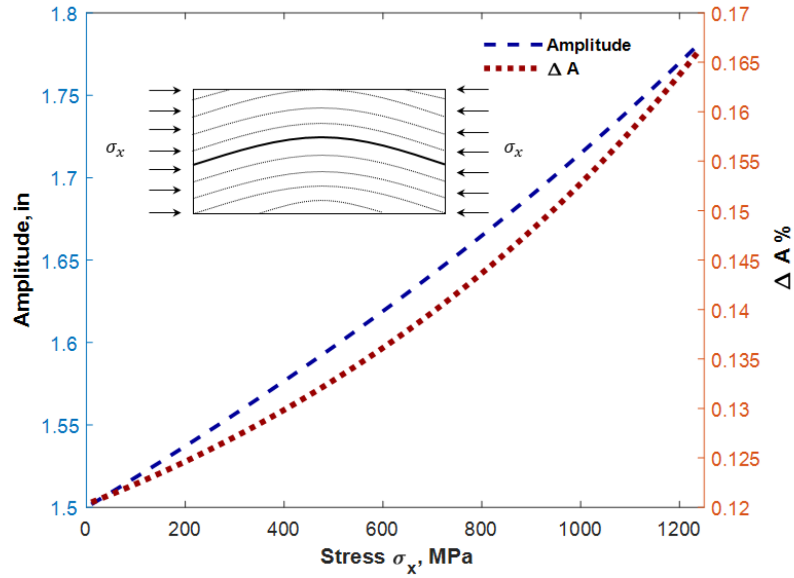

Figure 5-32 The amplitude, A, vs σ_x under compression for 0° lamina

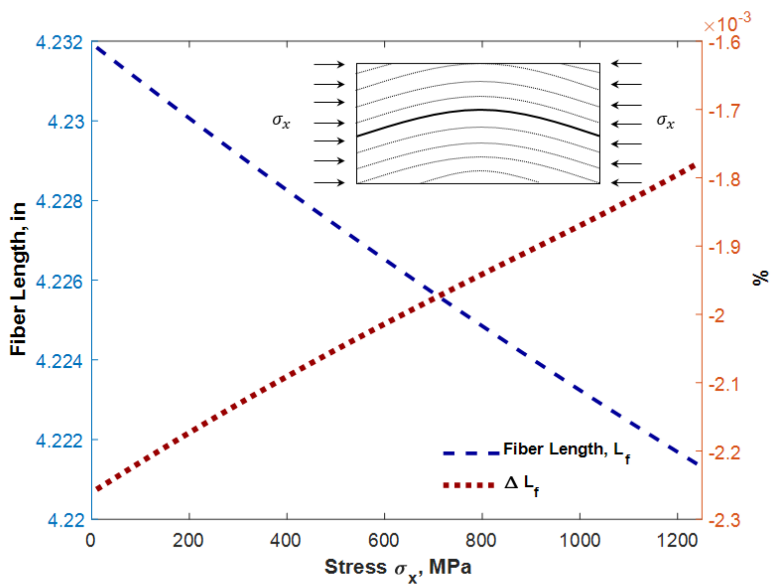

Figure 5-33 The fiber length, L_f, vs σ_x under tension for 0° lamina

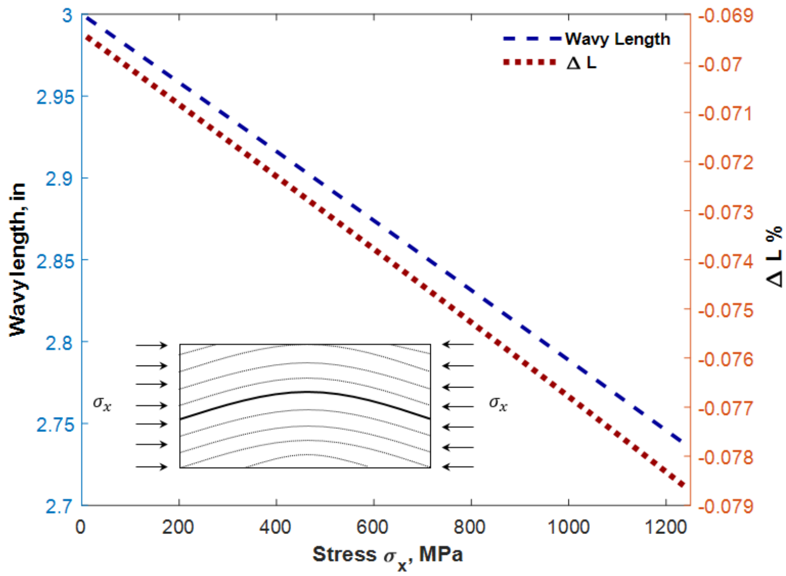

Figure 5-34 The wavy length, L, vs σ_x under compression for 0° lamina

On the other hand, if compression is considered, fiber waviness amplitude increases when compressive loading increases. In addition, Fiber waviness length L decreases when compressive loading increases. Thus, the updated Young's modulus along the x-direction is 11.73 % lower than its original value if 1200 MPa in compression is applied.

Effect of iteration number also plays and important role on obtaining updated amplitude, length fiber waviness shape properties. Updated fiber waviness length, fiber length and corresponding fiber waviness amplitude are sensitive with absence stiffness properties. To reach desired tensile stress, a small incremental stress is applied, and the stiffness properties will be updated every iterations. The accumulative variation may end up different updated wavy length, fiber length, and the amplitude of waviness even the desired stresses are identical. A numerical study will be presented in this section. The accumulative stress is assumed to be 600 MPa and $\Delta\sigma_x$ is 600 MPa, 300 MPa, 150 MPa, 75 MPa, 20 MPa, 10 MPa, 5 MPa, and 1

MPa, respectively. The corresponding iteration numbers will be 1, 2, 4, 8, 30, 60, 120, and 600. The effect of iteration numbers under certain tensile loading is shown in Table 5-4. According to Table 5-4, 8 iterations will be sufficient to calculate updated properties. This is an optimal number since less iterations may lead to inaccurate output but it is very time consuming if large iteration number is considered. The difference between results using 8 iterations and 600 iterations is less 0.15 %.

Table 5-4 Effect of iteration numbers under tension for 0° lamina with L = 1.5 m

Iteration number		1	2	4	8	30	60	120	600
ε_x	Accumulative	0.0806	0.0605	0.0504	0.0454	0.0417	0.0410	0.0407	0.04039
A (m)	Original A	1.5	1.5	1.5	1.5	1.5	1.5	1.5	1.5
	Update A	1.307	1.353	1.376	1.387	1.396	1.398	1.398	1.3995
	% Diff	-12.8	-9.79	-8.25	-7.47	-6.90	-6.79	-6.74	-6.70
L_f (m)	Original L_f	4.232	4.232	4.232	4.232	4.232	4.232	4.232	4.232
	Update L_f	4.244	4.241	4.239	4.238	4.238	4.238	4.238	4.2381
	% Diff	0.29	0.22	0.18	0.16	0.15	0.14	0.14	0.14
L_w (m)	Original L_w	3.0	3.0	3.0	3.0	3.0	3.0	3.0	3.0
	Update L_w	3.246	3.185	3.154	3.138	3.127	3.125	3.124	3.1237
	% Diff	8.23	6.17	5.14	4.63	4.25	4.18	4.15	4.12
$\bar{E}_x$ $(10^{10}\ Pa)$	Original $\bar{E}_x$	1.441	1.441	1.441	1.441	1.441	1.441	1.441	1.441
	Update $\bar{E}_x$	1.538	1.537	1.537	1.537	1.537	1.537	1.537	1.5371
	% Diff	6.77	6.72	6.69	6.68	6.67	6.67	6.67	6.67

5.8.5. Out-of-Plane Fiver Waviness for $\theta°$ Laminate

Effect of stack sequence of $[\pm\theta, 0_2, 90_2]_s$ is studied in this section. The average stiffness properties are obtained from rotating in-plane 0° properties with fiber waviness to out-of-plane fiber waviness. After rotating respect to x-axis, the stiffness matrix can be rotated based on given stacking sequence. According to Figure 5-35 and Figure 5-36, significant axial and bending stiffness reduction are observed for 0° fiber orientation laminate. According to Figure 5-37, G_{xy} is maximum when $\theta = 45°$. Rest of G_{xz}, G_{yz}, G_{xy} are shown in Appendix C.

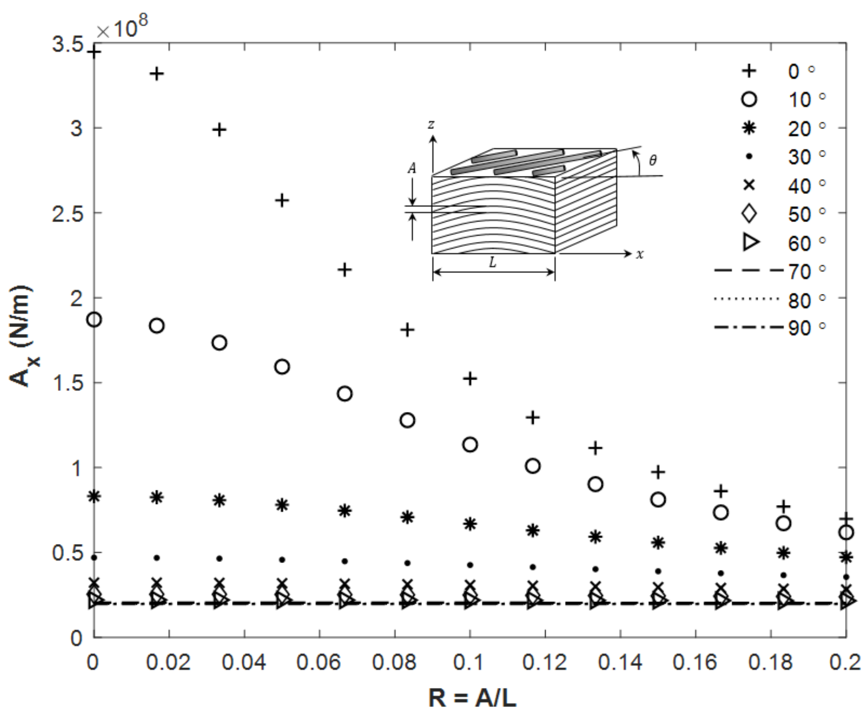

Figure 5-35 Equivalent axial stiffness comparison with stack sequence $[\pm\theta, 0_2, 90_2]_s$

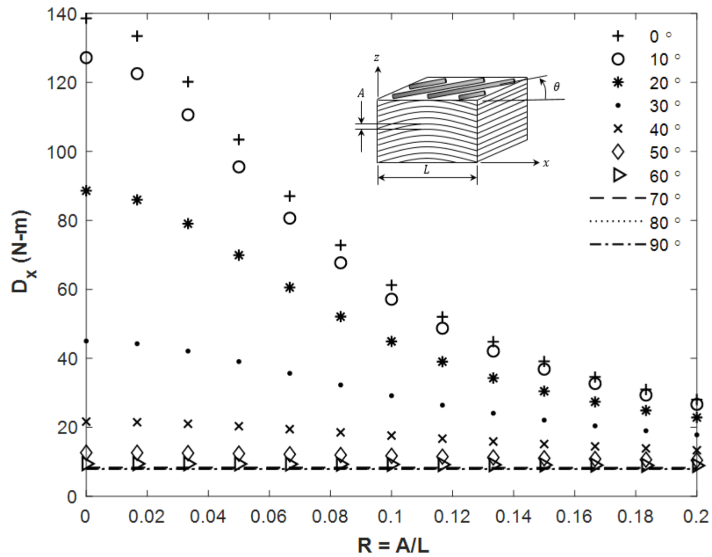

Figure 5-36 Equivalent bending stiffness comparison with stack sequence $[\pm\theta, 0_2, 90_2]_s$

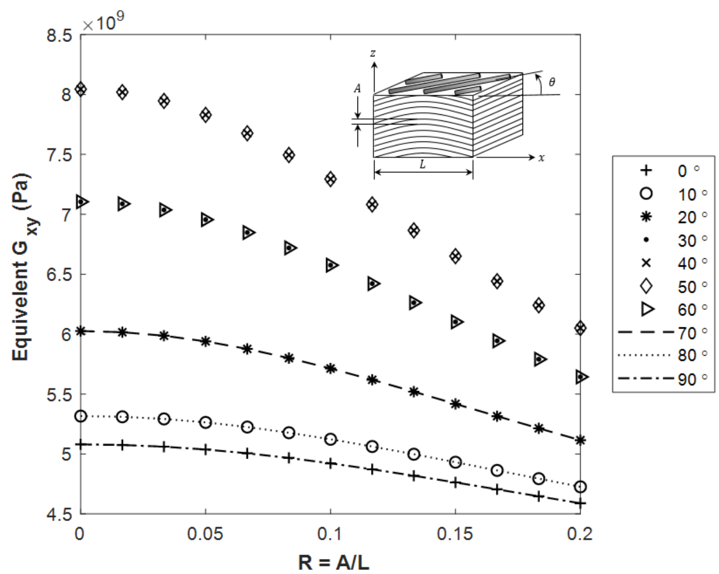

Figure 5-37 Equivalent shear modulus in x-y plane comparison with stack sequence $[\pm\theta, 0_2, 90_2]_s$

5.8.6. In-Plane Fiber Waviness of 0° Curved Lamina

A multi-comparisons between a lamina with and without initial curvature and fiber waviness is discussed and shown in Figure 5-38. According to Figure 5-38, the bending stiffness obtained using NB assumption is higher than results using general and WB assumptions. The bending stiffness results with curvature is higher than results without curvature. For comparison between a curved lamina with and without fiber waviness, $R = 0.05$ is selected to investigate bending stiffness reduction and approximately 25 % stiffness reduction is observed

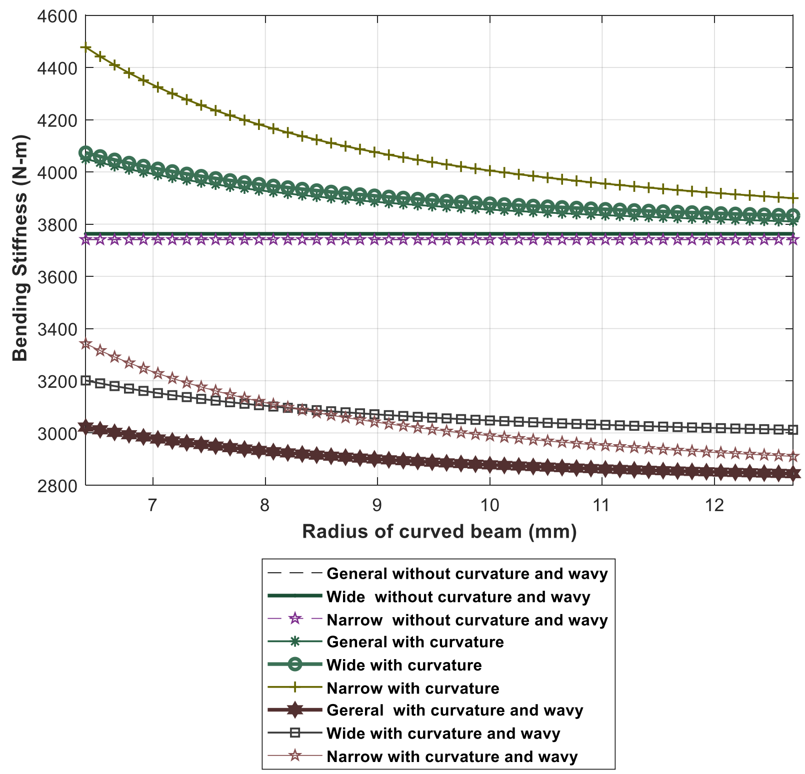

Figure 5-38 Comparison between general, wide, narrow beam with / without curvature and in-plane fiber waviness.

5.8.7. Out-of-Plane Fiber Waviness of 0° Curved Laminate

A single out-of-plane fiber waviness in the unidirectional composite curved beam is investigated in this section. The inner radius is 6.4 mm and the outer radius is 12.7 mm. The maximum amplitude of fiber waviness is selected at the 15^{th} ply, and the top and bottom plies with no amplitude are selected at 5^{th} and 33^{rd} plies. Fiber waviness initiates at $\theta = 20°$ and ends at $\theta = 70°$ as shown in Figure 5-39. Comparison for axial and bending stiffness for composite beam with and without curvature and wavy is shown in Table 5-5. Both axial and bending stiffness are higher for composite curved beam than composite straight beam. Since imperfection fiber waviness is introduced, both axial and bending stiffness in composite curved beam with fiber waviness are less than composite curved beam without fiber waviness

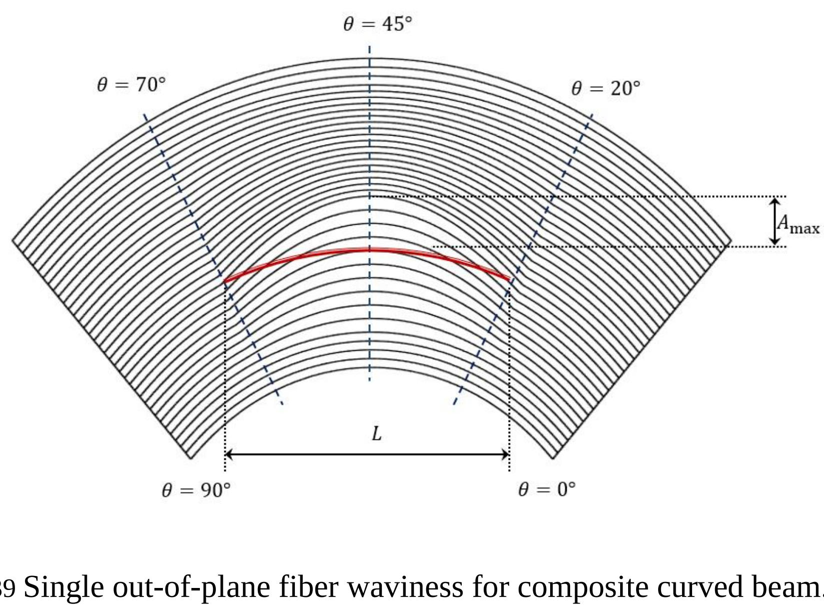

Figure 5-39 Single out-of-plane fiber waviness for composite curved beam.

Table 5-5 Comparison of axial and bending stiffness for composite beam with and without curvature and wavy, respectively.

		Ax	Dx
Straight	Perfect	1.032E9	3.733 E3
	Wavy	7.832E8	3.480 E3
Curved	Perfect	1.034 E9	3.864 E3
	Wavy	7.917 E8	3.633 E3

For a given fiber waviness amplitude approximately equals to 10% of total thickness of composite curved beam with 10 wavy plies, the effect of fiber waviness in different thickness location can be investigated. The fiber waviness angle is still initiates at $20°$ and ends up at $70°$, where $\mathrm{LA}_{\mathrm{end}}^{bot}$ is location of bottom layer with zero amplitude, $\mathrm{LA}_{\mathrm{end}}^{top}$ is location of top layer with zero amplitude of fiber waviness. $\mathrm{LA}_{\mathrm{max}}$ is the ply location with maximum amplitude. According to Table 5-6, bending stiffness reaches to maximum when the location of fiber waviness is approximately located in the middle axis along longitudinal direction.

Effect of fiber waviness amplitude is investigated. $\mathrm{LA}_{\mathrm{end}}^{bot}$ is selected to be 5^{th} layer and $\mathrm{LA}_{\mathrm{end}}^{top}$ is selected to be 34^{th} layer. The location which contains maximum fiber waviness amplitude is chosen to be 14^{th} layer. The maximum amplitude varied from 0% to 30% out of thickness of curved beam are investigated. The results are shown in Table 5-7. As amplitude increases, both axial and bending stiffness decrease. It is more pronounced for axial stiffness since significant axial stiffness reduction is observed as amplitude increases.

Table 5-6 Parameter study for location of fiber waviness for composite curved beam.

$\mathrm{LA}_{\mathrm{end}}^{bot}$ (ply)	$\mathrm{LA}_{\max}$ (ply)	$\mathrm{LA}_{\mathrm{end}}^{top}$ (ply)	A_{x}^{narrow} (N/m)	$\mathrm{D}_{\mathrm{x}}^{narrow}(N-m)$
1	5	10	9.746 E8	3.427 E3
5	10	15	9.751 E8	3.729 E3
15	15	20	9.792 E8	3.852 E3
20	20	25	9.812 E8	3.827 E3
25	25	30	9.824 E8	3.758 E3
30	30	35	9.831 E8	3.651 E3

Table 5-7 Parameter study for amplitude of fiber waviness for composite curved beam.

Amplitude	A_{x}^{narrow} (N/m)	$\mathrm{D}_{\mathrm{x}}^{narrow}(N-m)$
0 %	1.0343 E9	3.8636 E3
5 %	9.8178 E8	3.8213 E3
10 %	8.7894 E9	3.7224 E3
15 %	7.8364 E8	3.6071 E3
20 %	7.0825 E8	3.4947 E3
25 %	6.4996 E8	3.3914 E3
30%	6.0435 E8	3.2982 E3

5.8.8. Maximum Radial Stress Prediction for Composite Curved Beam with Out-of-Plane Fiber Waviness under Bending

Maximum radial stress can be predicted well using closed-form solution provided by [5] for a perfect curved beam without fiber waviness. However, maximum radial stress will relocate and vary if fiber waviness is introduced. The σ_r comparison between present method using Eqs. (5-14) and FE results with and without fiber waviness is shown in Figure 5-40. The σ_r distribution has excellent agreement with FE results. The maximum σ_r predicted from present method is 48.00 MPa and maximum σ_r obtained from FE analysis is 49.85 MPa. The error percentage is less than 4 % between the result from present method and FE analysis. Moreover, the location which has maximum σ_r using present method is $\mathrm{r} = 10.27$ mm, and the location which has maximum σ_r using FE analysis is $\mathrm{r} = 10.26$ mm. The error percentage is less than 1 % between the result from present method and FE analysis.

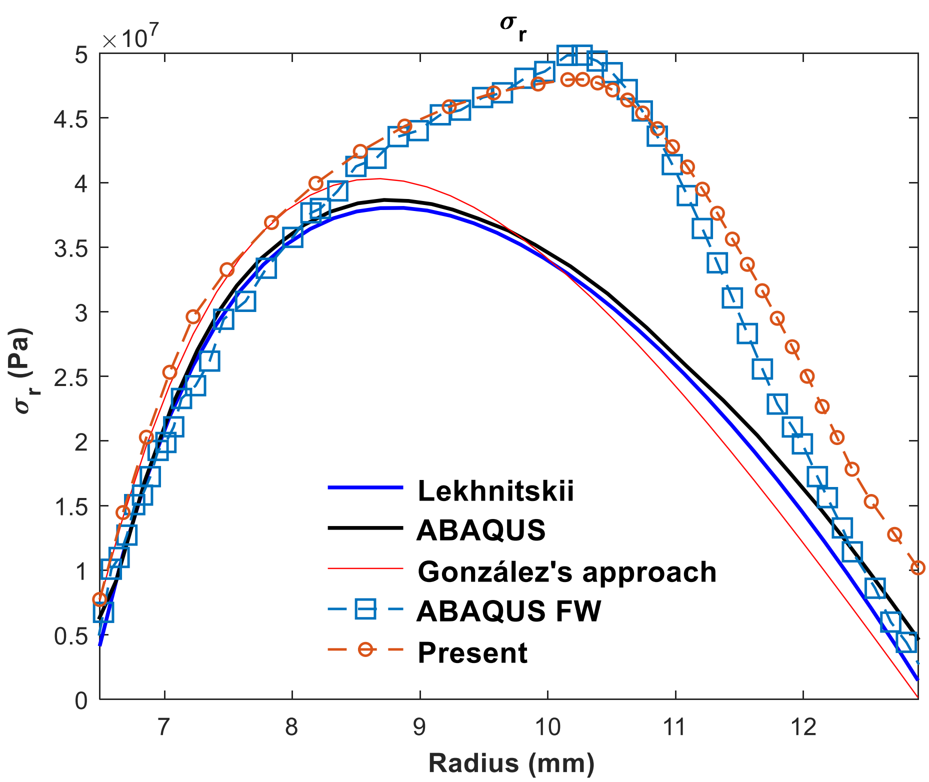

Figure 5-40 Comparison between present and FE results with and without fiber waviness

5-9 Conclusion

A closed-form analytical solution is developed for analyzing laminated composite beam with and without initial curvature and fiber waviness, respectively. The explicit expressions for evaluating axial and bending stiffness are formulated based upon modified lamination theory and taking into consideration the structural deformation characteristics of beam with narrow section. Closed-form solutions are also provided to analyze composite beam with in-plane and out-of-plane fiber waviness. Incremental loading schematic is introduced and a practical iteration number is selected. FE analysis is conducted to verify results using present approach. The maximum radial stress for a composite curved beam with out-of-plane fiber waviness under bending is discussed. The present stiffness and stress results are in good agreement with numerical results obtained from ANAQUS. It is found that the geometry of fiber waviness such as location where has maximum amplitude and the maximum amplitude of fiber waviness has a great impact on equivalent axial and bending stiffness. However, fiber waviness has less impact on the bending stiffness of plies affected by fiber waviness are near the middle axis of the composite curved beam. It is concluded that the present approach can provide an efficient method for analyzing laminated composite curved beam with in-plane and out-of-plane fiber waviness.

Chapter 6

COMPOSITE CURVED BEAM WITH DELAMINATION

Interface cracking is the most common failure mechanism in laminated structures. Fracture mechanics have been widely implemented to aim this type of failure mode where strain energy release rate (ERR) in the mixed mode are evaluated in order to investigate crack initiation and propagation. The crack starts to propagate when the strain ERR reaches to the critical strain ERR $\mathrm{G_T} = G_c = G_I + G_{II}$. Several authors [74-76] provided analytical closed-form solutions to predict the required strain ERR of crack propagation However, they observed that the analytical approaches can only satisfy the strain ERR results for larger cracks, $\theta_c > 8°$ compared with results obtained from numerical solutions. In addition, only a crack symmetric with respect to the middle span of the curved beam is considered in their approaches. Therefore, this study aims to fill this void by developing an analytical analysis for a composite curved beam with a delamination which can be located in any interface and any hoop location.

6-1 Symmetrical Model Formulation

Lu et al. [73] considered a circumferential crack in a composite curved beam under bending. Superposition method of a prefect curved beam under bending and a curved beam with a crack subjected to opening radial stress is applied as shown in Figure 6-1. In addition, they studied strain ERR with respect to crack length by using FE analysis. Roberta and Brian [75] conducted an analytical approach for calculation strain ERR and compared with results provided by [72]. However, if a small crack ($\frac{\theta_c}{2} < 5°$) is considered, the analytical results are not accurate compared with results from FE analysis. A novel analytical approach is developed in this research by extending the closed-form solution provided by [75].

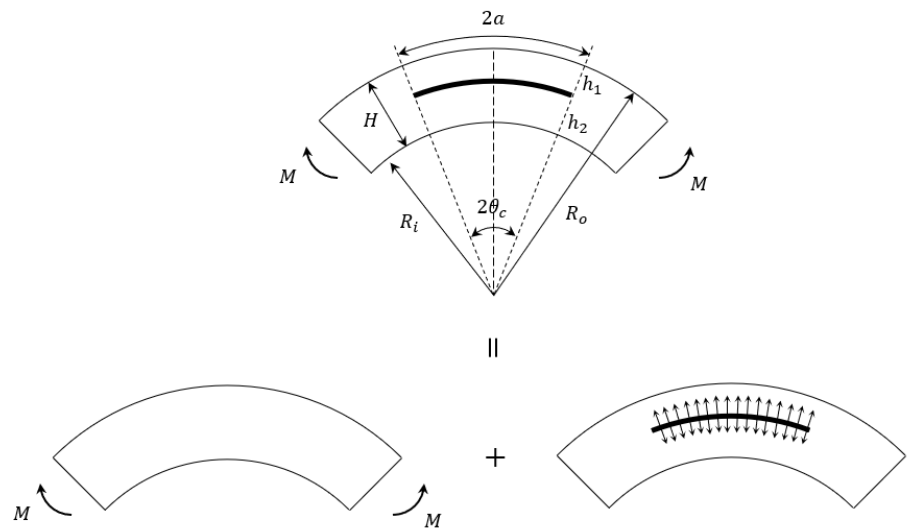

Figure 6-1 Superposition method for a curved beam with a delamination under bending from Lu et al [57].

Figure 6-2 shows the geometry and configuration of the symmetric model. The beam below the crack is denoted as beam 1 and the beam above the crack is denoted as beam 2. The perfect beam without crack is denoted as beam 3. The moment and force resultants under bending moment $\mathrm{M_o}$ are denoted as $\mathrm{N_i}$ and $\mathrm{M_i}$, respectively, where $\mathrm{i} = 1$ and 2. $\mathrm{R_o}$ is the outer radius of the curved beam and $\mathrm{R_i}$ is the inner radius, and $\mathrm{R_c}$ is the radius of the crack. For a given beam under opening bending moment $\mathrm{M_o}$, the upper part above the neutral axis of the beam is under compression and the lower part below the neutral axis is under tension as shown in Figure 6-3. The unit axial forces applied on the beam 1 and 2 can be computed as $\mathrm{N_1} = \sigma_\theta^1(R_v - R_i)/w$, and $\mathrm{N_2} = \sigma_\theta^2(R_o - R_c)/\mathrm{w}$ so the tangential stress distribution for beam 1 can be achieved by considering a beam subjected to a moment M_1 plus a axial force N_1. The tangential stress distribution in beam 2 can be contributed by a beam subjected a moment M_2 and an axial force N_2.

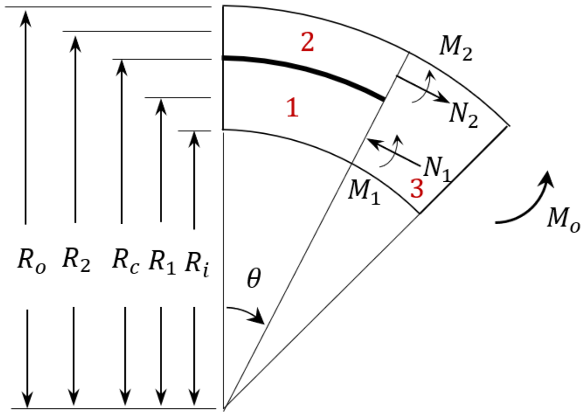

Figure 6-2 Symmetrical model configuration and moment and force resultants under bending.

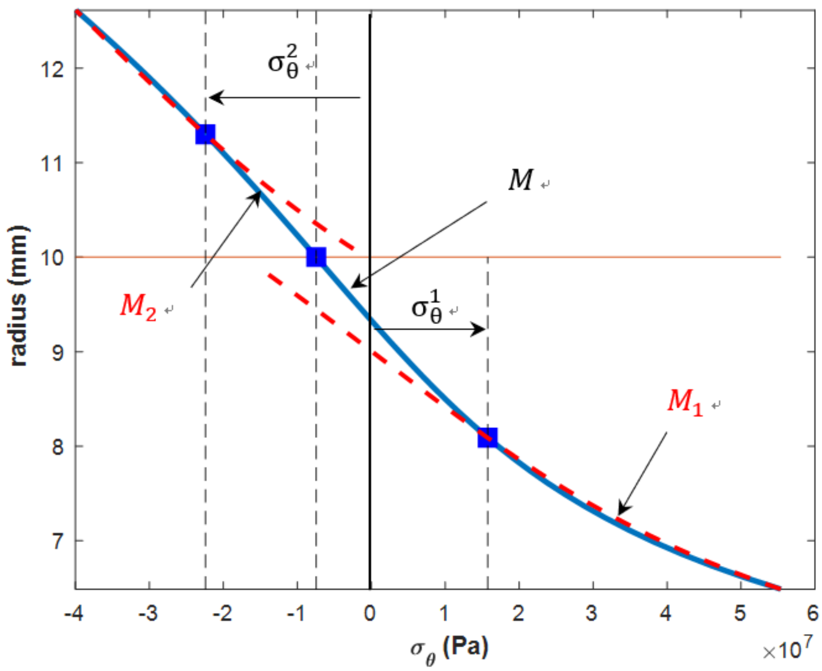

Figure 6-3 Tangential stress distribution σ_θ under opening bending moment M_o.

It should be noted that all the force and moment resultants need to satisfy the equilibrium equations below as shown in Figure 6-4:

$$N_1 + N_2 = 0$$
$$\mathrm{M}_1 + M_2 - \frac{N_1 h_1}{2} + \frac{N_2 h_2}{2} - M_3 = 0 \tag{6-1}$$

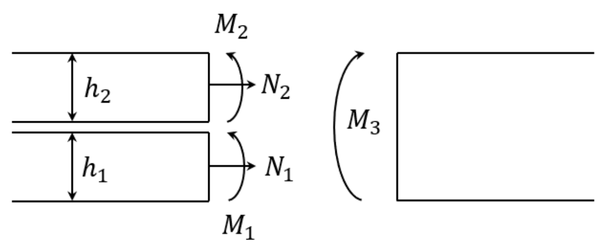

Figure 6-4 Bi-layer beam moment and force resultants.

The internal force and moment distribution are varied with respect to the crack angle θ for a curved beam under end bending moment and axial force. The internal axial, shear forces and moment distribution varied with respect to θ for beam 1 and beam 2 can be expressed as

$$N(\theta)_i^{internal} = N_i \cos(\theta)$$
$$Q(\theta)_i^{internal} = N_i \sin(\theta) \tag{6-2}$$
$$M(\theta)_i^{internal} = M_i + N_i\, R_i(1 - \cos(\theta))$$

where i = 1 and 2.

Since superposition method is considered, the total forces and moments variation with respect to θ are $N(\theta)_i^{total} = N(\theta)_i^{internal} + N(\theta)_i^{open}$, $Q(\theta)_i^{total} = Q(\theta)_i^{internal} + Q(\theta)_i^{open}$, and $M(\theta)_i^{total} = M(\theta)_i^{internal} + M(\theta)_i^{open}$ where

$N(\theta)_i^{open}, Q(\theta)_i^{open}, M(\theta)_i^{open}$ are axial force, shear force and moment due to opening stress mentioned in Figure 6-1.

$$
\begin{aligned}
N(\theta)_i^{open} &= -q_i \sin(\theta/2) \\
Q(\theta)_i^{open} &= q_i \cos(\theta/2) \\
M(\theta)_i^{open} &= -q_i R_i \sin(\theta/2\ )
\end{aligned}
\tag{6-2}
$$

where $q_i = \sigma_r(r)\ R_i\theta$, i = 1 and 2. $\sigma_r(r)$ can be found in Eqs. (4-16).

Thus, the total strain energy release rate can be obtained by following equation:

$$
\begin{aligned}
G_T(\theta) = \frac{1}{2R_c}\Bigg\{ & R_1\left(\frac{{N(\theta)_1^{total}}^2}{EA_1} + \frac{{M(\theta)_1^{total}}^2}{EI_1} + \frac{{Q(\theta)_1^{total}}^2}{GA_1}\right) \\
& + R_2\left(\frac{{N(\theta)_2^{total}}^2}{EA_2} + \frac{{M(\theta)_2^{total}}^2}{EI_2} + \frac{{Q(\theta)_2^{total}}^2}{GA_2}\right) \\
& - R_3\left(\frac{M_o^2}{EI_3}\right)\Bigg\}
\end{aligned}
\tag{6-3}
$$

where EA, EI, and GA are effective axial stiffness, bending stiffness, and shear stiffness in Eqs. (4-5) and (4-6). It should be noticed unit forces and unit moment are assumed in Eqs. (6-3). However, Eqs. (6-3) cannot accurately predict total strain ERR. Therefore, a modified equation $G_T^m(\theta)$ based on non-dimensional coefficients is proposed by comparing results obtained from Eqs. (6-3) and results obtained from FE analysis.

$$G_T^m(\theta) = \alpha\, \beta\, G_T(\theta) \tag{6-4}$$

The coefficient α is a parameter related to radial effect of crack location and the coefficient β is a parameter related to crack length effect.

$$\alpha = -25.254R_p^5 + 90.6Rp^4 - 101.29R_p^3 + 36.879R_p^2 - 1.5689R_p + 3.5294$$

$$\beta = \frac{-(y_1)\log(\theta) + (y_2)}{y_3} \tag{6-5}$$

where

$$\mathrm{y}_1 = (0.007006t^2 + 0.6156356t - 0.2455147) \tag{6-6}$$

$$\mathrm{y}_2 = 0.26848t^2 + 1.102285t + 4.3770866$$

$$\mathrm{y}_3 = -(y_1)\log(16.6) + (y_2)$$

and t is the total thickness of composite curved beam in the unit of (mm). θ is the crack angle in the unit of (degree), and $\mathrm{R_p}$ is the crack location ratio where $\mathrm{R_p} = (R_c - R_i)/(R_o - R_i)$

6-2 Unsymmetrical Model Formulation

The configuration of unsymmetrical model is shown in Figure 6-5. θ_h is the hoop angle locating with respect to the middle length of the crack. The angle of left crack tip is denoted as θ_s. The angle of right crack tip is denoted as θ_e, where *s* is start angle, and *e* is end angle of the crack where $\theta_h = (\theta_s + \theta_e)/2$. The lower part of the beam is denoted as beam 1, and the upper part of the beam is denoted as beam 2. Beam 3 and 4 are beams without crack as shown in Figure 6-5. Considering the total strain ERR on the left crack tip, it can be obtained by using Eqs. (6-3) but beam 3 should be replaced with beam 4.

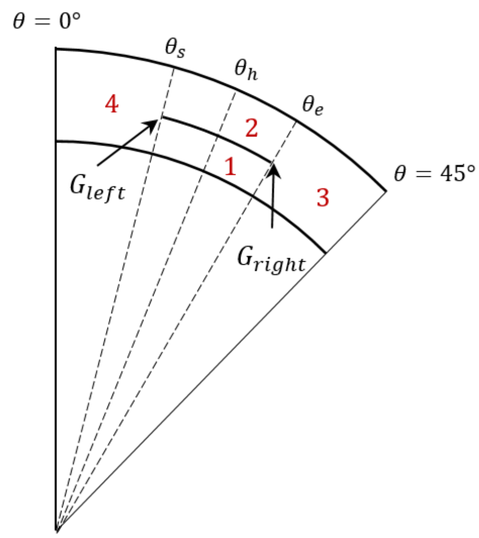

Figure 6-5 Configuration of unsymmetrical model

$$G_{T_{left}}(\theta) = \frac{1}{2R_c}\left\{R_1\left(\frac{N(\theta)_1^{total^2}}{EA_1} + \frac{M(\theta)_1^{total^2}}{EI_1} + \frac{Q(\theta)_1^{total^2}}{GA_1}\right) + R_2\left(\frac{N(\theta)_2^{total^2}}{EA_2} + \frac{M(\theta)_2^{total^2}}{EI_2} + \frac{Q(\theta)_2^{total^2}}{GA_2}\right) - R_4\left(\frac{M_o^2}{EI_4}\right)\right\} \tag{6-7}$$

where $R_4 = R_3$ and $EI_4 = EI_3$. The crack angle θ is varied from 0° to $\theta_h - \theta_s$. The total strain ERR on the right crack tip can be obtained using similar approach in Eqs. (6-3) where θ is varied from 0° to $\theta_e - \theta_h$. It should be noted that regularized model is applied for a curved beam with a small initial curvature only. The stress distribution for a curved composite beam under bending is assumed to be independent of θ if regularized model is considered. However, if moderate and large initial curvatures are considered for a curved beam under bending, non-regularized model has to be applied. The stress distribution of non-regularized model is assumed to be independent of θ within a certain range. According to González [82], the non-regularized angle $\theta_{\mathrm{nr}} = 23.32°$ is introduced for a composite curved beam where the radius to thickness ratio is 1.5. This ratio is similar to the ratio applied in the present approach, which is 1.51. Based on their model, a linear equation to describe reduced σ_{r} which is a function of crack angle θ_{ck} is introduced as

$$\begin{gathered} \sigma_{\mathrm{r}}^{new} = \sigma_r \, \mathrm{P} \\ \mathrm{P} = (-2.29277\ \theta_{ck}\ + 148.174)/100 \end{gathered} \tag{6-8}$$

where P is the percentage, θ_{ck} is the crack angle in the unit of degree. According to their σ_{r} results, for a given interface but varied with hoop angle, σ_{r} remains constant until $\theta = \theta_{\mathrm{nr}}$, and starts to decrease 52 % when $\theta = 45°$. Linear variation of P is assumed as shown in Eqs. (6-8).

The strain ERR based on beam 1, 2, and 4 has higher value compared to the one in the right composed by beam 1, 2, and 3 under end bending moment. The equivalent force per unit width due to opening stress σ_{r} within the region where $\theta_{\mathrm{s}} < \theta < \theta_h$ and $\theta_{\mathrm{s}} > \theta_{nr}$ can be written as

$$q_{i_{left}} = \sigma_{\mathrm{r}_{\mathrm{left}}}^{new} R_i \theta \tag{6-9}$$

where θ is varied from 0° to $\theta_{\mathrm{h}} - \theta_s$, i = 1 and 2. $\sigma_{\mathrm{r}_{\mathrm{left}}}^{new} = \sigma_r P$, where θ_{ck} is $(\theta_{\mathrm{s}}+\theta_{\mathrm{h}})/2$. The equivalent force per unit width due to opening stress σ_{r} within the region where $\theta_{\mathrm{h}} < \theta < \theta_e$ and $\theta_{\mathrm{s}} > \theta_{nr}$ can be written as

$$q_{i_{right}} = \sigma_{r_{right}}^{new} \, R_i \theta \qquad (6\text{-}10)$$

where θ is varied from $0°$ to $\theta_e - \theta_h$, $i = 1$ and 2. $\sigma_{r_{right}}^{new} = \sigma_r \, P$, where θ_{ck} is $(\theta_h + \theta_e)/2$. Once reduced q_i is obtained, the total strain ERR for a crack locates in any hoop location is obtained using Eqs. (6-2) to (6-4).

6-3 Finite Element Analysis

An ABAQUS based non-linear FE analysis is developed to simulate structural response of a composite curved beam with a crack. The failure load under bending, and the strain ERR in Mode I and II are investigated. A unidirectional laminated curved beam is considered. The inner radius of the curved beam is 6.4 mm and the outer radius 12.7 mm. The width of the beam is 12.7 mm. IM7/8552 carbon-epoxy composite material properties are implemented.

6.3.1. Model Formulation

Delamination is located at the interface between upper and lower laminates. Thus, two sub-laminate system is implemented in order to simulate delamination using Virtual Crack Closure Technique (VCCT) [85]. The upper surface of the lower beam is chosen as the master surface and the lower surface of the upper beam is chosen as the slave surface as shown in Figure 6-6. Discrete material orientation is considered since unidirectional laminated beam is implemented as shown in Figure 6-6, where 1 is the fiber direction. During mesh process, it should be noticed that element numbers between slave surface and master surface has to be identical because nodes on the master and slave surfaces will be bonded. The bonded node set has to be selected from nodes on the slave surface. All the nodes on the slave surface have to be selected excepted nodes at which the initial crack is applied with. Since non-linear crack propagation analysis is considered, when the step is being editing, non-linear effects and large displacements control option called "NIgeom" needed to be opened. In addition, maximum number of increments is selected to be 1000. The initial increment size is 0.01, the maximum increment size is 0.1, and minimum increment size is 10^{-20} because large computational steps will take place. Types for selected step called "Surface-to-surface contact (Standard)" is implemented. The node to surface discretization method is chosen. The bonded nodes set is specifying the initially bonded nodes of the slave surface in debond using VCCT crack. The contact properties for VCCT BK mixed mode behavior [86] is imputed as $\mathrm{G_{Ic}} = 0.277\frac{N}{mm}, \mathrm{G_{IIc}} = G_{IIIc} = 0.777\frac{N}{mm}$, and the parameter $\mathrm{n} = 2.6645$ for IM7/8552 material [87].

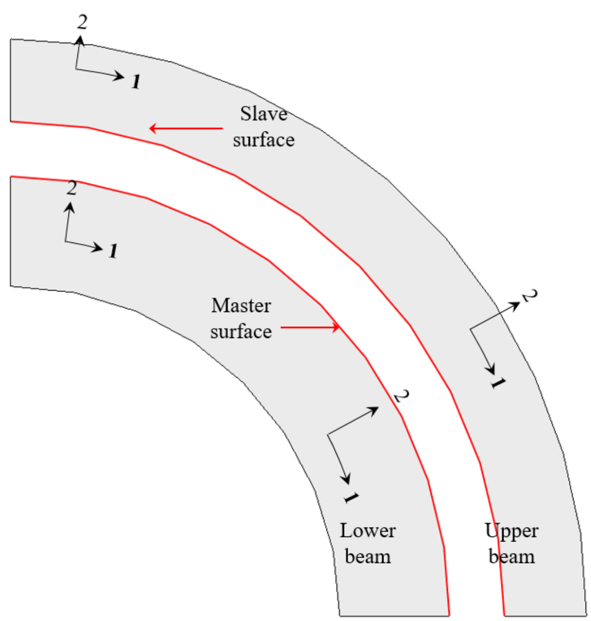

Figure 6-6 Definition of master and slave surfaces.

Two numerical cases are provided in this section.

$$\text{Case 1: } R_i = 6.4\ mm \quad R_o = 12.7mm$$

$$\text{Case 2: } R_i = 12\ mm \quad R_o = 16mm$$

Figure 6-7 shows stress distribution of σ_{11}, σ_{22}, and τ_{12} for a composite curved beam with crack locates at middle axis of the beam.

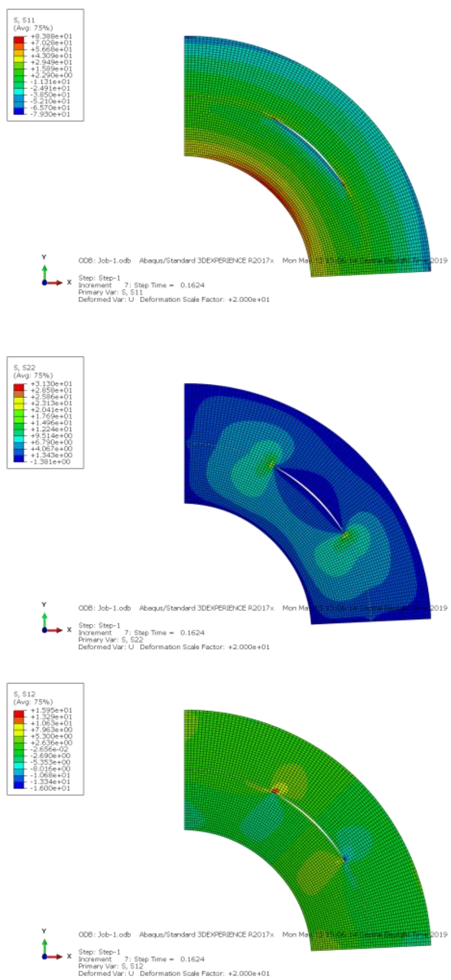

Figure 6-7 σ_{11}, σ_{22}, and τ_{12} stress distribution for a composite curved beam with a crack under bending.

6-4 Results and Discussion

6.4.1. Radial Effect

In this study, the crack is located in any radial location when $0 < \mathrm{R_p} < 1$ as shown in Figure 6-8. A constant moment $\mathrm{M_o} = 2.956\, N - m$ is applied to investigate $\mathrm{G_T}$ obtained from present approach and compared with results from FE-analysis implemented by ABAQUS. The configuration of the curved beam, applied moment, crack radial location and total strain ERR from ABAQUS is shown in Table 6-1.

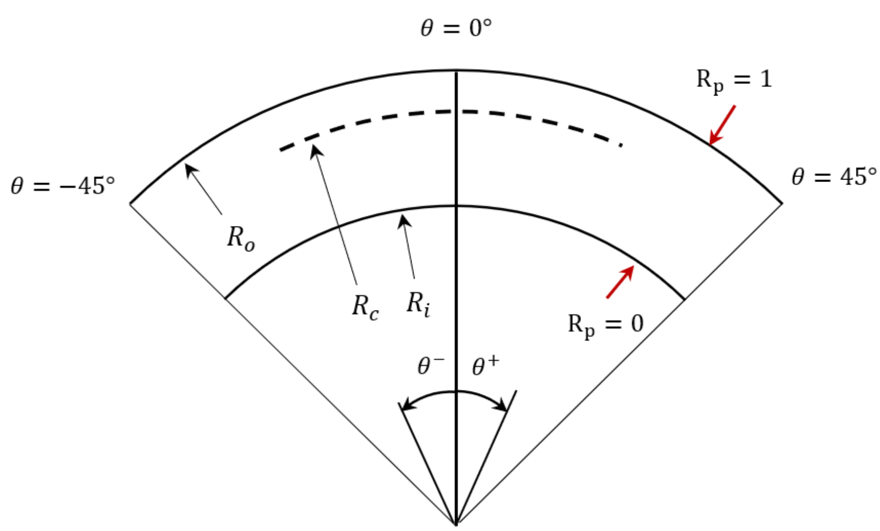

Figure 6-8 Crack location radial effect parameter definition.

Table 6-1 Crack location radial effect parameters and strain ERR results obtained from FE analysis (case 1).

θ^+	θ^-	R_i	R_o	R_c	R_p	M_o	G_I^{FE}	G_{II}^{FE}	$\frac{G_I^{FE}}{G_{II}^{FE}}$	G_T^{FE}
16.2	-16.2	6.4	12.7	7.03	10%	2956	134.167	3.68	2.74%	137.85
16.2	-16.2	6.4	12.7	7.66	20%	2956	201.85	8.8	4.36%	210.65
16.2	-16.2	6.4	12.7	8.29	30%	2956	244.512	14.04	5.74%	258.55
16.2	-16.2	6.4	12.7	8.92	40%	2956	260.695	18.15	6.96%	278.85
16.2	-16.2	6.4	12.7	9.55	50%	2956	245.735	20.36	8.29%	266.10
16.2	-16.2	6.4	12.7	10.18	60%	2956	204.205	20.78	10.18%	224.99
16.2	-16.2	6.4	12.7	10.81	70%	2956	148.029	20.28	13.70%	168.31
16.2	-16.2	6.4	12.7	11.44	80%	2956	89.06	19.96	22.41%	109.02
16.2	-16.2	6.4	12.7	12.07	90%	2956	33.65	20.52	60.98%	54.17

where the unit of radius is *mm*, the unit of moment is *N-mm*, the unit of θ is in degree, and the unit of strain ERR is N/m.

The total strain ERR comparison between present method and results obtained from ABAQUS is tabulated in Table 6-2. G_T^p is the total strain ERR obtained from present method, and G_T^{FE} is the total strain ERR using FE analysis implemented by ABAQUS. The comparison is also shown in Figure 6-9. All the results obtained from present method have excellent agreement with ABAQUS's results except when $\mathrm{R_p} = 0.1$.

The geometry and applied moment in second case are tabulated in Table 6-3. The comparison between the total strain ERR results obtained from the present method and ABAQUS are tabulated in Table 6-4 and is shown in Figure 6-10. The total strain energy increase as $\mathrm{R_p}$ increases. It reaches to maximum when $\mathrm{R_p} \cong 0.33$. It should be more pronounced that the crack is located near the neutral axis of the curved beam. In conclusion, the present method has excellent accuracy at predicting the total strain ERR results where the crack can be located in any radial interface.

Table 6-2 Total strain ERR comparison between present method and ABAQUS (case 1).

θ^+	θ^-	R_i	R_o	R_c	R_p	M_o	G_T^p	G_T^{FE}	*% Diff.*
16.2	-16.2	6.4	12.7	7.03	10%	2956	137.85	125	9.32%
16.2	-16.2	6.4	12.7	7.66	20%	2956	210.65	213	-1.12%
16.2	-16.2	6.4	12.7	8.29	30%	2956	258.55	252	2.53%
16.2	-16.2	6.4	12.7	8.92	40%	2956	278.85	269	3.53%
16.2	-16.2	6.4	12.7	9.55	50%	2956	266.10	253	4.92%
16.2	-16.2	6.4	12.7	10.18	60%	2956	224.99	219	2.66%
16.2	-16.2	6.4	12.7	10.81	70%	2956	168.31	164	2.56%
16.2	-16.2	6.4	12.7	11.44	80%	2956	109.02	116	-6.40%
16.2	-16.2	6.4	12.7	12.07	90%	2956	54.17	56.3	-3.93%

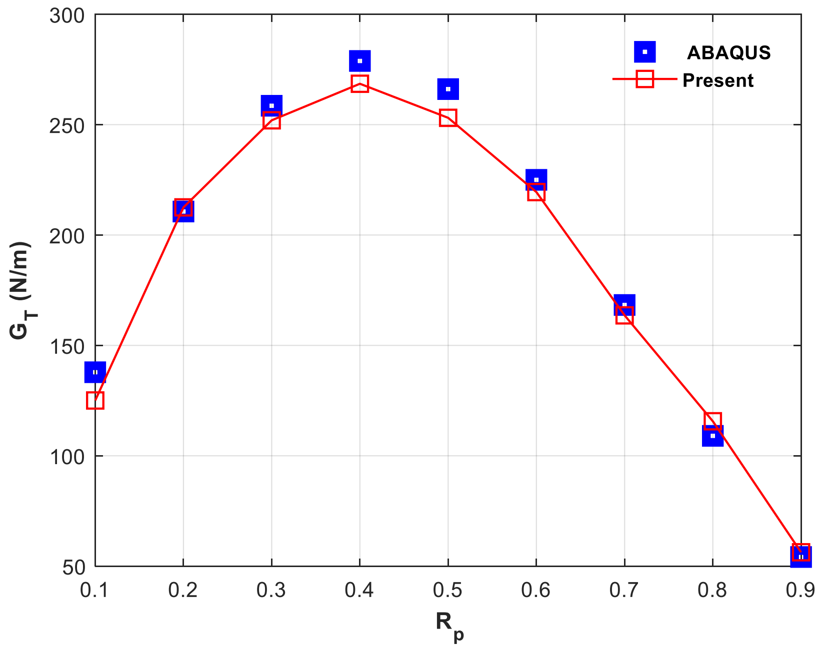

Figure 6-9 G_T comparison between present method and ABAQUS (case 1).

Table 6-3 Crack location radial effect parameters and strain ERR results obtained from FE analysis (case 2).

θ^+	θ^-	R_i	R_o	R_c	R_p	M_o	G_I^{FE}	G_{II}^{FE}	$\frac{G_I^{FE}}{G_{II}^{FE}}$	G_T^{FE}
16.2	-16.2	12	16	12.4	10%	1497	89.764	3.51	3.91%	93.27
16.2	-16.2	12	16	12.8	20%	1497	199.933	4.52	2.26%	204.45
16.2	-16.2	12	16	13.2	30%	1497	255.985	9.24	3.61%	265.23
16.2	-16.2	12	16	13.6	40%	1497	268.702	16.15	6.01%	290.24
16.2	-16.2	12	16	14	50%	1497	246.51	23.63	9.59%	277.14
16.2	-16.2	12	16	14.4	60%	1497	200.662	30.82	15.36%	231.48
16.2	-16.2	12	16	14.8	70%	1497	142.296	37.56	26.40%	179.86
16.2	-16.2	12	16	15.2	80%	1497	79.48	43.35	54.54%	122.83
16.2	-16.2	12	16	15.6	90%	1497	18.77	39.23	209.00%	58.00

Table 6-4 Total strain ERR comparison between present method and ABAQUS (case 2).

θ^+	θ^-	R_i	R_o	R_c	R_p	M_o	G_T^p	G_T^{FE}	*% Diff.*
16.2	-16.2	12	16	12.4	10%	1497	103	93.27	-10.43%
16.2	-16.2	12	16	12.8	20%	1497	206	204.45	-0.76%
16.2	-16.2	12	16	13.2	30%	1497	265	265.23	0.08%
16.2	-16.2	12	16	13.6	40%	1497	299	290.24	-3.02%
16.2	-16.2	12	16	14	50%	1497	285	277.14	-2.84%
16.2	-16.2	12	16	14.4	60%	1497	243	231.48	-4.98%
16.2	-16.2	12	16	14.8	70%	1497	177	179.86	1.59%
16.2	-16.2	12	16	15.2	80%	1497	120	122.83	2.30%
16.2	-16.2	12	16	15.6	90%	1497	55.5	58.00	4.31%

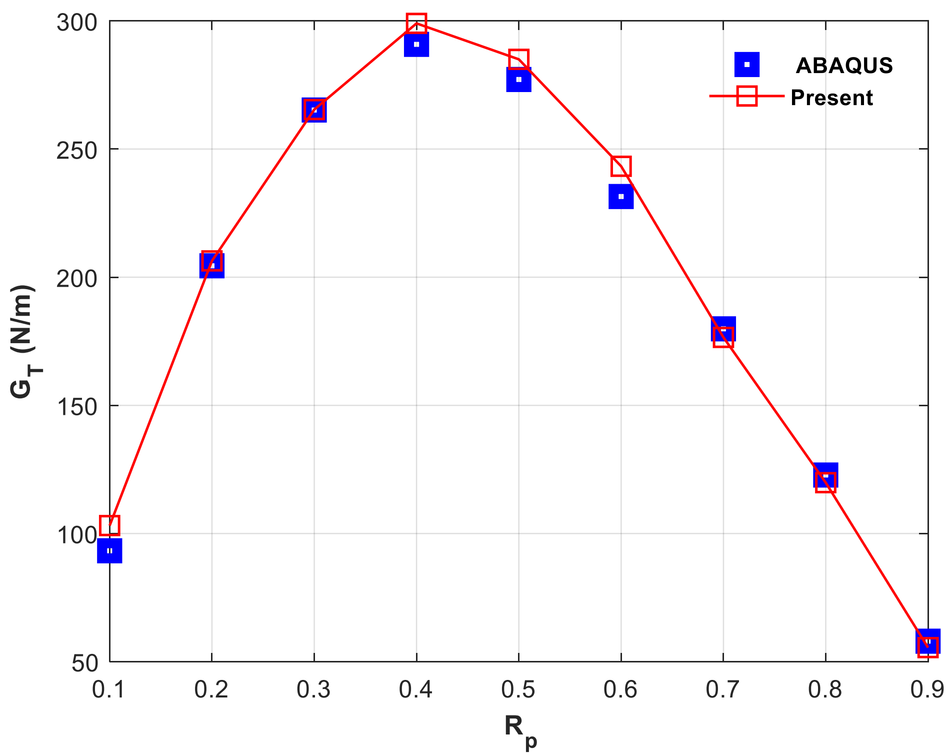

Figure 6-10 G_T comparison between present method and ABAQUS (case 2).

6.4.2. Length Effect

For case 1, the crack radius is 10 mm. A constant moment $M_o = 2\ N - m$ is applied to investigate G_T obtained from present approach and compared with results from FE-analysis implemented by ABAQUS. The configuration of the curved beam, applied moment, crack radial location and total strain ERR from ABAQUS is shown in Table 6-5. The total strain ERR comparison between present method and results obtained from ABAQUS is tabulated in Table 6-6. G_T^p is the total strain ERR obtained from present method, and G_T^{FE} is the total strain ERR using FE analysis implemented by ABAQUS. The comparison is also shown in Figure 6-11Figure

6-9. All the results obtained from present method have excellent agreement with ABAQUS's results especially for small crack.

Table 6-5 Crack length effect parameters and strain ERR results obtained from FE analysis (case 1).

θ^{+}	θ^{-}	R_i	R_o	R_c	M_o	G_I^{FE}	G_{II}^{FE}	$\frac{G_I^{FE}}{G_{II}^{FE}}$	G_T^{FE}
2.70	-2.70	6.4	12.7	10	2000	17.61	0	0.00%	17.61
5.40	-5.40	6.4	12.7	10	2000	37.6	0.46	1.22%	38.06
8.10	-8.10	6.4	12.7	10	2000	56.86	1.51	2.66%	58.37
10.80	-10.80	6.4	12.7	10	2000	74.74	3.55	4.75%	78.29
13.50	-13.50	6.4	12.7	10	2000	89.87	6.8	7.57%	96.67
16.20	-16.20	6.4	12.7	10	2000	101	11.3	11.19%	112.3

Table 6-6 Total strain ERR comparison between present method and ABAQUS (case 1).

θ^{+}	θ^{-}	R_i	R_o	R_c	M_o	G_T^{p}	G_T^{FE}	*% Diff.*
2.70	-2.70	6.4	12.7	10	2000	17.2	17.61	2.33%
5.40	-5.40	6.4	12.7	10	2000	37.4	38.06	1.73%
8.10	-8.10	6.4	12.7	10	2000	60.7	58.37	-3.99%
10.80	-10.80	6.4	12.7	10	2000	82.4	78.29	-5.25%
13.50	-13.50	6.4	12.7	10	2000	99.7	96.67	-3.13%
16.20	-16.20	6.4	12.7	10	2000	110	112.3	2.05%

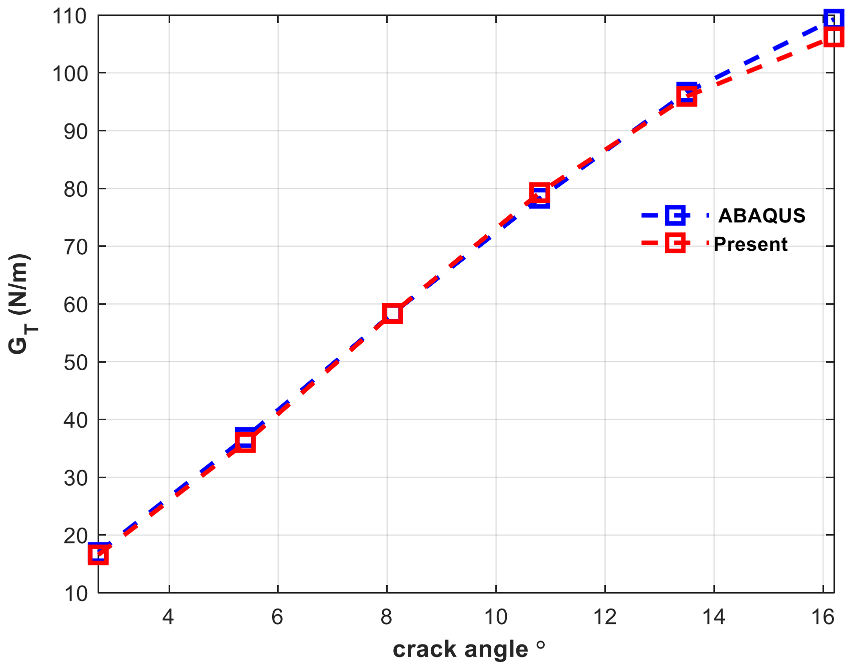

Figure 6-11 G_T length effect comparison between present method and ABAQUS (case 1).

The geometry and applied moment in second case are tabulated in Table 6-7. The comparison between the total strain ERR results obtained from the present method and ABAQUS are tabulated in Table 6-8 and is shown in Figure 6-12. The total strain energy increase as θ increases. The strain ERR for a small crack length is successfully recovered using present method and the error percentage between present method and FE analysis is less than 4 %.

Table 6-7 Crack length effect parameters and strain ERR results obtained from FE analysis (case 2)

θ^{+}	θ^{-}	R_i	R_o	R_c	M_o	G_I^{FE}	G_{II}^{FE}	$\frac{G_I^{FE}}{G_{II}^{FE}}$	G_T^{FE}
2.70	-2.70	12	16	14	1000	9.36	0	0.00%	9.36
5.40	-5.40	12	16	14	1000	27.39	0.185	0.68%	27.575
8.10	-8.10	12	16	14	1000	50.98	0.843	1.65%	51.823
10.80	-10.80	12	16	14	1000	73.19	2.4	3.28%	75.59
13.50	-13.50	12	16	14	1000	93.54	5.61	6.00%	99.15
16.20	-16.20	12	16	14	1000	120.83	10.6	8.77%	131.43

Table 6-8 Total strain ERR comparison between present method and ABAQUS (case 2).

θ^{+}	θ^{-}	R_i	R_o	R_c	M_o	G_T^{p}	G_T^{FE}	*% Diff.*
2.70	-2.70	12	16	14	1000	9.64	9.36	-2.99%
5.40	-5.40	12	16	14	1000	28.6	27.575	-3.72%
8.10	-8.10	12	16	14	1000	52.3	51.823	-0.92%
10.80	-10.80	12	16	14	1000	77.8	75.59	-2.92%
13.50	-13.50	12	16	14	1000	103	99.15	-3.88%
16.20	-16.20	12	16	14	1000	127	131.43	3.37%

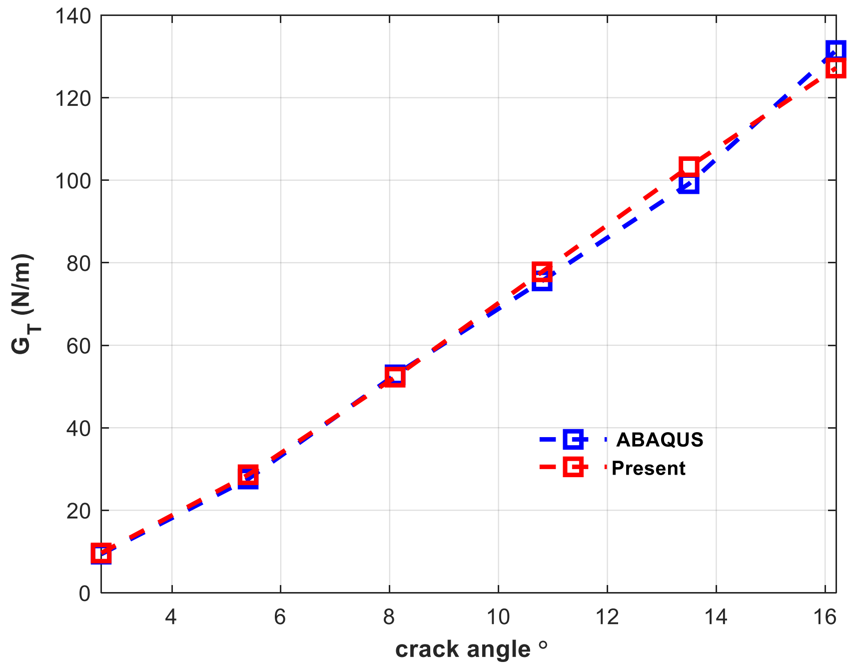

Figure 6-12 G_T length effect comparison between present method and ABAQUS (case 2).

6.4.3. Hoop Effect

Unsymmetrical model is implemented in this section. Table 6-9 and Table 6-10 show the strain energy ERR at the location of crack left tip as shown in Figure 6-5. The radius of the crack is 10 mm, the inner radius is 6.4 mm and the outer radius is 12.7 mm. The length of the crack angle is selected as 5.4° in total or the half crack angle is 2.7°. The unit of the applied moment is N-mm. G_{left} is selected for the analysis only because $G_{\text{left}} > G_{right}$ for a curved beam where the crack locates in the positive θ region. Based on the observation from Table 6-9 and Table 6-10, the failure mode for a small crack is mainly contributed from Mode I. Mode I to Mode II ratio is less than 5 % even the crack locates near $\theta = 45°$. The total strain ERR obtained from present method G_T^p has excellent agreement with results from FE analysis G_T^{FE}. The error percentage is less then 6 % except for a crack which is near $\theta = 45°$.

Table 6-9 The strain ERR for a composite curved beam with a delamination locates in any hoop location under the end bending moment 2000 N-mm.

R_i	R_o	R_c	θ_h	θ_s	θ_e	Moment	$G_{I\ left}^{FE}$	$G_{II\ left}^{FE}$	$G_{T\ left}^{FE}$	G_T^p	% Diff.
6.4	12.7	10	0.00	-2.70	2.70	2000	17.6048	4.13E-02	17.65	17.2	-2.30%
6.4	12.7	10	5.40	2.70	8.10	2000	17.5706	3.91E-02	17.61	17.2	-2.11%
6.4	12.7	10	10.80	8.10	13.50	2000	17.326	3.55E-02	17.36	17.2	-0.73%
6.4	12.7	10	16.20	13.50	18.90	2000	16.7817	2.93E-02	16.81	17.2	2.49%
6.4	12.7	10	21.60	18.90	24.30	2000	15.75	1.93E-02	15.77	15.7	-0.32%
6.4	12.7	10	27.00	24.30	29.70	2000	13.92	6.64E-03	13.93	14.7	5.60%
6.4	12.7	10	32.40	29.70	35.10	2000	10.87	0	10.87	11	1.20%
6.4	12.7	10	37.80	35.10	40.0	2000	6.3	0	6.3	7.87	24.92 %

Table 6-10 The strain ERR for a composite curved beam with a delamination locates in any hoop location under the end bending moment 5000 N-mm.

R_i	R_o	R_c	θ_h	θ_s	θ_e	Moment	$G_{I\ left}^{FE}$	$G_{II\ left}^{FE}$	$G_{T\ left}^{FE}$	G_T^p	% Diff.
6.4	12.7	10	0.00	-2.70	2.70	5000	109.583	0.235	17.65	109.82	1.66%
6.4	12.7	10	5.40	2.70	8.10	5000	109.305	0.2189	17.61	109.52	1.39%
6.4	12.7	10	10.80	8.10	13.50	5000	107.722	0.195	17.36	107.92	-0.08%
6.4	12.7	10	16.20	13.50	18.90	5000	104.257	0.156	16.81	104.41	-3.44%
6.4	12.7	10	21.60	18.90	24.30	5000	97.7	0	15.77	97.70	-0.41%
6.4	12.7	10	27.00	24.30	29.70	5000	86.2	0	13.93	86.20	-6.50%
6.4	12.7	10	32.40	29.70	35.10	5000	66.96	0	10.87	66.96	-2.90%
6.4	12.7	10	37.80	35.10	40.0	5000	38.2	0	38.2	21.99	28.8 %

The failure moment can be computed when $G^{p}_{I\,left} = G^{c}_{I_{left}} = 277\ \mathrm{N/m}$. According to Table 6-11, if the crack locates close to $\theta_h = 45°$, approximately 38 % increment is observed compared with the crack locates near $\theta = 0°$

Table 6-11 Failure moment investigation for a composite curved beam with a half crack angle 2.7°

R_i	R_o	R_c	θ_h	θ_s	θ_e	Moment
6.4	12.7	10	0	-2.7	2.7	10632
6.4	12.7	10	4.05	1.35	6.75	10632
6.4	12.7	10	9.45	6.75	12.15	10632
6.4	12.7	10	14.85	12.15	17.55	10632
6.4	12.7	10	20.25	17.55	22.95	10632
6.4	12.7	10	25.65	22.95	28.35	11932
6.4	12.7	10	29.7	27	32.4	12945
6.4	12.7	10	35.1	32.4	37.8	14685

6-5 Conclusion

The analytical solutions is developed to calculate the total strain ERR for a composite curved beam under bending. Both symmetrical and unsymmetrical models are developed, which means the crack can be located in any interface and hoop location. FE analysis is implemented to verify results obtained from the present approach. In FE analysis, VCCT techniques is implemented to study the strain ERR at the crack tip. For a composite curved beam with a crack locates in any radial location, the strain ERR reaches to maximum at the location where maximum σ_r is observed of a prefect composite curved beam under bending. The strain ERR analytical solutions can be obtained accurately by using linear scale parameters compared with strain ERR results from FE analysis. After introducing scale parameters, the present strain ERR has good agreement with FE analysis result. In addition, strain ERR increases when the total crack length increases. That is, higher moment can be applied on the shorter crack. If the total crack angle increases from 5.4° to 32.4°, the applied moment significantly reduce from 8.356 N-m to 3.287 N-m for a composite curved beam with inner radius is 6.4 mm, outer radius is 12.7 mm, and the crack radius is 10 mm composite curved beam. The effect of crack hoop location is also investigated. If crack locates near $\theta_h = 40°$, the applied moment is 38 % higher than the crack locates at $\theta_h = 0°$. In conclusion, the present successfully aim the void where previous authors couldn't predict accurately for a composite curved beam with a small crack. Moreover, this study allows the crack can be located in any interface and hoop locations, which provides a feasible way to efficiently analyze composite curved beam with a crack and the total strain ERR results can be predicted accurately even when the radius to total thickness ratio is small.

Chapter 7

TORSIONAL AND WARPING STIFFNESS OF COMPOSITE Z-STIFFENERS

7-1 Introduction

Composite materials have been applied in aircraft structure components for its performance efficiency. In applications, thin walled beams of composite structures with an open cross-section, such Z-section are widely used for stiffeners or stringers as load carrying members. Analysis of composite beams has been extensively studied in the past. Several books containing composite beam analysis were published [88-92]. Among these books [88, 89], analysis of the composite beams only employed the properties in the beam axis. Other books [90-92] include the effect due to transverse shear in the beam structural response. Their formulations, though rigorous, were complicated and not handy and efficient enough for practicing engineers to use in their design. In engineering design practice, there is a need of simple closed form expressions for quick but accurate evaluation of sectional properties and ply stresses/strains, which can be easily used for parametric study and optimal design.

In analysis of composite beams, Wu and Sun [93] formulated a general expression of the constitutive equation by using thin-walled shell theory. Both warping and shear deformation of the beam are also included. Yu et al. [94] presented a generalized Vlasov Theory of composite thin-walled structures. In 2012, Yu et al. [95] used the varied asymptotic method to determine the sectional properties of composite beams. Drummond and Chan [96] analytically and experimentally investigated I-beam under bending. Their expression for evaluating bending stiffness included the stiffness due to flanges, web and the spandrels at the intersection corners of flange and web. In the analysis of I-beam under bending and torsion, Jung and Lee [97] included the elastic coupling, shell wall thickness, transverse shear deformation, torsion warping, and constrained warping. Rios and Chan [98] presented a unified analysis of stiffener reinforced composite beams. In their study, a general analytical method was presented for evaluating the structural response of composite laminated beams. For beams with both open- and closed-sections, Parambil et al. [99] and Sanghavi and Chan [100], using structural characteristics of narrow composite beam, developed a closed-form expression for evaluation of bending, torsion and warping stiffness as well as ply stresses/strains for I-beam.

On the other hand, analysis of composite beams is often conducted by using smeared properties of laminate and then employing into conventional structural analysis. In this simplified approach, the sectional properties of composite beams such as bending and torsional stiffness (E_xI and $G_{xy}J$), are obtained by using equivalent axial and shear moduli of the cross-sectional laminate (E_x and G_{xy}) times the moments of inertia, I and J which are purely geometric parameters. In so doing, the stiffness due to effect of un-symmetric layup of laminate is included but the coupling stiffness due to effect of un-symmetric configuration of cross-section is ignored. Syed and Chan [101] found that this conventional approach for evaluating sectional stiffness results in a significant difference from the Finite Element (FE) results.

The main objective of this paper is to present a novel analytical method for conducting stress analysis for Z-sectioned beam which is made of laminated composites. Analytical closed-form expressions for determining the torsional and wrapping stiffness as well as locations of shear center in term of laminate properties were developed based upon a modified lamination theory. The similar approach to this was successfully used for analyzing the ply stresses of composite I-beams under bending and torsion loads [100].

7-2 Constitutive Equation of Isotropic Z-Stiffener

Thin wall structurers are using often in aircraft applications ranged from the single cell closed section fuselage to multi-cellular wings, which are subjected to bending, shear, axial and torsional loads. Several shapes including channel, T -, I -, or Z -sections are used to stiffen the structures by providing supports for internal loads. Thin wall structures contain high load capacity but have relatively small thickness [102]. The twisting rigidity is quite significant so it can be considered with stiffer than a beam of comparable span and thickness. Thin wall structures are classified as open and closed section. For a thin wall section is considered as closed section, the centerline of its walls is a closed curve. For open section, the centerline of its walls is not a closed curve such as I -, T-, and Z – sections.

7.2.1. Torsional Stiffness of Isotropic Z-Stiffener

Figure 7-1 shows the geometry of Z-stiffener. Three family members are considered, which are the top (f_1) and bottom (f_2) laminates, and the web (w). W is the width for the laminate and h is the thickness of the laminate. For St. Venant's Torsion,

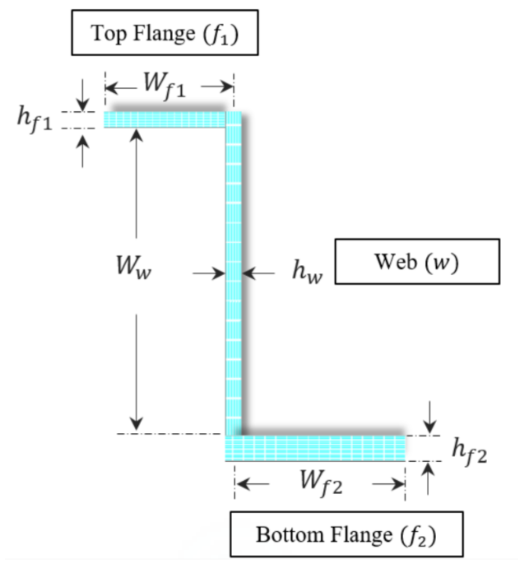

Figure 7-1 Family member and geometry definition of Z-stiffener.

$$T_{sv} = \mathrm{GK}\frac{d\theta_{sv}}{dx} \tag{7-1}$$

where G = shear modulus, θ_{sv}= total angle of twist in free torsion case, and K = torsion constant, so-called polar moment of inertia. For open cross section structures, torsion constant K can be taken as the sum of the torsional constants of each rectangular cross section's K. Three different method are provided in this work. For method 1, 2, and 3, K_1, K_2, [108] and K_3 [103] can be expressed as

$$\mathrm{K}_1 = \frac{W_{f1}h_{f1}^3 + W_w h_w^3 + W_{f2}h_{f2}^3}{3}$$

$$\mathrm{K}_2 = \frac{\mu_{f1}W_{f1}h_{f1}^3 + \mu_w W_w h_w^3 + \mu_{f2}W_{f2}h_{f2}^3}{3} \tag{7-2}$$

$$K_3 = ab^3\left(\frac{1}{3} - 0.21\frac{b}{a}\left(1 - \frac{b^4}{12a^4}\right)\right)$$

where μ is a width reduction factor tabulated in Table 7-1, and a is the length of longer side of the cross-section, b is length of shorter side of the cross-section.

Table 7-1 Width reduction factor [103], where h is the thickness of the beam.

W/h	1.0	1.5	2.0	2.5	3.0	4.0	5.0	6.0	10.0	∞
μ	0.423	0.588	0.687	0.747	0.789	0.843	0.873	0.897	0.936	0.999

For a Z cross-sectional stiffener, the torsional constant can be expressed as

$$K_{total} = K_{f1} + K_{f2} + K_w \tag{7-3}$$

where K_{f1}, K_{f2} *and* K_w are with respect to top flange, bottom flange and web.

7.2.2. Warping Stiffness of Isotropic Beam

A mathematical sectorial based approach is provided by [104] to calculate warping properties. The parameter definition of sectorial area of any 2 random points is shown in Figure 7-2.

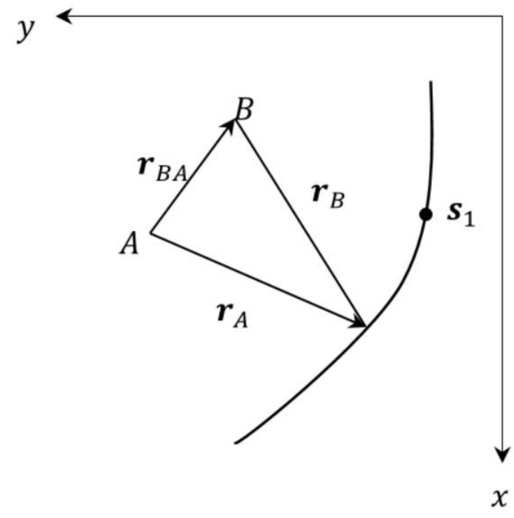

Figure 7-2 Definition of sectorial area [15].

Let A and B be two randomly selected poles from the warping function. Supposed the origin for W_A is selected to be at $S = S_0$ and the origin for W_B at $S = S_1$. The equation for finding the warping function W_A with origin S_0 from the warping function W_B with origin S_1 is

$$\mathrm{W_A}(s) = W_B(s) - W_B(S_0) + (z_A - z_B)(y(s) - y_0)$$
$$-(y_A - y_B)(z(s) - z_0) \tag{7-4}$$

where A and B are coincident point.

If $w(s)$ is a warping function for a particular pole and origin, the area integral

$$\mathrm{Q_w} = \int w(s)dA \tag{7-5}$$

is called the *first sectorial moment*. The area integrals

$$I_{yw} = \int y(s)w(s)dA$$
$$I_{zw} = \int z(s)w(s)dA \tag{7-6}$$

are known as the *sectorial products* of area. Moreover, the definition of the first, second, and product moments of area can be expressed as

$$Q_y = \int zdA$$
$$Q_z = \int ydA$$
$$I_y = \int z^2dA \tag{7-7}$$
$$I_z = \int y^2dA$$
$$I_{yz} = \int yzdA$$

The important concept here is when those sectorial products of area are both equal zero, the pole is called *principal pole*, or *shear center*. By integrating both sides of the results over the cross-section area and multiplying both sides, we can obtain

$$I_{yw_A} = I_{yw_B} - w_B(S_0)Q_Z + (z_A - z_B)(I_z - y_0Q_z) - (y_A - y_B)\left(I_{yz} - z_0Q_z\right) \tag{7-8}$$

Since the origin of the *y*, *z* axis is the centroid C of the cross section, the first moments Q_z and Q_y are both zero. For the conditions for A to be a principal pole

$$I_{yw_A} = I_{zw_A} = 0 \tag{7-9}$$

Therefore,

$$y_A = y_B + \frac{I_{zw_B}I_z - I_{yw_B}I_{yz}}{I_yI_z - I_{yz}^2} \tag{7-10}$$

$$z_A = z_B + \frac{I_{zw_B} I_{yz} - I_{yw_B} I_y}{I_y I_z - I_{yz}^2}$$

If, for a given pole A, there is a sectorial origin s_0 such that

$$Q_{wA} = \int w_A(s)\, dA = 0 \tag{7-11}$$

The point s_0 is termed as a *principal origin*. Let B be a pole coincident with A but with a known origin s_1,

$$w_A(s) = w_B(s) - w_B(s_0) \tag{7-12}$$

Hence, for a given cross section, it is possible to find a pole A and an origin s_0 so that Q_{wA}, I_{yw_A}, and I_{zW_A} are zero.

7.2.3. Warping Stiffness of Isotropic Z-Stiffener

Considering an isotropic beam with Z cross-section as shown in Figure 7-3, the dimensions are:

$$b_1 = W_{f1} - \frac{h_w}{2} \quad b_2 = W_{fw} - \frac{h_w}{2} \quad h = W_w + \frac{h_{f1}}{2} + \frac{h_{f2}}{2} \tag{7-13}$$

The centroid C is at a horizontal distance d and a vertical distance e from the intersection O of the lower flange and the web

$$d = \bar{Y}_c - \frac{h_w}{2} \quad e = \bar{Z}_c - \frac{h_{f2}}{2} \tag{7-14}$$

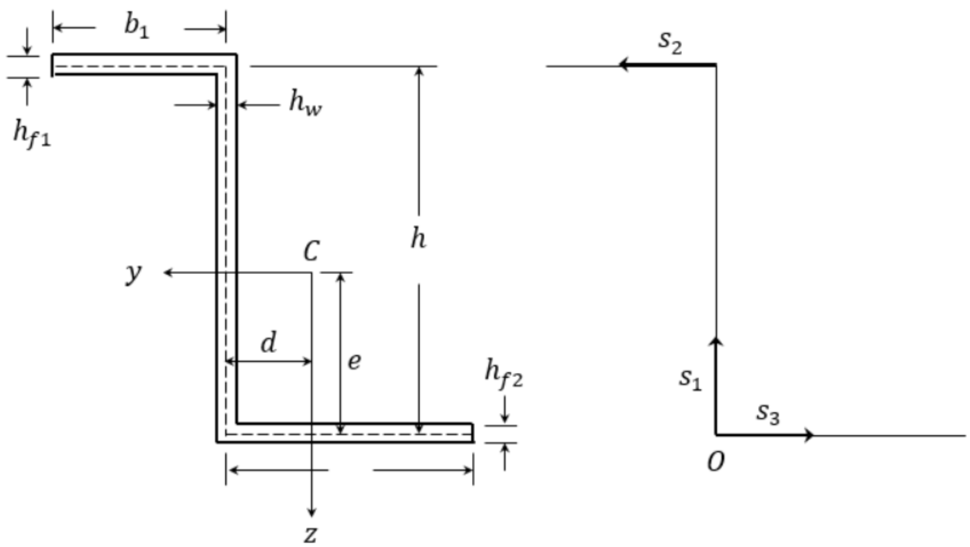

Figure 7-3 Geometry of unsymmetrical Z-section and shear flow direction.

where

$$\bar{Y}_c = \frac{\left(-\frac{W_{f1}}{2} + h_w\right)(W_{f1}h_{f1}) + \left(\frac{h_w}{2}\right)(W_w h_w) + (\frac{W_{f2}}{2})(W_{f2}h_{f2})}{W_{f1}h_{f1} + W_w h_w + W_{f2}h_{f2}}$$

$$\bar{Z}_c = \frac{\left(h_{f2} + W_w + \frac{h_{f1}}{2}\right)(W_{f1}h_{f1}) + \left(\frac{h_w}{2} + h_{f2}\right)(W_w h_w) + (\frac{h_{f2}}{2})(W_{f2}h_{f2})}{W_{f1}h_{f1} + W_w h_w + W_{f2}h_{f2}} \tag{7-15}$$

If the point O is used both as the pole and the sectorial origin the warping function is

$$w_O(s_1) = 0 \quad w_O(s_2) = hs_2 \quad w_O(s_3) = 0 \tag{7-16}$$

To find the principal pole, the values of the sectorial products of area can be calculated.

$$I_{yw_O} = \int yw_O dA\, y = \int_0^{b_1} (d + s_2) w_O(s_2) h_{f1} ds_2$$

$$I_{zw_O} = \int zw_O dA\, y = \int_0^{b_1} (-h + e) w_O(s_2) h_{f1} ds_2 \tag{7-17}$$

The principal pole *A* or *shear center* can be expressed as

$$Y_{so} = y_A = y_O - \frac{I_{zw_B} I_z - I_{yw_B} I_{yz}}{I_y I_z - I_{yz}^2}$$

$$Z_{so} = z_A = z_O - \frac{I_{zw_B} I_{yz} - I_{yw_B} I_y}{I_y I_z - I_{yz}^2} \tag{7-18}$$

The warping function with principal pole *A* and origin *O* is

$$w_A(s_1) = -(y_A - y_O)s_1$$

$$w_A(s_2) = -(y_A - y_O)h + (h - z_A)s_2 \tag{7-19}$$

$$w_A(s_3) = z_A s_3$$

The first sectorial area moment is

$$Q_{wA} = \int_0^{h} w_A(s_1) h_w d_{s1} + \int_0^{b_1} w_A(s_2) h_{f1} d_{s2} + \int_0^{b_2} w_A(s_3) h_{f2} d_{s3} \tag{7-20}$$

The condition for s_0 to be a principal origin is

$$w_A(s_0) = \frac{Q_{wA}}{A} \tag{7-21}$$

where $A = W_{f1} h_{f1} + W_w h_w + W_{f2} h_{f2}$

The principal warping functions

$$w(s_1) = w_A(s_1) - w_A(s_0)$$

$$w(s_2) = w_A(s_2) - w_A(s_0) \quad (7\text{-}22)$$

$$w(s_3) = w_A(s_3) - w_A(s_0)$$

Therefore, the warping constant I_w (or Γ) can be computed as

$$I_w = \int_0^h w(s_1)^2 h_w d_{s1} + \int_0^{b_1} w(s_2)^2 h_{f1} d_{s2} + \int_0^{b_2} w(s_3)^2 h_{f2} d_{s3} = \Gamma \quad (7\text{-}23)$$

The torque due to warping is

$$\mathrm{T_w} = -E\Gamma \frac{d^3\theta}{dx^3} \quad (7\text{-}24)$$

where E = Axial stiffness, Γ = Warping constant, EΓ = Warping stiffness.

The total torque will be resisted by St Venant's shearing stresses and warping torsion. The derivation is well documented in [100].

$$\mathrm{T} = \mathrm{T_{sv}} + T_w = GK\frac{d\theta}{dx} - E\Gamma\frac{d^3\theta}{dx^3} \quad (7\text{-}25)$$

Rearranging and writing $\mu^2 = \frac{GK}{E\Gamma}$ to solve $\frac{d\theta}{dx}$, we have

$$\frac{d^3\theta}{dx^3} - \mu^2\frac{d\theta}{dx} = -\mu^2\frac{T}{GK} \quad (7\text{-}26)$$

Applying boundary conditions with

1. When x = 0, the slope of beam equals zero.
2. When x = L, the bending moment is zero.

$$\frac{d\theta}{dx} = \frac{T}{GK}\left(1 - \frac{\cosh \mu(L-x)}{\cosh \mu L}\right) \tag{7-27}$$

Thus, θ can be solved.

$$\theta_{warp} = \frac{T}{GK}\left(x + \frac{\sinh \mu(L-x)}{\mu \cosh \mu L} - \frac{\sinh \mu L}{\mu \cosh \mu L}\right) \tag{7-28}$$

When x = L,

$$\theta_{warp} = \frac{TL}{GK}\left(1 - \frac{\tanh \mu L}{\mu L}\right) \tag{7-29}$$

Considering only free torsion case,

$$\theta_{sv} = \frac{TL}{GK} \tag{7-30}$$

7-3 Constitutive Equation of Composite Z-Stiffener

7-3.1 Constitutive Equation of Laminated Composite Beam under Torsion

The foundation of beam analysis is based upon the one-dimensional moment-curvature relationship along the longitudinal axis of the beam under bending and upon the torque-twist angle relationship along the center axis of twist of the cross-section for torsion. This approach for laminated composite beams is similar with the approach used in isotropic beams. However, evaluation of the sectional properties is different. These properties are not only dependent of the geometry of the cross-section but also composite material properties and their stacking sequence. Composite material is inherent with two-dimensional property. Hence, an equivalent one-dimensional property of composite beam is needed. The equivalent one-dimensional property is dependent of the structural response of the deformed beam and the structural response of the beam is dependent on the ratio of the width to height of the beam cross-section. Beam with general, wide, and narrow sections under axial and bending are discussed in Chapter 4-2. The axial and bending stiffness under general, wide, and narrow sections are shown in Eqs. (4-7), (4-9), and (4-15).

For the case of torsion, no axial strains, ε_x^0 and ε_y^0 as well as K_x exist. However, a non-zero M_x is induced for the laminate under torsion. The narrow laminate constitutive equation subjected to torsion is given as

$$\begin{bmatrix} N_{xy} \\ M_{xy} \end{bmatrix} = \begin{bmatrix} A_T^* & B_T^* \\ B_T^* & D_T^* \end{bmatrix} \begin{bmatrix} \gamma_{xy}^0 \\ \kappa_{xy} \end{bmatrix} \ and \ \begin{bmatrix} A_T^* & B_T^* \\ B_T^* & D_T^* \end{bmatrix} = \begin{bmatrix} a_T^* & b_T^* \\ b_T^* & d_T^* \end{bmatrix}^{-1} \qquad (7\text{-}31)$$

where

$$a_T^* = \left(a_{66} - \frac{{b_{61}}^2}{d_{11}}\right);\, b_T^* = \left(b_{66} - \frac{b_{61} d_{16}}{d_{11}}\right);\ d_T^* = \left(d_{66} - \frac{{d_{16}}^2}{d_{11}}\right) \qquad (7\text{-}32)$$

It should be noted that the properties with a subscript, $_T$ refer to laminate under torsion. In general, b_{61} and b_{16} are not the same. The shear center, Z_{sc} measuring from the mid-plane of the laminate can be obtained by setting shear strain with absence of N_{xy}.

$$z_{sc} = -\frac{\gamma_{xy}^0}{\kappa_{xy}} = -\frac{b_T^*}{d_T^*} \qquad (7\text{-}33)$$

The torsional stiffness of the laminate at the shear center, Z_{sc} can be obtained by using the parallel theorem as

$$D_{T_{sc}}^* = D_T^* - 2 z_{sc} B_T^* + z_{sc}^2 A_T^* \qquad (7\text{-}34)$$

Like beam of isotropic material, an edge correction factor is needed to accommodate the zero shear boundary condition. The torsional stiffness, GK is modified by a correction factor, μ as shown below:

$$GK = 4b\, \mu\, D^{*}_{T_{sc}} \tag{7-35}$$

In this analysis, the correction factor used for isotropic material as listed in [105] is adopted. For a finite rectangular cross-section of the beam, the twist curvature is twice of the rate of the twisting angle, ϕ and the torque, T is twice of total twisting moment of the laminate, b*M_{xy} where b is the width of laminate.

$$\phi = \frac{T}{4b\, D^{*}_{T_{sc}}} \tag{7-36}$$

7-3.2 Shear Center

The shear center for composite beam depends on the geometry of the cross-section, material properties, and the stack sequence. It is an important sectional property because the bending and torsion are uncoupled at the shear center. Twisting will be induced if only torque is applied and vice versa. The axial and bending stiffness for composite Z-stiffener are provided [106, 107] as shown below

$$\bar{A}_x = [w_{f1}(A^{*}_{1,f1}) + w_{f2}(A^{*}_{1,f2}) + w_w(A^{*}_{w})] \tag{7-37}$$

$$\overline{D}_z = \left\{ \left[A^*_{1,f1} \left[y^2_{c,f1}\, w_{f1} + \left(\frac{w^3_{f1}}{12} \right) \right] \right] \right.$$

$$+ \left[A^*_{1,f2} \left[y^2_{c,f2}\, w_{f2} + \left(\frac{w^3_{f2}}{12} \right) \right] \right]$$

$$\left. + \left[D^*_w\, w_w + A^*_w\, y^2_{c,w}\, w_w + 2\, B^*_w\, y_{c,w}\, w_w \right] \right\}$$

$$\overline{D}_{yz} = \{ (A^*_{1,f1} w_{f1}\, y_{c,f1}\, z_{c,f1} + B^*_{1,f1}\, w_{f1}\, y_{c,f1})$$

$$+ (A^*_{1,f2}\, w_{f2}\, y_{c,f2}\, z_{c,f2} + B^*_{1,f2}\, w_{f2}\, y_{c,f2})$$

$$+ (B^*_w\, w_w\, z_{c,w} + A^*_w\, w_w\, z_{c,w}\, y_{c,w}) \}$$

$$\overline{D}_y = \left[w_{f1}\, D^*_{1,f1} + w_{f1}\, A^*_{1,f1}\, z^2_{c,f1} + 2\, w_{f1}\, B^*_{1,f1}\, z_{c,f1} + w_{f2}\, D^*_{1,f2} \right.$$

$$+ w_{f2}\, A^*_{1,f2}\, z^2_{c,f2} + 2\, w_{f2}\, B^*_{1,f2}\, z_{c,f2}$$

$$\left. + A^*_{1,w} \left[z^2_{c,w}\, w_w + \left(\frac{w^3_w}{12} \right) \right] \right]$$

Curvatures for a composite Z-stiffener under bending can be expressed as

$$K_y = \frac{\overline{D}_y}{\overline{D}_y \overline{D}_z - \overline{D}^2_{yz}} \quad K_z = \frac{\overline{D}_z}{\overline{D}_y \overline{D}_z - \overline{D}^2_{yz}} \quad K_{yz} = \frac{\overline{D}_{yz}}{\overline{D}_y \overline{D}_z - \overline{D}^2_{yz}} \qquad (7\text{-}38)$$

Curvature at centroid can be written as

$$K^c_y = \overline{M}_y K_z - \overline{M}_z K_{yz} \quad K^c_z = \overline{M}_z K_y - \overline{M}_z K_{yz} \qquad (7\text{-}39)$$

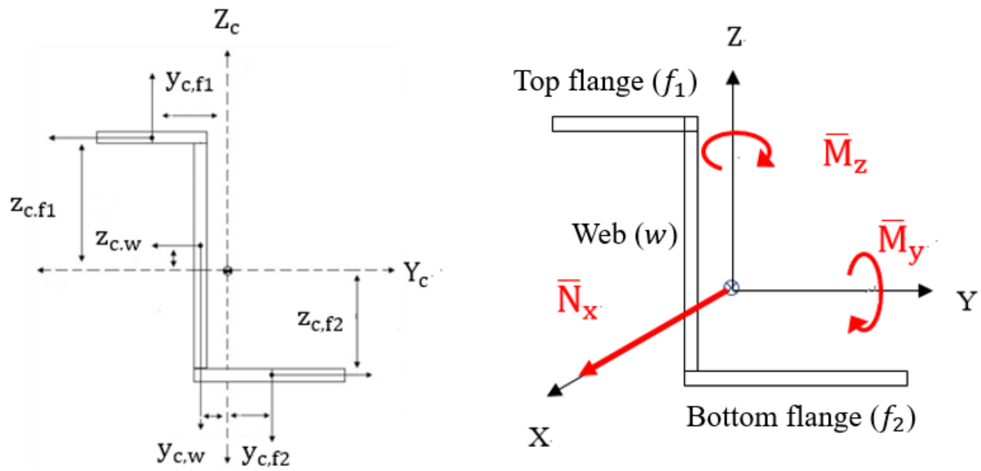

Figure 7-4 Geometry of composite Z-stiffener and load components.

Distances from top flange, lower flange and web to the origin and loading schematic is shown in Figure 7-4. Strain of the top flange can be expressed as

$$\varepsilon_{x_{f1}}^{0} = \varepsilon_x^0 + yK_z^c + zK_y^c \tag{7-40}$$

where

$$\varepsilon_x^0 = \frac{\overline{N_x}}{\bar{A}_x} \tag{7-41}$$

Relationship between applied moment/force and induced shearing force along y and z-direction can be expressed as

$$\frac{\partial N_x}{\partial x} = 0 \quad \frac{\partial \overline{M}_z}{\partial x} = V_y \quad \frac{\partial \overline{M}_y}{\partial x} = V_z \tag{7-42}$$

Substituting Eqs. (7-41) into (7-42), the following equation can be obtained.

$$\frac{\partial N_{x_{f1}}}{\partial x} = A_{1_{f1}}^{*}\left[y\left(V_y K_y - V_z K_{yz}\right) - z\left(V_z K_z - V_y K_{yz}\right)\right] \tag{7-43}$$

If there is no load applied in the axial direction, the equilibrium equation can be expressed as

$$\frac{\partial q}{\partial s} + \frac{\partial N_x}{\partial x} = 0 \tag{7-44}$$

where q = Shear flow, s = The flow direction, N_x = Total force in x-direction (lb/in).

Rearranging Eqs. (7-44), we can obtained:

$$\frac{\partial q_{f1}}{\partial s_1} = -\frac{\partial N_{x f1}}{\partial x} = -A_{1\,f1}^{\ *}\left[y\left(V_y K_y - V_z K_{yz}\right) - z\left(V_z K_z - V_y K_{yz}\right)\right] \tag{7-45}$$

The shear flow on the top flange after integration can be written as

$$q_{f1} = \int_0^{s_1} -A_{1\,f1}^{\ *}\left[y\left(V_y K_y - V_z K_{yz}\right) - z\left(V_z K_z - V_y K_{yz}\right)\right] ds_1 \tag{7-46}$$

Due to unsymmetrical cross-section, both shear force V_y and V_z has necessary to be applied. The shear flow on top flange due to V_y and V_z applied at the shear center are

$$\begin{gathered} q_{f1_y} = -(V_y K_y) \int_0^{s_1} A_{1\,f1}^{\ *}\, y ds_1 - \left(-V_y K_{yz}\right) \int_0^{s_1} A_{1_{f1}}^{*}\, z ds_1 \\ q_{f1_z} = -(V_z K_{yz}) \int_0^{s_1} A_{1\,f1}^{\ *}\, y ds_1 - (V_z K_z) \int_0^{s_1} A_{1_{f1}}^{*}\, z ds_1 \end{gathered} \tag{7-47}$$

where $y = -W_{f1} + h_w - \bar{Z}_c + s_1$ and $z = z_{c_{f1}}$.

The shear forces acting on the top flange are introduced as

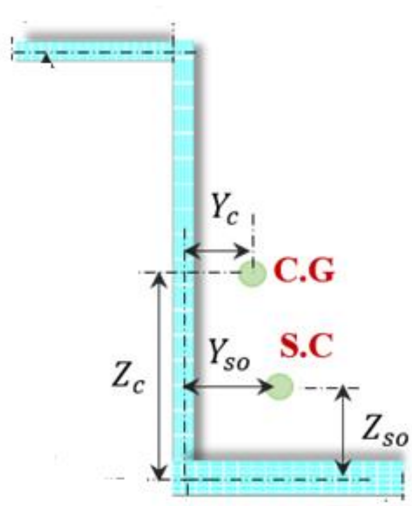

Figure 7-5 Definition of distances regarding with the shear center.

$$V_{f1_y} = \int_0^{W_{f1}-\frac{h_w}{2}} q_{f1_y} ds_1$$
$$V_{f1_z} = \int_0^{W_{f1}-\frac{h_w}{2}} q_{f1_z} ds_1 \tag{7-48}$$

The distances from centroid to shear center can be expressed as

$$\mathrm{Z_{sc}} = V_{f1_y} \frac{\left(\frac{h_{f2}}{2} + W_w + \frac{h_{f1}}{2}\right)}{V_y} - \bar{Z}_c$$
$$\mathrm{Y_{sc}} = V_{f1_z} \frac{\left(\frac{h_{f2}}{2} + W_w + \frac{h_{f1}}{2}\right)}{V_z} - \bar{Y}_c \tag{7-49}$$

Distance between the middle line intersection between web and bottom and the shear center can be expressed as

$$\mathrm{Z_{so}} = Z_{sc} + \bar{Z}_c$$
$$\mathrm{Y_{so}} = Y_{sc} + \bar{Y}_c \tag{7-50}$$

7-3.3 Torsional Stiffness of Composite Z-Stiffener

Based on CLT, the relationship for a thin rectangular cross-section can be shown as

$$\begin{bmatrix} \varepsilon_x^0 \\ \varepsilon_y^0 \\ \gamma_{xy}^0 \\ k_x \\ k_y \\ k_{xy} \end{bmatrix} = \begin{bmatrix} a_{11} & a_{12} & a_{16} & b_{11} & b_{12} & b_{16} \\ a_{12} & a_{22} & a_{26} & b_{21} & b_{22} & b_{26} \\ a_{16} & a_{26} & a_{66} & b_{61} & b_{62} & b_{66} \\ b_{11} & b_{21} & b_{61} & d_{11} & d_{12} & d_{16} \\ b_{12} & b_{22} & b_{62} & d_{12} & d_{22} & d_{26} \\ b_{16} & b_{26} & b_{66} & d_{16} & d_{26} & d_{66} \end{bmatrix} \begin{bmatrix} N_x \\ N_y \\ N_{xy} \\ M_x \\ M_y \\ M_{xy} \end{bmatrix} \tag{7-51}$$

At *shear center*, bending and twisting are decoupled. On the other hand, for *torsional center* or we called *center of twist*, it does not move when the member twist. That is, twisting and shearing are decoupled at torsional center. However, if beam subjects only to torsion, it is surprise that the center of twist is identical as shear center. That is, the bending-torsion-shear are decoupled. Thus, for a thin rectangular composite section under a torque, Eqs. (7-51) will be reduced to

$$\begin{bmatrix} \gamma_{xy}^0 \\ k_x \\ k_{xy} \end{bmatrix} = \begin{bmatrix} a_{66} & b_{61} & b_{66} \\ b_{61} & d_{11} & d_{16} \\ b_{66} & d_{16} & d_{66} \end{bmatrix} \begin{bmatrix} N_{xy} \\ M_x \\ M_{xy} \end{bmatrix} \tag{7-52}$$

If pure torque subjected to the shear center is considered, the curvature in x-direction is equal to zero.

$$k_x = b_{61} N_{xy} + d_{11} M_x + d_{16} M_{xy} = 0 \tag{7-53}$$

Solving for Eqs. (7-52),

$$M_x = -\left(\frac{b_{61}}{d_{11}} N_{xy} + \frac{d_{16}}{d_{11}} M_{xy}\right) \tag{7-54}$$

Substituting Eqs. (7-54) to (7-52), the mid-plane shear strain and curvature are obtained.

$$\begin{aligned} \gamma_{\mathrm{xy}}^0 &= \left(a_{66} - \frac{b_{61}^2}{d_{11}}\right) N_{xy} + \left(b_{66} - \frac{b_{61} d_{16}}{d_{11}}\right) M_{xy} \\ k_{xy} &= \left(b_{66} - \frac{b_{61} d_{16}}{d_{11}}\right) N_{xy} + \left(d_{66} - \frac{d_{16}^2}{d_{11}}\right) M_{xy} \end{aligned} \tag{7-55}$$

The constitutive equation for a beam under pure torsion can be expressed as

$$\begin{bmatrix} \gamma_{xy}^0 \\ k_{xy} \end{bmatrix} = \begin{bmatrix} a_T^* & b_T^* \\ b_T^* & d_T^* \end{bmatrix} \begin{bmatrix} N_{xy} \\ M_{xy} \end{bmatrix} \tag{7-56}$$

where

$$a_T^* = \left(a_{66} - \frac{b_{61}^2}{d_{11}}\right) \quad b_T^* = \left(b_{66} - \frac{b_{61} d_{16}}{d_{11}}\right) \quad d_T^* = \left(d_{66} - \frac{d_{16}^2}{d_{11}}\right) \tag{7-57}$$

Under pure torsion assumption, the mid-plane shear strain can curvature are simplified as

$$\begin{aligned} \gamma_{\mathrm{xy}}^0 &= b_T^* M_{xy} \\ \mathrm{k_{xy}} &= d_T^* M_{xy} \end{aligned} \tag{7-58}$$

It should be noted that the shear strain at the shear center is equal to zero.

$$\gamma_{\mathrm{xy}} = 0 = \gamma_{xy}^0 + \rho_{sc} k_{xy} \tag{7-59}$$

Solving for Eqs. (7-59),

$$\rho_{sc} = -\frac{\gamma_{xy}^0}{k_{xy}} = -\frac{b_T^*}{d_T^*} \tag{7-60}$$

The effective stiffness are

$$\begin{bmatrix} A_T^* & B_T^* \\ B_T^* & D_T^* \end{bmatrix} = \begin{bmatrix} a_T^* & b_T^* \\ b_T^* & d_T^* \end{bmatrix}^{-1} \tag{7-61}$$

Stiffness should all shift to the location of center of twist by a distance ρ_{sc}

$$\begin{gathered} \mathrm{A_T}{}_{sc}^{*} = A_T^* \\ \mathrm{B_T}{}_{sc}^{*} = B_T^* - \rho_{sc} A_T^* \\ \mathrm{D}^*_{\mathrm{T_{sc}}} = D_T^* - 2\rho_{sc} B_T^* + \rho_{sc}^2 A_T^* \end{gathered} \tag{7-62}$$

Due to twisting and bending decoupled at the shear center, $\mathrm{B}_{\mathrm{T}^*_{\mathrm{sc}}} = 0$. Definition for curvature and moment in x-y direction can be written as

$$\begin{gathered} k_{xy} = -2\frac{\partial^2 w}{\partial x \partial y} = -2\frac{\partial \frac{\partial w}{\partial y}}{\partial x} = -2\frac{\partial \theta_T}{\partial x} = -2\phi_T \\ \mathrm{M_{xy}} = -\frac{T}{2b} \end{gathered} \tag{7-63}$$

where ϕ_T = rate of twist = $\frac{\partial \theta_T}{\partial x}$, T is the applied torque and b is the width of the laminate. Substituting Eqs. (7-63) to (7-62), the rate of twist is

$$\phi_T = \frac{T}{4bD_{T_{sc}}^*} \tag{7-64}$$

Therefore, for a rectangular cross-section, the torsion stiffness is

$$GK = 4bD_{T^*_{sc}} \tag{7-65}$$

The torsion stiffness for a composite rectangular cross-section depends on material properties, stack sequence, and ply orientation of the laminate. Considering Z-section geometry, since it belongs open thin wall sections, the torsion stiffness can be approximated added together, which is similar to isotropic cases. Three different method discussed in [108] are implemented in order to compute overall torsional stiffness for a composite Z-stiffener as shown below.

$$
\begin{aligned}
GK_1 &= GK_{f1} + GK_{f2} + GK_w = 4w_{f1}D_{T_{sc^*_{f1}}} + 4w_{f2}D_{T_{sc^*_{f2}}} + 4w_wD_{T_{sc^*_w}} \\
GK_2 &= GK_{f1} + GK_{f2} + GK_w = \frac{4w_{f1}}{d_{66_{f1}}} + \frac{4w_{f2}}{d_{66_{f2}}} + \frac{4w_w}{d_{66_w}} \\
GK_3 &= GK_{f1} + GK_{f2} + GK_w = \mu_{f1}4w_{f1}D_{T_{sc^*_{f1}}} + \mu_{f2}4w_{f2}D_{T_{sc^*_{f2}}} + \mu_w4w_wD_{T_{sc^*_w}}
\end{aligned}
\tag{7-66}
$$

where GK_{f1} = Torsion stiffness of top flange. GK_{f2} = Torsion stiffness of bottom flange. GK_w = Torsion stiffness of web.

7-3.4 Warping Stiffness of Composite Z-Stiffener

The warping stiffness of an isotropic beam is function of modulus E and thickness h [109]. The Eh is related to the axial force (per unit length) inside the wall can be shown as follow,

$$N_{\mathrm{x}} = h\sigma_x = Eh\varepsilon^0_{\mathrm{x}} \tag{7-67}$$

For a beam with orthotropic layup,

$$N_x = \frac{d_{11}}{D}\varepsilon_x^0 - \frac{b_{11}}{D}K_z \tag{7-68}$$

where

$$D = a_{11}d_{11} - b_{11}^2 \tag{7-69}$$

At the neutral plane $b_{11} = 0$. Eqs. (7-68) can be simplified to

$$N_x = \frac{1}{a_{11_i}}\varepsilon_x^0 \tag{7-70}$$

where i = top flange, bottom flange, and web.

By comparing with warping stiffness for isotropic and composite I-beam, an orthotropic beam's tension stiffness $\frac{1}{a_{11}}$ corresponds to an isotropic beam's tensile stiffness Eh. For an open arbitrary cross section, we can use criteria to evaluate the warping stiffness of an orthotropic Z-beam by replacing Eh by $1/a_{11_i}$ Thus, the warping stiffness of a composite Z-beam can be expressed as

$$\begin{aligned} EI_w = \left(\frac{1}{a_{11_w}}\right)\int_0^{W_w+\frac{h_{f1}}{2}+\frac{h_{f2}}{2}} w(s_1)^2 ds_1 + \left(\frac{1}{a_{11_{f1}}}\right)\int_0^{W_{f1}-\frac{h_w}{2}} w(s_2)^2 ds_2 \\ + \left(\frac{1}{a_{11_{f2}}}\right)\int_0^{W_{f2}-\frac{h_w}{2}} w(s_3)^2 ds_3 \end{aligned} \tag{7-71}$$

7-4 Finite Element Analysis for Composite Z-Stiffener

7-4.1 Model Definition and Boundary Condition

ANSYS APDL version 17.2 [110] is used to model and solve in this study. The composite Z-section beam is considered as three rectangular cross-sections assemble together. The material used for the composite laminate is AS4/3501-6. The shell 281element is selected to preform torsion analysis. In this model, validations can be constructed by switching the material properties from orthotropic to isotropic material properties. The global coordinate system is used for top and bottom flanges, where x-axis represents the length of the flanges, and y-axis represents the width of the flanges. However, for the web, a local co-ordinate system is considered by rotating the $-90°$ with respect to global x-axis. Therefore, for the local co-ordinate system in the web, x-axis will be the length of the web, and y-axis will be the height of the web. The accuracy of the results depends on the way we meshed. A fine mesh is used in this study.

For the case of constrained torsion, cantilever boundary condition is considered in one end surface and the total torsional moment of 1 lb-in^2 is applied on the other end surface. The torsional moment is equally distributed to all of the nodes on the cross-section of the beam, which are called as slave nodes. A master node is named at its shear center at the free end. The force applied to the slave nodes is proportional to the weighting factor, which is related to the distance between the master node and the slave node as shown in Figure 7-6. For the case of free torsion (unconstrained torsion), all degrees of freedoms are constrained at shear center of the cross-section at middle length of the beam. The master node and the slave nodes for this case are referred to the nodes on the cross-section of at middle length of the beam as shown in Figure 7-7.

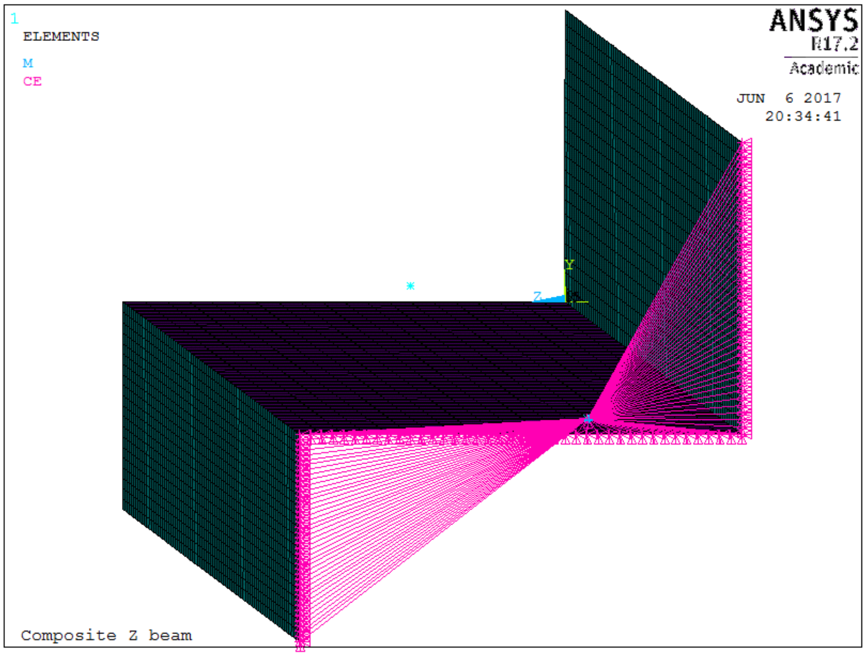

Figure 7-6 Nodes at the end cross-section connected/coupled to the shear center.

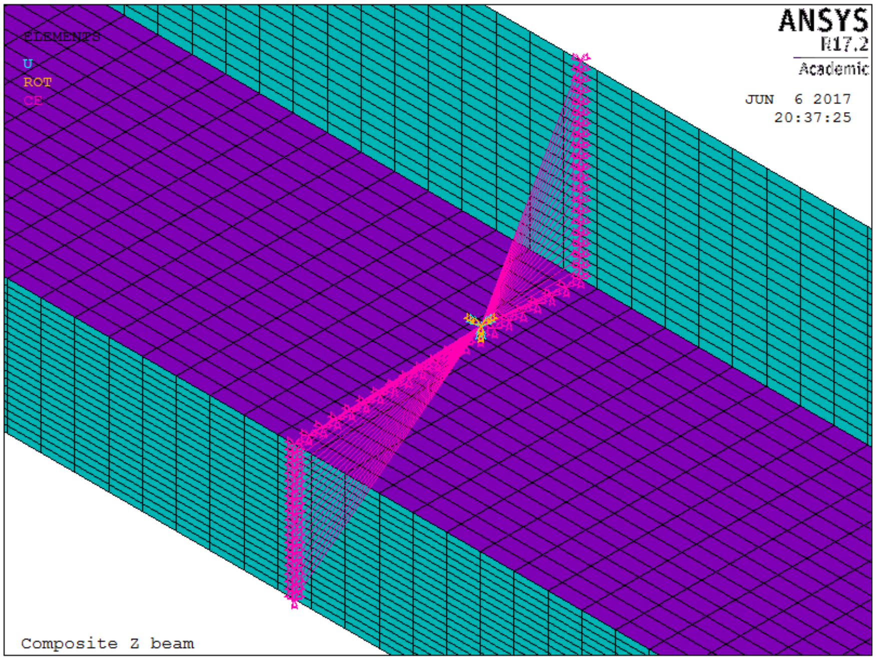

Figure 7-7 Nodes at the middle length of beam cross-section connected/coupled to the shear center.

7-4.2 Torsional and Warping Stiffness in Finite Element Analysis

The validation is performed by using isotropic material properties for composite Z-stiffener. The torsional constant, warping constant can be obtained from ANSYS Beam Tool. If free torsion condition is considered, θ_{sv} is applied at one end surface of the beam and $-\theta_{sv}$ is applied at the other end surface of the beam. Thus, the total amount of M_{xy} can be accumulated which are identical the applied torsion. The torsional stiffness can be obtained using Eqs. (7-30). In order to evaluate warping stiffness, a constant θ_{warp} from theoretical equation is applied. The total amount of M_{xy} is obtained. By using Eqs. (7-29), warping stiffness is obtained.

7-5 Results and Discussion

7-5.1 Isotropic Validation

FE analysis is conducted to verify torsional stiffness in Eqs. (7-1) by selecting a proper reduction factor K_{total_1}, K_{total_2}, and K_{total_3}, where K_{total_i} is the total torsional constant obtained using method i, $i = 1, 2$, and 3. Isotropic material properties are used and three different cross-section geometry are implemented. Case I is a symmetrical Z-stiffener where the length of top and bottom flanges are identical. Case II and case III are unsymmetrical Z-stiffeners with and without identical flanges thickness, respectively, as shown in Table 7-2. The results are tabulated in Table 7-3.

Table 7-2 Selected isotropic cases with different dimensions

Table Dimensions (inches)	Case I	Case II	Case III	Material Properties
Width of top flange	0.5	0.5	0.5	$E = 1.02 \times 10^7\ psi$ $G = 3.7 \times 10^6\ psi$ $v = 0.3$
Width of bottom flange	0.5	0.7	0.7	
Height of web	1	1	1	
Thickness of top flange	0.04	0.04	0.05	
Thickness of bottom flange	0.04	0.04	0.04	
Thickness of web	0.02	0.02	0.02	

Table 7-3 Torsional stiffness comparison for isotropic Z-stiffener

Case	**Torsional Stiffness GK (unit: $\mathrm{lb-in^2}$)**			
	Analytical Approach			ANSYS Beam Tool
	Method 1	Method 2	Method 3	
I	87.22	84.67	84.70	86.95
II	103.01	100.67	100.48	102.86
III	139.87	135.87	135.23	138.75

Based on the observation in Table 7-3, the torsional stiffness results obtained from Method 2 and 3 are quit comparable. Comparison between ANSYS Beam Tool and present analytical results for the centroid and shear center is shown in Table 7-4. The centroid is measured from the origin located at the intersection between base line of bottom flange and the most left line of the web. The shear center is measured from the origin located at the intersection between middle line of bottom flange and the middle line of the web.

Table 7-4 Comparison between analytical and ANSYS Beam Tool for shear center and centroid, respectively

	Centroid				**Shear Center**			
Geometry	ANSYS Beam Tool		Analytical		ANSYS Beam Tool		Analytical	
(inches)	$\mathrm{Y_{co}}$	Z_{co}	$\mathrm{Y_{co}}$	Z_{co}	$\mathrm{Y_{So}}$	Z_{So}	$\mathrm{Y_{So}}$	Z_{So}
Case I	0.00	0.55	0.00	0.52	0.00	0.52	0.00	0.52
Case II	0.069	0.458	0.019	0.458	0.0725	0.260	0.0726	0.259
Case III	0.0482	0.5003	0.0482	0.5003	0.0625	0.2995	0.0630	0.2990

Table 7-5 Comparison of torsional properties and angle of twist of isotropic Z-Beam with ANSYS results for Case I.

Case 1: Isotropic Material				
	ANSYS Beam Tool	Analytical	ANSYS Z-Beam Model	Difference % (Analytical and ANSYS Z-Model)
$\mathrm{K}\ (\mathrm{in}^4)$ Torsional Constant	2.35×10^{-5}	2.289×10^{-5}	2.251×10^{-5}	1.6 %
$\Gamma\ (\mathrm{in}^4)$ Warping Constant	4.32×10^{-4}	4.326×10^{-4}	4.181×10^{-4}	3.4 %
$\mathrm{GK}\ (psi - in^4)$ Torsional Rigidity	86.95	84.67	83.29	1.6 %
$\mathrm{E\Gamma}\ (\mathrm{psi} - \mathrm{in}^4)$ Warping Rigidity	4406	4413	4265	3.4 %
$\theta_{\mathrm{sv}}\ (rad)$	-	0.1181	0.1181	0 %
$\theta_{\mathrm{warp}}\ (rad)$	-	0.0429	0.0429	0 %

Table 7-6 Comparison of torsional properties and angle of twist of isotropic Z-Beam with ANSYS results for Case II.

Case II: Isotropic Material				
	ANSYS Beam Tool	Analytical	ANSYS Z-Beam Model	Difference % (Analytical and ANSYS Model)
K (in^4) Torsional Constant	2.78×10^{-5}	2.715×10^{-5}	2.677×10^{-5}	1.4 %
Γ (in^4) Warping Constant	6.06×10^{-4}	6.059×10^{-4}	5.799×10^{-4}	4.3 %
GK $(psi - in^4)$ Torsional Rigidity	102.86	100.47	99.04	1.4 %
$E\Gamma$ $(\mathrm{psi} - \mathrm{in}^4)$ Warping Rigidity	6181	6180	5915	4.3 %
θ_{sv} (rad)	-	0.09954	0.09954	0 %
θ_{warp} (rad)	-	0.03278	0.03278	0 %

Table 7-7 Comparison of torsional properties and angle of twist of isotropic Z-Beam with ANSYS results for Case III.

Case III: Isotropic Material				
	ANSYS Beam Tool	Analytical	ANSYS Z-Beam Model	Difference % (Analytical and ANSYS Model)
K (in^4) Torsional Constant	3.75×10^{-5}	3.65×10^{-5}	3.59×10^{-5}	1.7 %
Γ (in^4) Warping Constant	6.84×10^{-4}	6.83×10^{-4}	6.51×10^{-4}	4.8 %
GK ($psi - in^4$) Torsional Rigidity	138.75	135.17	132.93	1.7 %
EΓ ($\mathrm{psi} - \mathrm{in}^4$) Warping Rigidity	6976	6975	6634	4.8 %
θ_{sv} (rad)	-	0.07398	0.07398	0 %
θ_{warp} (rad)	-	0.02702	0.02702	0 %

According to Table 7-4, both results from ANSYS Beam Tool and analytical have excellent agreements. For the case the width of bottom flange is greater than the length of top flange, we observed that the shear center is lower than the centroid for isotropic Z-beam. An overall comparison between ANSYS Beam Tool, Analytical, and ANSYS Z-Stiffener Model is shown in Table 7-5, Table 7-6, and Table 7-7 for Case I, II, and III, respectively.

7-5.2 Composite Validation

Three different cases are selected to verify shear center results. Unidirectional laminate 0° laminate are designed for top flange, bottom flange, and web, respectively. Case I has symmetrical cross-section which the length of top flange and the length of bottom flange are identical. Case II and II has unsymmetrical cross-section. The thickness of the web contains 4 plies for all cases. The dimensions of Z-cross-section are tabulated in Table 7-8.

Table 7-8 Dimensions for selected cases.

Table Dimensions (inches)	Case I	Case II	Case III	Material Properties
Width of top flange	0.5	0.5	0.5	$\mathrm{E} = 1.02 \times 10^7\ psi$ $\mathrm{G} = 3.7 \times 10^6\ psi$ $v = 0.3$
Width of bottom flange	0.5	0.7	0.7	
Height of web	1	1	1	
Thickness of top flange	$[0]_{8T}$	$[0]_{8T}$	$[0]_{10T}$	
Thickness of bottom flange	$[0]_{8T}$	$[0]_{8T}$	$[0]_{8T}$	
Thickness of web	$[0]_{4T}$	$[0]_{4T}$	$[0]_{4T}$	

Table 7-9 Shear center location comparison between ANSYS Beam Tool and present approach.

	Shear Center			
	ANSYS Beam Tool		Present Approach Eqs. (7-50)	
(inches)	$\mathrm{Y_{So}}$	Z_{So}	$\mathrm{Y_{So}}$	Z_{So}
Case I	0.0000	0.5200	0.0000	0.5200
Case II	0.0726	0.2593	0.0729	0.2587
Case III	0.0630	0.2990	0.0633	0.2983

According to Table 7-9, since case I has symmetrical cross-section, location between shear center and centroid are identical. The lateral distance Y_{So} between shear center and origin is equal to zero. Case II and III has unsymmetrical cross-section, the bending twisting decoupled point is shifted outside of the cross-section. Based on the observation in Table 7-9, shear center results obtained from present approach give an excellent agreement with numerical results from ANSYS Beam Tool. Numerical studies of shear center location and centroid location are provided in Figure 7-8. Thickness for top and bottom flanges and web are 0.04 in. Top flange length is 0.5 in and web length is 1 in. A varied bottom flange length from 0.3 in to 0.8 in is implemented to investigate locations of shear center and centroid. According to Figure 7-8(a), the distance between shear center and origin linearly decreases when the bottom flange length increases. When the bottom flange increases from 0.3 in to 0.8 in, shear center is closer to the bottom flanges than centroid if the bottom flange length is greater than the top flange length due to symmetric cross-section behavior.

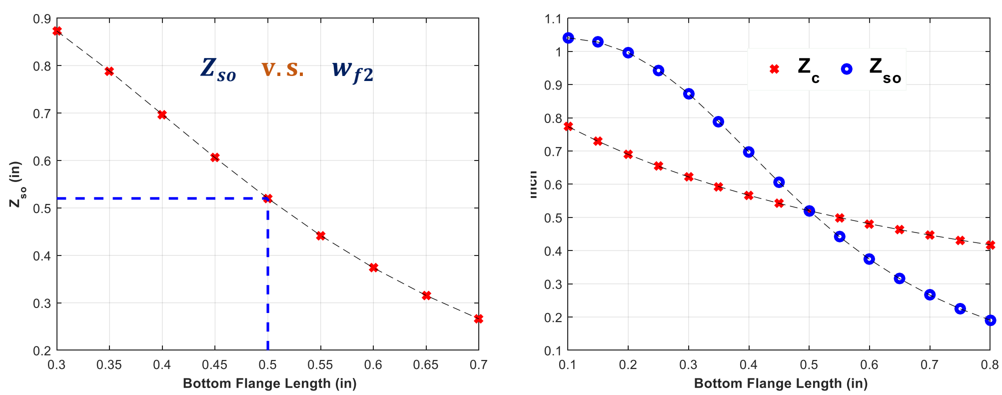

(a) (b)

Figure 7-8 Numerical study of shear center location and centroid location if the length of bottom flange varies from 0.3 in to 0.8 in. Thickness in all flanges and web are identical equals to 0.04 in. The length of top flange is 0.5 in and the length of web is 1 in.

Table 7-10 Effect of fiber orientation

Fiber Orientation	Shear Center	
	Y_{so} (in)	Z_{so} (in)
0°	0.0715	0.2641
15°	0.0741	0.2534
30°	0.0798	0.2248
45°	0.0837	0.1956
60°	0.0847	0.1809
90°	0.0849	0.1767

Effect of fiber orientation is shown in Table 7-10. The designed staking sequence for top flange is $[\pm\theta/0_2/90]_s$, for bottom flange is $[0]_{8T}$, and for web is $[0]_{4T}$, $\theta = 0°, 15°, 30°, 45°, 60°$, and 90°, respectively. The length of top flange is 0.5 in, the length of bottom flange is 0.7 in, and the length of web is 1 in. Based on the observation in Table 7-10, the shear center is closer to the bottom flanges when fiber orientation increases. If fiber orientation increases from 0° to θ°, the stiffness along x-direction (longitudinal direction) decreases, resulted in shorter distance from shear center to the bottom flange. Insignificant distance changes along y-direction with changing fiber orientation. Five cases are selected to investigate overall influence based on stacking sequence, thickness and length for each sub-laminates. Case 1 has symmetrical cross-section with symmetrical/balanced laminate staking sequence. Case 2 and 3 has unsymmetrical cross-sections but still has symmetrical/balanced laminate stacking sequence. Case 4 has unsymmetrical cross-section and unsymmetrical/balanced laminate stacking sequence. Case 5 has unsymmetrical cross-section and unsymmetrical/unbalanced laminate stacking sequence.

Table 7-11 Dimensions and stacking sequences of flanges and web.

Case	Top Flange	Bottom Flange	Web
	Stack Sequence	Stack Sequence	Stack Sequence
	Width (in)	Width (in)	Height (in)
1	$[\pm 45/0/90]_s$	$[\pm 45/0/90]_s$	$[\pm 45]_s$
	0.5	0.5	1.0
2	$[\pm 45/0/90]_s$	$[\pm 45/0/90]_s$	$[\pm 45]_s$
	0.5	0.7	1.0
3	$[\pm 45/0_2/90]_s$	$[\pm 45/0/90]_s$	$[\pm 45]_s$
	0.5	0.7	1.0
4	$[\pm 45/0/90/0/90/\pm 45]_T$	$[\pm 45/0/90/0/90/\pm 45]_T$	$[\pm 45]_s$
	0.5	0.7	1.0
5	$[\pm 45/-60/15/30/0/\pm 45]_T$	$[\pm 45/-60/15/30/0/\pm 45]_T$	$[\pm 45]_s$
	0.5	0.7	1.0

Table 7-12 Warping and torsional stiffness comparison for case 1 between analytical and ANSYS.

Case 1: Orthotropic Material			
	Present	ANSYS Result	Difference %
GK $(psi - in^4)$ Torsional Rigidity	91.18	88.85	2.6 %
EΓ $(\mathrm{psi} - \mathrm{in}^4)$ Warping Rigidity	2598	2607	0.3 %
θ_{sv} (rad)	0.10536	0.10536	0 %
θ_{warp} (rad)	0.05259	0.05454	3.6 %

Table 7-13 Warping and torsional stiffness comparison for case 2 between analytical and ANSYS.

Case 2: Orthotropic Material			
	Present	ANSYS Result	Difference %
GK $(psi - in^4)$ Torsional Rigidity	112.21	108.00	3.9 %
$E\Gamma$ $(\mathrm{psi} - \mathrm{in}^4)$ Warping Rigidity	3666	3694	0.75 %
θ_{sv} (rad)	0.08912	0.08912	0 %
θ_{warp} (rad)	0.04116	0.04187	1.7 %

Table 7-14 Warping and torsional stiffness comparison for case 3 between analytical and ANSYS.

Case 3: Orthotropic Material			
	Present	ANSYS Result	Difference %
GK $(psi - in^4)$ Torsional Rigidity	146.59	142.20	2.7 %
$E\Gamma$ $(\mathrm{psi} - \mathrm{in}^4)$ Warping Rigidity	4773	4536	5.2 %
θ_{sv} (rad)	0.06822	0.06822	0 %
θ_{warp} (rad)	0.03156	0.03284	3.9 %

Table 7-15 Warping and torsional stiffness comparison for case 4 between analytical and ANSYS.

Case 4: Orthotropic Material			
	Present	ANSYS Result	Difference %
GK $(psi - in^4)$ Torsional Rigidity	117.33	114.98	2 %
EΓ $(\mathrm{psi} - \mathrm{in}^4)$ Warping Rigidity	3653	3660	0.2 %
θ_{sv} (rad)	0.08523	0.08523	0 %
θ_{warp} (rad)	0.04024	0.04065	1.1 %

Table 7-16 Warping and torsional stiffness comparison for case 5 between analytical and ANSYS.

Case 5: Orthotropic Material			
	Present	ANSYS Result	Difference %
GK $(psi - in^4)$ Torsional Rigidity	122.44	119.07	2.8 %
EΓ $(\mathrm{psi} - \mathrm{in}^4)$ Warping Rigidity	3508	3493	0.4 %
θ_{sv} (rad)	0.08167	0.08167	0 %
θ_{warp} (rad)	0.03999	0.04071	1.8 %

Table 7-17 Shear center comparison between present and ANSYS.

Case	Shear Center			
	Isotropic		Composite	
	Y_{so} (in)	Z_{so} (in)	Y_{so} (in)	Z_{so} (in)
1	0.000	0.520	0	0.52
2	0.073	0.259	0.079	0.266
3	0.063	0.299	0.037	0.365
4	0.073	0.259	0.080	0.264
5	0.073	0.259	0.076	0.269

Based on the observation from Table 7-12 to Table 7-16, results obtained from present approach give an excellent agreement compared to numerical results obtained from ANSYS. The shear center location comparison between present and ANSYS is shown in Table 7-17. Shear center location of Z-stiffener using isotropic material is only functional of geometry of cross-section. However, for composite Z-stiffener, it is functional of not only geometry of the cross-section but stacking sequence of the laminate. According to Table 7-17 case 1, shear center location using isotropic material properties is identical with shear center location using composite material properties. Hence, it can be concluded that shear center location is dependent on structural configuration only if the entire beam is made of same family laminates regardless the ply orientation and the stacking sequence.

The fiber orientation effect of warping stiffness and torsional stiffness are discussed. The stacking sequence for top flange is $[\pm\theta/0_2/90]_s$, for bottom flange is $[\pm\theta/0_2/90]_s$, and for web is $[\pm 45]_s$ where θ = 0°, 15°, 30°, 45°, 60°, 75° and 90° to investigate the effect of fiber orientations. It should be noted that $w_{f1} = 0.5\ in$, $w_{f2} = 0.7\ in$, and $w_w = 1.0\ in$. The torsional stiffness and warping stiffness based on fiber orientation is tabulated in Table 7-18 and is shown in Figure 7-9.

Table 7-18 Torsional stiffness varied based on fiber orientation.

Fiber Orientation	Stiffness $\mathrm{lb-in}^2$			
	Analytical		ANSYS	
	Torsion GK	Warping EI_w	Torsion GK	Warping EI_w
0°	33.16	6006	36.75	5635
15°	54.24	5615	56.23	5578
30°	94.34	4622	92.48	4739
45°	112.21	3666	108.00	3694
60°	91.58	3202	89.36	3229
75°	52.52	3080	53.86	3096
90°	33.16	3065	35.76	2997

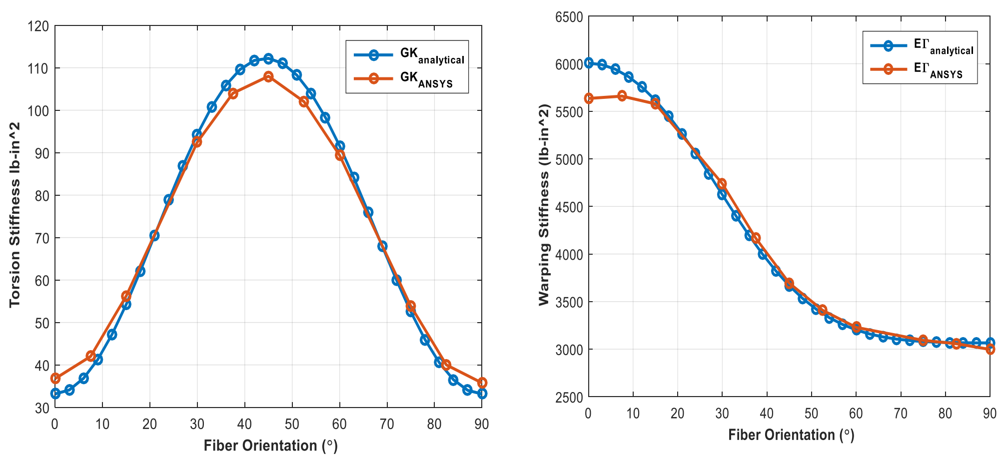

(a) (b)

Figure 7-9 (a) Torsional stiffness (b) warping comparison between present and ANSYS results (case 2).

Excellent agreements between the present method and FEM are observed except small fiber orientation. It is also shown that flange laminates with 45° ply in $[\pm\theta/0/90]_s$ layup gives higher torsional stiffness and 0° ply in $[\pm\theta/0/90]_s$ layup exhibits higher warping stiffness.

7-5.3 Comparison between Narrow and Wide Beam Assumption for Composite Z-Stiffener

Difference between a beam with general, narrow and wide sections is discussed. For the width to height ratio is less than 6, the narrow beam deflection results have more accuracy than general beam results compared with FE analysis provided by Lu [111]. However, there is a need to investigate the difference between outcomes obtained from narrow beam assumption and wide beam assumption. Opposite to a narrow beam, wide beam acting essentially as a plate does not show distortion of the cross-section. As a result, curvatures K_y and K_{xy} are restrained. It should be noted that N_y, N_{xy}, M_y, and M_{xy} are induced due to strains and curvatures restrained. The comparison between narrow and wide beam concept are shown in Table 7-19. According to Table 7-19, stiffness results obtained from narrow beam assumption has errors less than 3 % compared with FE analysis.

Table 7-19 Comparison between narrow and wide beam assumptions.

	Case 2			Case 3		
	A_x	K_y^c	K_z^c	A_x	K_y^c	K_z^c
Narrow	4.436E5	2.951E-06	3.771E-06	5.787E5	2.248E-6	2.730E-6
Wide	5.397E5	2.395E-6	3.052E-6	6.758E5	1.909E-6	2.329E-6
ANSYS	4.424E5	2.953E-06	3.777E-06	5.779E5	2.233E-6	2.728E-6
% Diff. (Narrow)	-0.25	0.07	0.16	-0.13	0.67	0.07
% Diff. (Wide)	21.93	18.89	19.16	-17.12	-14.51	-14.63
	Case 4			Case 5		
	A_x	K_y^c	K_z^c	A_x	K_y^c	K_z^c
Narrow	4.430E5	2.953E-6	3.774E-6	4.222E5	3.002E-6	3.805E-6
Wide	5.398E5	2.395E-6	3.050E-6	5.973E5	2.173E-6	2.772E-6
ANSYS	4.423E5	2.955E-6	3.746E-6	4.223E5	3.11E-6	3.875E-6
% Diff. (Narrow)	-0.19	0.07	-0.75	0.03	2.99	1.29
% Diff. (Wide)	22.04	-18.95	-18.58	41.44	-30.13	-28.46

7-6 Conclusion for Composite Z-Stiffener

An analytical method is developed to calculate the sectional properties and ply stresses of the z-beam under torsion. The sectional properties include shear center, equivalent torsional and wrapping stiffness of a laminated composite beam with Z cross-section. The developed expression takes into consideration of the structural deformation characteristics of composite beam with narrow section. The difference between beams with narrow and wide sections is studied. The sectional properties and the ply stresses of flanges and web laminates are computed for composite Z-stiffener torsional loads. The present results give excellent agreement with the results obtained from ANSYS™. A parametric study of shear center and centroid with various layup sequences ranging from the combination of symmetric/unsymmetrical and balanced/unbalanced laminates was performed using the present solution. It is found that the sectional properties of a composite Z-stiffener structure are dependent on the laminate material properties and stacking sequence besides its structural configuration if the flange and web laminates are made of different family of laminates. However, the sectional properties are dependent on structural configuration only if the entire beam is made of same family laminates regardless the ply orientation and the stacking sequence. It is concluded that the present approach for analyzing a composite z-stiffener is a viable and efficient method for composite z-stiffener design.

Chapter 8

CONCLUSION AND FURTURE WORK

This research fundamentally provides the analytical development of simple closed-form solutions for accurately predicting key structural characteristics such as equivalent axial stiffness, bending stiffness, and ply-stress variations for a composite curved beam under bending. A closed-form analytical solution is developed for analyzing laminated composite beam with and without curvature and fiber waviness, respectively. The explicit expression for evaluating axial and bending stiffness are formulated based on consideration of structural deformation of beam with narrow cross-section. Closed-form solutions are also provided to predict overall structural stiffness behavior for a composite curved beam with in-plane fiber waviness or out-of-plane fiber waviness. FE analysis is conducted for verifying the analytical results. The present stiffness and stress variation results have excellent agreement with numerical results obtained from ABAQUS. Significant stiffness reduction is observed when fiber waviness ratio R varies from 0 to 0.3. A specific ratio when $R = 0.72$ is introduced, where Young's modulus along the x-direction and y-direction are identical. If the ratio is over 0.72, the stiffness along the y-direction is greater than the stiffness along the x-direction because larger portion of fiber now align in the y-direction, which contributes the most stiffness for the structure. In curved laminate stage, both axial stiffness and bending stiffness decrease for a composite curved beam with fiber waviness. It is more pronounced for axial stiffness since significant axial stiffness reduction is observed when the amplitude of fiber waviness increases. However, fiber waviness has less impact on the bending stiffness of plies which is affected by fiber wariness near the middle axis of the composite curved beam. The maximum radial stress for a composite curved beam with fiber waviness under bending is discussed. The maximum radial stress increases about 25 % when a fiber waviness is present and the fiber waviness amplitude is equal to 10 % of the total thickness of the beam. It is concluded that the present approach can provide an efficient method for analyzing laminated composite curved beam with in-plane and out-of-plane fiber waviness.

The analytical closed-form solution is developed to calculate the total strain ERR for a composite curved beam under bending. The crack is allowed to locate in any arbitrary interface and location in the present research. Symmetrical model and unsymmetrical model are developed to capture the total strain ERR. Linear scaling parameters are provided to predict the total strain ERR in the present approach to aim the void where inaccurate strain ERR is obtained for a given small crack. FE analysis is implemented to verify analytical results, VCCT techniques is implemented and the total strain ERR in the crack tips are studied. If the total crack angle is 5.4°, a bending moment 8.356 N-m can be applied on the composite curved beam without failure. However, if the total crack angle 32.4° is considered, only a moment 3.287 N-m can be applied on the composite curved beam without failure. Significant failure loading reduction is observed when crack angle increases from 5.4° to 32.4°. The total strain ERR also varies with the radius of crack. The strain ERR reaches to maximum at the location where maximum σ_r is observed of a prefect composite curved beam under bending. The effect of crack hoop location is also investigated. If crack locates near $\theta_h = 40°$, the applied moment is 38 % higher than the crack locates at $\theta_h = 0°$. In conclusion, the present successfully fills the void where previous authors couldn't predict accurately for a composite curved beam with a small crack. Moreover, this study allows the crack can be located in any interface and hoop locations, which provides a feasible way to efficiently analyze composite curved beam with a crack and the total strain ERR results can be predicted accurately for the type of curved beam where $\mathrm{R_m}/t$ ratio is less than 3.5.

The last chapter discussed of composite Z-stiffener which is the application of composite curved beam. An analytical method is developed to calculate the sectional properties and ply stresses of the z-beam under torsion. The sectional properties include shear center, equivalent torsional and wrapping stiffness of a laminated composite beam with Z cross-section. Narrow beam assumption has to be applied if a thin-walled structures is considered. The equivalent stiffness comparison between NB and WB assumptions is provided. The present results give excellent agreement with the results obtained from ANSYS™. A parametric study of shear center and centroid with various layup sequences ranging from the combination of symmetric/unsymmetrical and balanced/unbalanced laminates was performed using the present solution. It is found that the sectional properties of a composite Z-stiffener structure are dependent on the laminate material properties and stacking sequence besides its structural configuration if the flange and web laminates are made of different family of laminates. However, the sectional properties are dependent on structural configuration only if the entire beam is made of same family laminates regardless the ply orientation and the stacking sequence.

In conclusion, the present research provides an overall study of composite curved beam with fiber waviness and delamination under bending. Equivalent stiffness closed-form solutions to calculate axial and bending stiffness are provided for a composite curved beam with/without curvature and fiber waviness, respectively. The closed-form analytical solution for analyzing composite curved beam with delamination is developed. Torsional stiffness and warping stiffness are also studied for a composite Z-stiffener. It is concluded that the present approach is a viable and efficient method for composite beam design with and without fiber waviness and delamination. The research initiated in this study provides further motivation to the following topics:

- Shear stress prediction for a composite curved beam with an out-of-plane fiber waviness.
- 3-D numerical modeling of investigation in composite curved beam with a void using VCCT.
- Stress concentration factor of voids and stress intensity factor of cracks inside the composite curved beam under bending.
- Extend present approach to study “Spring-in” and “Spring-out” effects where data is provided from [112].

Appendix A

The average compliance constant of 0° ply with fiber waviness S'_{ij} are

$$S'_{11} = \frac{1}{L}[S_{11}I_1 + (2S_{12} + S_{66})I_3 + S_{22}I_5]$$

$$S'_{12} = \frac{1}{L}[(S_{11} + S_{22} - S_{66})I_3 + S_{12}(I_1 + I_5)]$$

$$S'_{13} = \frac{1}{L}[S_{13}I_6 + S_{23}I_7]$$

$$S'_{16} = \frac{1}{L}[(2S_{11} - 2S_{12} - S_{66})I_2 - (2S_{22} - 2S_{12} - S_{66})I_4]$$

$$S'_{22} = \frac{1}{L}[S_{11}I_5 + (2S_{12} + S_{66})I_3 + S_{66}I_1]$$

$$S'_{23} = \frac{1}{L}[S_{13}I_7 + S_{23}I_6]$$

$$S'_{26} = \frac{1}{L}[(2S_{11} - 2S_{12} - S_{66})I_4 - (2S_{22} - 2S_{12} - S_{66})I_2]$$

$$S'_{33} = S_{33}$$

$$S'_{44} = \frac{1}{L}[S_{44}I_6 + S_{55}I_7]$$

$$S'_{45} = \frac{1}{L}[I_8(S_{55} - S_{44})]$$

$$S'_{66} = \frac{1}{L}[2(2S_{11} + 2S_{22} - 4S_{12} - S_{66})I_3 + S_{66}(I_1 + I_5)]$$

where

$$\mathrm{I}_1 = \int_0^L \cos^4\phi\, dx = \frac{L}{\pi}\int_0^{\pi} \frac{d\psi}{(1 + a^2\cos^2\psi)^2} = \frac{L}{\pi}J_1$$

$$\mathrm{I}_2 = \int_0^{\frac{L}{2}} \cos^3\phi\, sin\phi\, dx = \frac{L}{\pi}\int_0^{\frac{\pi}{2}} \frac{a\, cos\,\psi}{(1 + a^2\cos^2\psi)^2}\, d\psi = \frac{L}{\pi}J_2$$

$$I_3 = \int_0^{\frac{L}{2}} cos^2\phi\, sin^2\phi\, dx = \frac{L}{\pi}\int_0^{\pi} \frac{a^2\, cos^2\psi}{(1 + a^2\, cos^2\psi)^2}\, d\psi = \frac{L}{\pi}J_2$$

$$I_4 = \int_0^{\frac{L}{2}} cos\,\phi\, sin^3\phi\, dx = \frac{L}{\pi}\int_0^{\frac{\pi}{2}} \frac{a^3\, cos^3\psi}{(1 + a^2\, cos^2\psi)^2}\, d\psi = \frac{L}{\pi}J_4$$

$$I_5 = \int_0^L sin^4\phi\, dx = \frac{L}{\pi}\int_0^{\pi} \frac{a^4\, cos^4\psi}{(1 + a^2\, cos^2\psi)^2}\, d\psi = \frac{L}{\pi}J_5$$

$$I_6 = \int_0^L cos^2\phi\, dx = I_1 + I_3$$

$$I_6 = \int_0^L sin^2\phi\, dx = I_3 + I_5$$

$$I_6 = \int_0^L cos\,\phi\, sin\,\phi\, dx = I_2 + I_4$$

and

$$\mathrm{J}_0 = \frac{\pi}{\sqrt{1 + a^2}}$$

$$J_1 = J_0 - \frac{a^2}{2\pi^2} J_0^3$$

$$J_2 = \frac{a}{2(1+a^2)} + \frac{1}{4(1+a^2)^{1.5}} \ln\left(\frac{\sqrt{1+a^2}+a}{\sqrt{1+a^2}-a}\right)$$

$$J_3 = \frac{a^2}{2\pi^2} J_0^3$$

$$J_4 = (1+2a^2) J_2 - a$$

$$J_5 = \pi - J_0 - \frac{a^2}{2\pi^2} J_0^3$$

The 0° S matrix with waviness properties is presented below.

$$[S'] = \begin{bmatrix} S'_{11} & S'_{12} & S'_{13} & 0 & 0 & S'_{16} \\ S'_{12} & S'_{22} & S'_{23} & 0 & 0 & S'_{26} \\ S'_{13} & S'_{23} & S_{33} & 0 & 0 & S'_{36} \\ 0 & 0 & 0 & S'_{44} & S'_{45} & 0 \\ 0 & 0 & 0 & S'_{45} & S'_{55} & 0 \\ 0 & 0 & 0 & 0 & 0 & S'_{66} \end{bmatrix}$$

Next, S' matrix can be rotated with respect to z-direction with transformation matrix as shown below.

$$[T_\sigma(\theta)]_z = \begin{bmatrix} m^2 & n^2 & 0 & 0 & 0 & 2mn \\ n^2 & m^2 & 0 & 0 & 0 & -2mn \\ 0 & 0 & 1 & 0 & 0 & 0 \\ 0 & 0 & 0 & m & -n & 0 \\ 0 & 0 & 0 & n & m & 0 \\ -mn & mn & 0 & 0 & 0 & m^2-n^2 \end{bmatrix}$$

$$[\mathrm{T}\varepsilon(\theta)]_z = \begin{bmatrix} m^2 & n^2 & 0 & 0 & 0 & mn \\ n^2 & m^2 & 0 & 0 & 0 & -mn \\ 0 & 0 & 1 & 0 & 0 & 0 \\ 0 & 0 & 0 & m & -n & 0 \\ 0 & 0 & 0 & n & m & 0 \\ -2mn & 2mn & 0 & 0 & 0 & m^2 - n^2 \end{bmatrix}$$

where $\mathrm{m} = \cos\theta$, $\mathrm{n} = \sin\theta$, and θ is fiber orientation. After rotation with respect to z-axis, the in-plane compliance matrix $[\bar{\mathrm{S}}']$ can be obtained.

$$[\bar{\mathrm{S}}'] = [\mathrm{T}\varepsilon(-\theta)]_z[S][\mathrm{T}_\sigma(\theta)]_z$$

The average properties are

$$\overline{E_1} = \frac{1}{\bar{S}'_{11}}, \overline{E_2} = \frac{1}{\bar{S}'_{22}}, \overline{G_{12}} = \frac{1}{\bar{S}'_{66}}, \overline{\nu_{12}} = -\frac{\bar{S}_{12}{}'}{\bar{S}'_{11}},$$

$$\bar{\alpha}_1 = \frac{1}{L}(\alpha_1 I_6 + \alpha_2 I_7) \;\; \bar{\alpha}_2 = \frac{1}{L}(\alpha_1 I_7 + \alpha_2 I_6) \;\; \bar{\alpha}_{12} = \frac{2}{L}(\alpha_1 - \alpha_2) I_8$$

Appendix B

During the preceding of increasing the strain, the wave amplitude and wavelength of the fiber are changed. Subsequently, the effective moduli of wave ply are also changed. Therefore, recalculation of the material properties at each step of strain increment is required. The average Young's modulus in 1-direction can be expressed as

$$\overline{E_x} = \frac{1}{\bar{S}'_{11}}$$

Next, for a given loading either tension or thermal loading, stress can be transformed from x-y coordinate into the 1-2 (in-plane) coordinate.

$$\begin{Bmatrix} \Delta\sigma_1 \\ \Delta\sigma_2 \\ \Delta\sigma_3 \\ \Delta\tau_{23} \\ \Delta\tau_{13} \\ \Delta\tau_{12} \end{Bmatrix} = [\mathrm{T}_\sigma(\theta)]_\mathrm{z} \begin{Bmatrix} \Delta\sigma_\mathrm{x} \\ \Delta\sigma_\mathrm{y} \\ \Delta\sigma_z \\ \Delta\tau_{23} \\ \Delta\tau_{13} \\ \Delta\tau_{12} \end{Bmatrix}$$

where

$$\Delta\sigma_\mathrm{x} = \sigma_x + \sigma_x^T$$

$$\Delta\sigma_\mathrm{y} = \sigma_y + \sigma_y^T$$

$$\Delta\sigma_\mathrm{z} = \sigma_z + \sigma_z^T$$

$$\Delta\tau_\mathrm{yz} = \tau_{yz} + \tau_{yz}^T$$

$$\Delta\tau_\mathrm{xz} = \tau_{xz} + \tau_{xz}^T$$

$$\Delta\tau_\mathrm{xy} = \tau_{xy} + \tau_{xy}^T$$

Next, stress can be transformed from 1-2 coordinate into $\bar{1}-\bar{2}$ (out of plane) coordinate. The incremental strains in $\bar{1}-\bar{2}$ coordinate can be computed by using stress-strain relationships.

$$\begin{Bmatrix} \overline{\Delta\sigma_1} \\ \overline{\Delta\sigma_2} \\ \overline{\Delta\sigma_3} \\ \overline{\Delta\tau_{23}} \\ \overline{\Delta\tau_{13}} \\ \overline{\Delta\tau_{12}} \end{Bmatrix} = [\mathrm{T}_\sigma(\theta)]_\mathrm{x} \begin{Bmatrix} \Delta\sigma_1 \\ \Delta\sigma_2 \\ \Delta\sigma_3 \\ \Delta\tau_{23} \\ \Delta\tau_{13} \\ \Delta\tau_{12} \end{Bmatrix}$$

$$\begin{Bmatrix} \overline{\Delta\varepsilon_1} \\ \overline{\Delta\varepsilon_2} \\ \overline{\Delta\varepsilon_3} \\ \overline{\Delta\gamma_{23}} \\ \overline{\Delta\gamma_{13}} \\ \overline{\Delta\gamma_{12}} \end{Bmatrix} = \bar{\mathrm{S}}' \begin{Bmatrix} \overline{\Delta\sigma_1} \\ \overline{\Delta\sigma_2} \\ \overline{\Delta\sigma_3} \\ \overline{\Delta\tau_{23}} \\ \overline{\Delta\tau_{13}} \\ \overline{\Delta\tau_{12}} \end{Bmatrix}$$

Since fiber waviness is along 1-direction, the new fiber waviness length L' is

$$\mathrm{L}' = \mathrm{L}(1 + \overline{\Delta\varepsilon_1})$$

Calculate original fiber length, ℓ, by using original amplitude, A, and length, L. Assuming $\varphi = \frac{\pi \mathrm{x}}{\mathrm{L}}, \mu = \pi^2 R^2, and\ \eta^2 = \frac{\mu}{1+\mu}$,

$$\frac{\ell}{\mathrm{L}} = 1 + \frac{1}{4}\eta^2 + \frac{13}{64}\eta^4 + \frac{45}{256}\eta^6 + \frac{2577}{16384}\eta^8 + \frac{9417}{65536}\eta^{10} + \cdots$$

The value of ℓ/L will coverage to the fourth digit after decimal point when using the first 4 items if R less than 0.3 and using the first 6 items if R less than 0.5.

To calculate new fiber length, ℓ', coordinate system from x-y coordinate system to 1'-2' coordinate system has to be considered where 1' and 2' are coordinate system corresponding to fiber angles along waviness. For given loadings including mechanical and thermal loads, 1'-2' (along fiber direction) stresses can be found by using stress transformation

$$\begin{Bmatrix} \Delta\sigma_1 \\ \Delta\sigma_2 \\ \Delta\sigma_3 \\ \Delta\tau_{23} \\ \Delta\tau_{13} \\ \Delta\tau_{12} \end{Bmatrix} = [\mathrm{T}_\sigma(\theta)]_\mathrm{z} \begin{Bmatrix} \Delta\sigma_\mathrm{x} \\ \Delta\sigma_\mathrm{y} \\ \Delta\sigma_z \\ \Delta\tau_{23} \\ \Delta\tau_{13} \\ \Delta\tau_{12} \end{Bmatrix}$$

where

$$\mathrm{m} = \cos(\theta + \phi)\,;\;\; n = \sin(\theta + \phi)$$

$$\phi = \tan^{-1}\left[\frac{\pi A}{L}\cos\left(\frac{\pi x}{L}\right)\right]$$

$$\theta = \text{fiber orientation}$$

After rotating respect with z-axis, the incremental strain in $1' - 2'$ coordinate system can be computed using stress-strain relationship.

$$\begin{Bmatrix} \overline{\Delta\sigma_1'} \\ \overline{\Delta\sigma_2'} \\ \overline{\Delta\sigma_3'} \\ \overline{\Delta\tau_{23}'} \\ \overline{\Delta\tau_{13}'} \\ \overline{\Delta\tau_{12}'} \end{Bmatrix} = [\mathrm{T}_\sigma(\theta)]_\mathrm{z} \begin{Bmatrix} \Delta\sigma_1 \\ \Delta\sigma_2 \\ \Delta\sigma_3 \\ \Delta\tau_{23} \\ \Delta\tau_{13} \\ \Delta\tau_{12} \end{Bmatrix}$$

$$\begin{Bmatrix} \Delta\varepsilon_1' \\ \Delta\varepsilon_2' \\ \Delta\varepsilon_3' \\ \Delta\gamma_{23}' \\ \Delta\gamma_{13}' \\ \Delta\gamma_{12}' \end{Bmatrix} = \begin{bmatrix} S_{11} & S_{12} & S_{13} & 0 & 0 & 0 \\ S_{12} & S_{22} & S_{23} & 0 & 0 & 0 \\ S_{13} & S_{23} & S_{33} & 0 & 0 & 0 \\ 0 & 0 & 0 & S_{44} & 0 & 0 \\ 0 & 0 & 0 & 0 & S_{55} & 0 \\ 0 & 0 & 0 & 0 & 0 & S_{66} \end{bmatrix} \begin{Bmatrix} \Delta\sigma_1 \\ \Delta\sigma_2 \\ \Delta\sigma_3 \\ \Delta\tau_{23} \\ \Delta\tau_{13} \\ \Delta\tau_{12} \end{Bmatrix}$$

where [S] are original compliance constants. Therefore, the new fiber length ℓ' can be calculated as

$$\ell' = \ell(1 + \Delta\varepsilon_1')$$

Once the new length of waviness and the new fiber length are found, the new amplitude can be computed by using equation shown below.

$$\frac{\ell'}{\mathrm{L}'} = 1 + \frac{1}{4}\eta'^2 + \frac{13}{64}\eta'^4 + \frac{45}{256}\eta'^6 + \frac{2577}{16384}\eta'^8 + \frac{9417}{65536}\eta'^{10} + \cdots$$

where

$$\varphi' = \frac{\pi \mathrm{x}}{\mathrm{L}'}, \mu' = \pi^2 R'^2, and\ \eta'^2 = \frac{\mu'}{1 + \mu'}$$

Since new amplitude and length of fiber waviness are obtained. The new Young's modulus can be calculated.

Appendix C

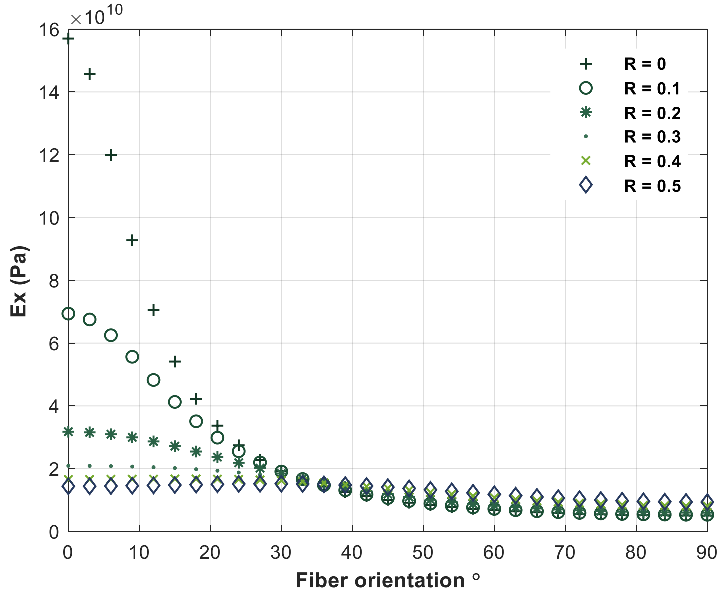

Figure C-1 Comparison between fiber orientation and waviness ratio R of $\bar{E}_{\mathrm{x}}$.

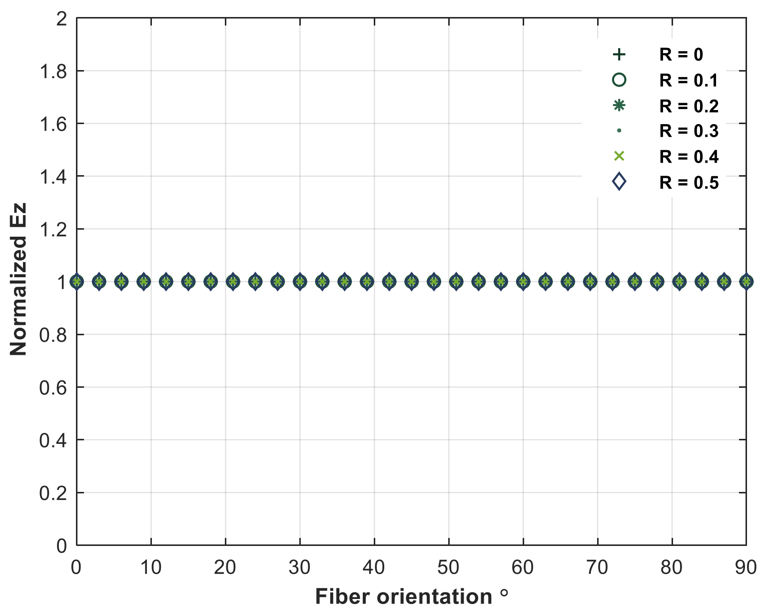

Figure C-2 Comparison between fiber orientation and waviness ratio R of $\bar{E}_{\mathrm{z}}$

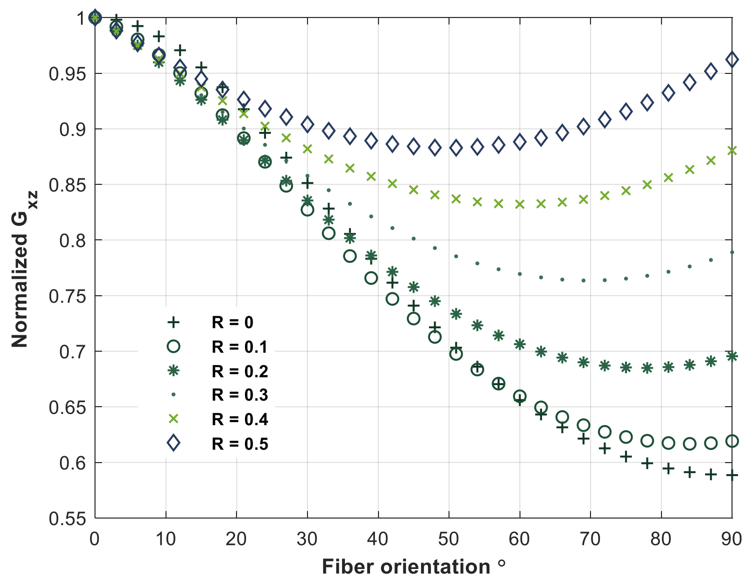

Figure C-3 Comparison between fiber orientation and waviness ratio R of $\bar{G}_{\mathrm{xz}}$

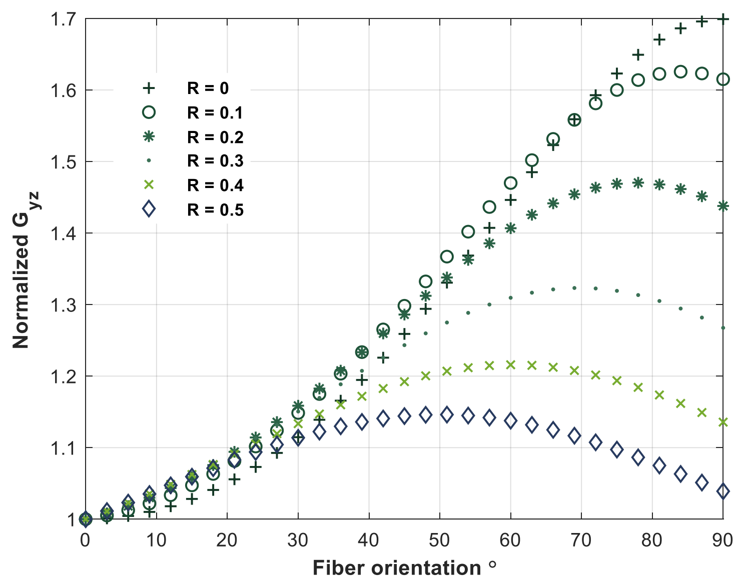

Figure C-4 Comparison between fiber orientation and waviness ratio R of $\bar{G}_{\mathrm{yz}}$

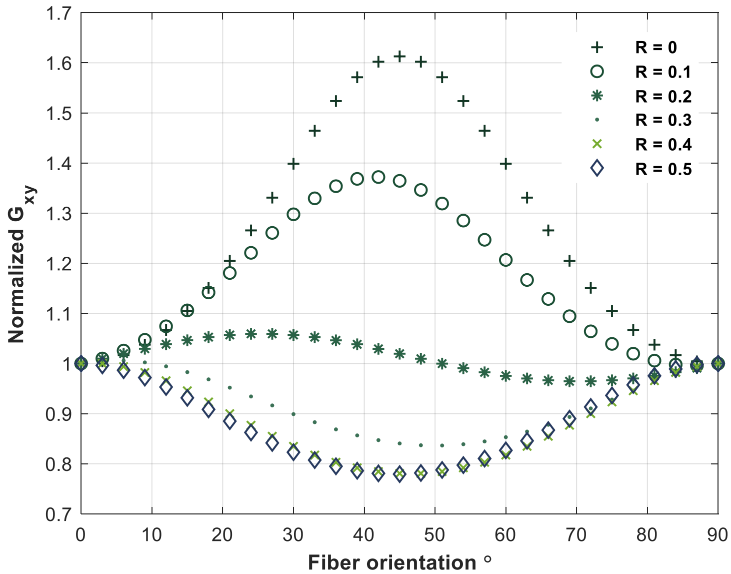

Figure C-5 Comparison between fiber orientation and waviness ratio R of $\bar{G}_{xy}$

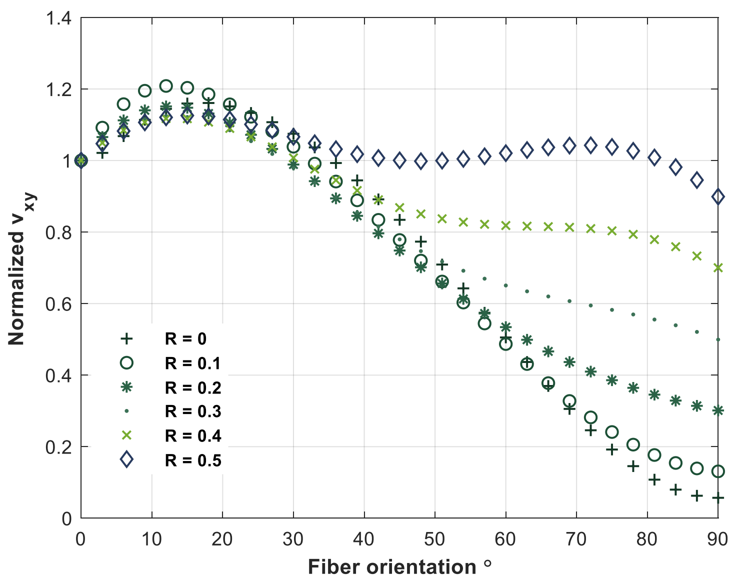

Figure C-6 Comparison between fiber orientation and waviness ratio R of v_{xy}

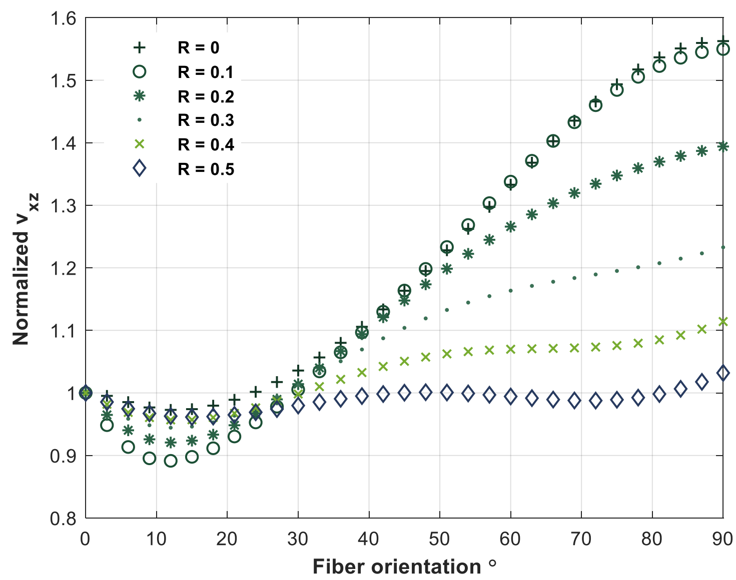

Figure C-7 Comparison between fiber orientation and waviness ratio R of v_{xz}

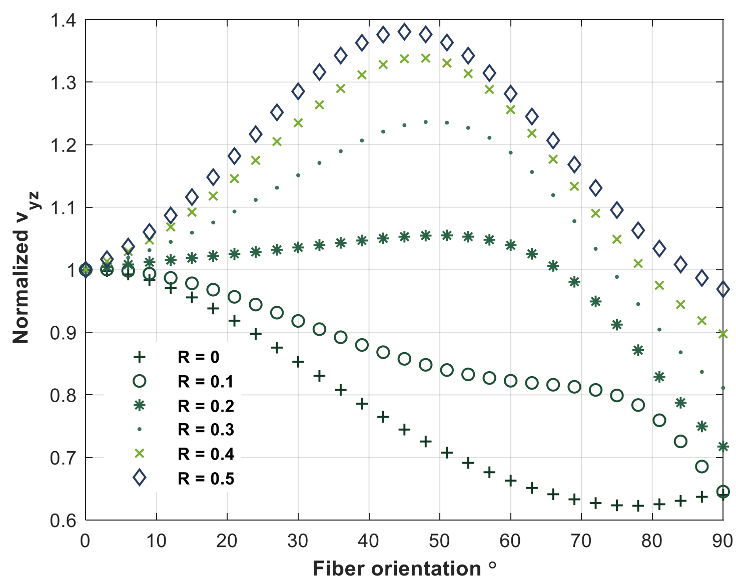

Figure C-8 Comparison between fiber orientation and waviness ratio R of v_{yz}

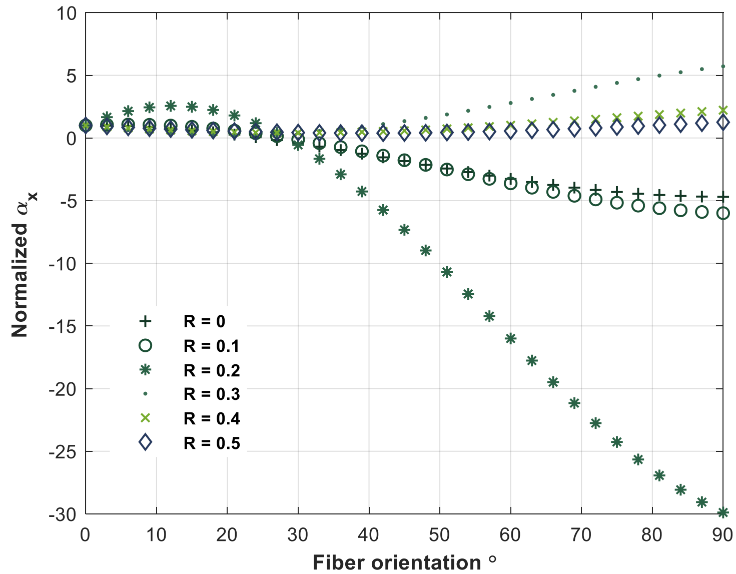

Figure C-9 Comparison between fiber orientation and waviness ratio R of α_x

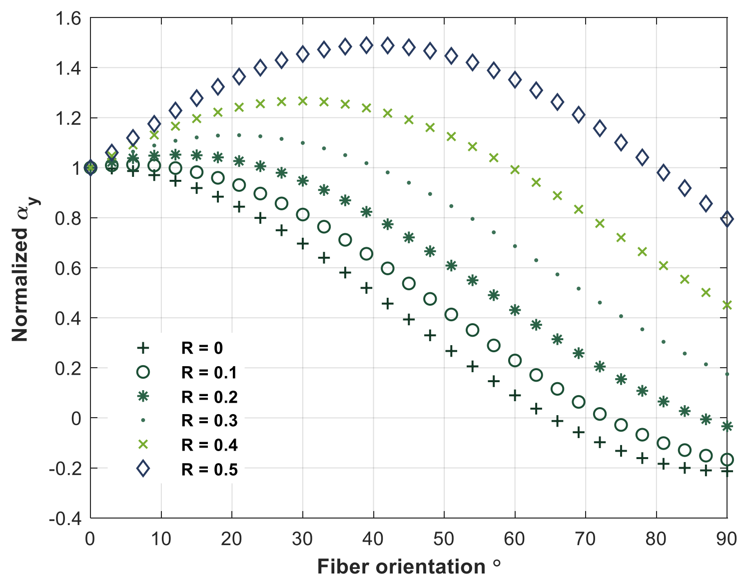

Figure C-10 Comparison between fiber orientation and waviness ratio R of α_y

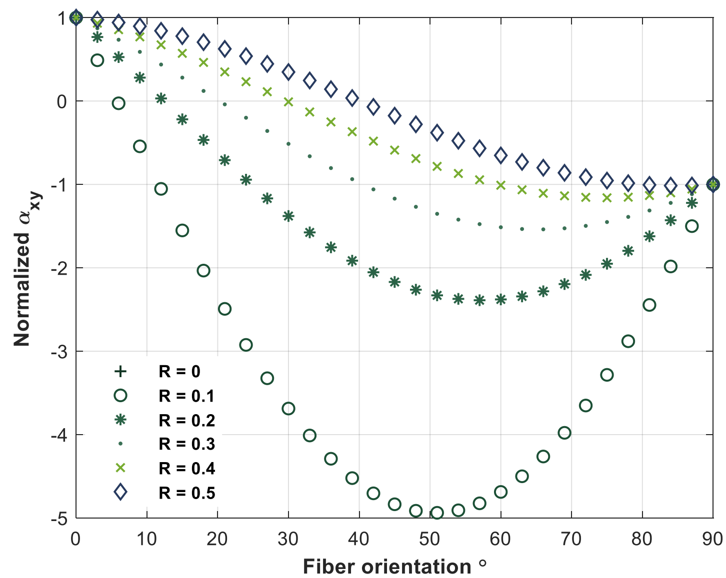

Figure C-11 Comparison between fiber orientation and waviness ratio R of α_{xy}

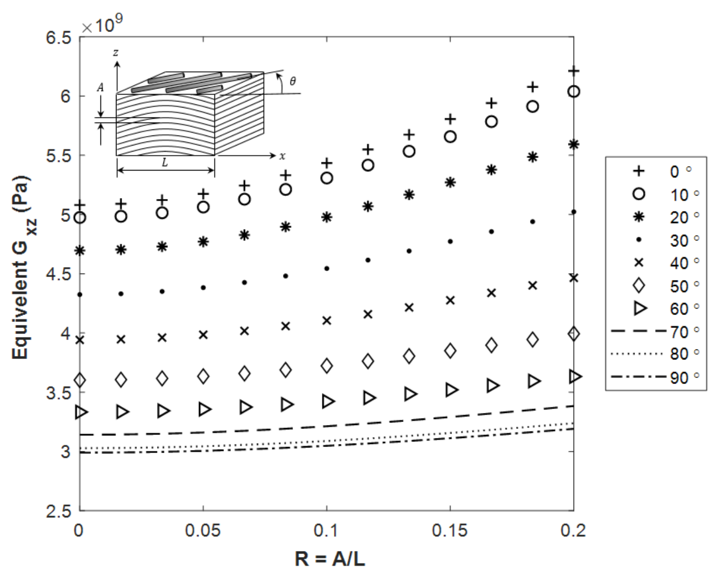

Figure C-12 Equivalent shear modulus in x-z plane comparison with stack sequence $[\pm\theta, 0_2, 90_2]_s$

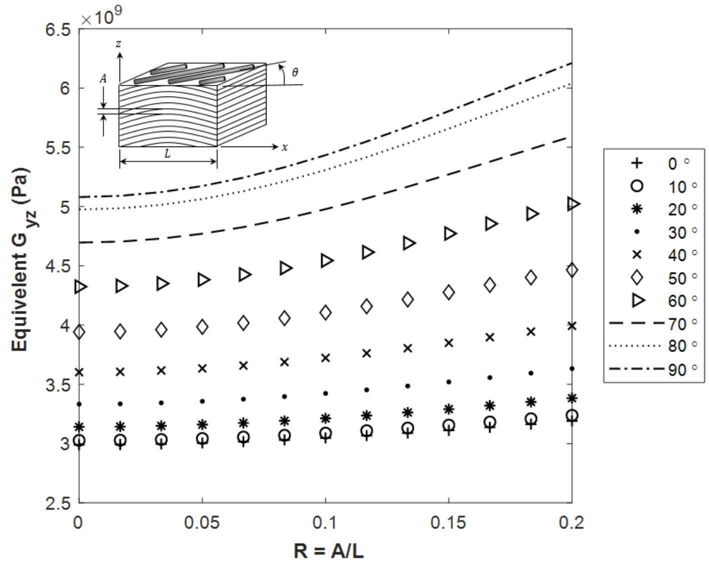

Figure C-13 Equivalent shear modulus in y-z plane comparison with stack sequence $[\pm\theta, 0_2, 90_2]_s$

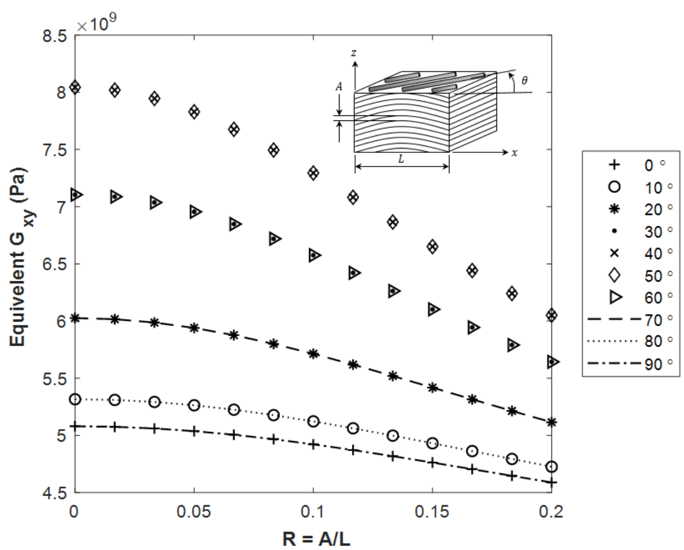

Figure C-14 Equivalent shear modulus in x-y plane comparison with stack sequence $[\pm\theta, 0_2, 90_2]_s$

REFERENCE

1. Love, A. E. H. (1888). The small free vibrations and deformation of a thin elastic shell. Philosophical Transactions of the Royal Society of London. A, 179, 491-546.
2. Timoshenko, S. P., 1921, On the correction factor for shear of the differential equation for transverse vibrations of bars of uniform cross-section, Philosophical Magazine, p. 744.
3. TIMOSHENKSO.., A N D J . N. GOODIER.1 951. Theory of elasticity. 2nd ed. McGraw-Hill, N.Y. Pp.
4. ODEN. T. J. 1967. Mechanics of elastic structures. McGraw-Hill, N.Y.
5. Lekhnitskii, S. G. (1968). Anisotropic plates (No. FTD-HT-23-608-67). Foreign Technology Div Wright-Patterson Afb Oh.
6. Cheung, C. K., & Sorensen, H. C. (1982). Effect of axial loads on radial stress in curved beams. Wood and Fiber Science, 15(3), 263-275.
7. Tolf, G. (1983). Stresses in a curved laminated beam. Fibre Science and Technology, 19(4), 243-267.
8. Ko, W. L. (1988). Delamination stresses in semicircular laminated composite bars.
9. Shenoi, R. A., & Wang, W. (2001). Through-thickness stresses in curved composite laminates and sandwich beams. Composites Science and Technology, 61(11), 1501-1512.
10. Ko, W. L., & Jackson, R. H. (1989). Multilayer theory for delamination analysis of a composite curved bar subjected to end forces and end moments. In Composite structures 5 (pp. 173-198). Springer, Dordrecht.
11. Wang, W., & Shenoi, R. A. (2004). Analytical solutions to predict flexural behavior of curved sandwich beams. Journal of Sandwich Structures & Materials, 6(3), 199-216.
12. Ko, W. L., & Jackson, R. H. (1989). Multilayer theory for delamination analysis of a composite curved bar subjected to end forces and end moments. In Composite structures 5 (pp. 173-198). Springer, Dordrecht.
13. Nguyen, T. (2010). Effects of Curvature on the Stresses of a Curved Laminated Beams subjected to Bending.
14. Sushanta G. & Kashinath S. (2017). A review on stress and deformation analysis of cirved beams under large deflection. International Journal of Engineering and Technologies.
15. Qatu, M. S. (1993). Theories and analyses of thin and moderately thick laminated composite curved beams. International Journal of Solids and Structures, 30(20), 2743-2756.
16. Erkmen, R. E., & Bradford, M. A. (2009). Nonlinear elastic analysis of composite beams curved in-plan. Engineering Structures, 31(7), 1613-1624.
17. Aggarwal, M. (2016). Analysis of curved composite beam. West Virginia University.
18. Tan, E. L., & Uy, B. (2009). Experimental study on curved composite beams subjected to combined flexure and torsion. Journal of Constructional Steel Research, 65(8-9), 1855-1863.
19. Yu, W., Hodges, D. H., Volovoi, V., & Cesnik, C. E. (2002). On Timoshenko-like modeling of initially curved and twisted composite beams. International Journal of Solids and Structures, 39(19), 5101-5121.
20. Zhang, Y., Hou, Z., Li, Y., & Wang, Y. (2015). Torsional behaviour of curved composite beams in construction stage and diaphragm effects. Journal of Constructional Steel Research, 108, 1-10.
21. Lee, J., & Soutis, C. (2007) A study on the compressive strength of thick carbon fibre-epoxy laminates. Composite science and technology, 67(10), 2015-2026.

22. Kantharaju, H. (2012). Analysis of fiber waviness in laminated composite subjected to compressive loads (Doctoral dissertation, Wichita State University).
23. Kugler, D., & Moon, T. J. (2002). Identification of the most significant processing parameters on the development of fiber waviness in thin laminates. Journal of Composite Materials, 36(12), 1451-1479.
24. Yousaf, Z. (2014). Investigation of deformation behaviour of dry textiles under forming forces by computed tomography(Doctoral dissertation, University of Manchester).
25. Masters, J. E., Naik, R., & Minguet, P. J. (1995). Effects of preform architecture on modulus and strength of 2-D triaxially braided textile composites
26. Minguet, P. (1994, July). A comparison of graphite/epoxy tape laminates and 2-D braided composites mechanical properties. In 36th Structures, Structural Dynamics and Materials Conference (p. 1158).
27. Jackson, W. C., & Portanova, M. A. (1995). Out-of-plane properties.
28. Whitcomb, J., & Srirengan, K. (1996). Effect of various approximations on predicted progressive failure in plain weave composites. Composite structures, 34(1), 13-20.
29. Mahadik, Y., & Hallett, S. R. (2011). Effect of fabric compaction and yarn waviness on 3D woven composite compressive properties. Composites Part A: Applied Science and Manufacturing, 42(11), 1592-1600.
30. Yushanov, S. P., & Bogdanovich, A. E. (2000). Fiber waviness in textile composites and its stochastic modeling. Mechanics of Composite materials, 36(4), 297-318.
31. Bolotin, V. V. (1966). Theory of a reinforced layered medium with random initial irregularities. Polymer mechanics, 2(1), 7-11.
32. Tarnopol'skii, Y. M., Portnov, G. G., & Zhigun, I. G. (1967). Effect of fiber curvature on the modulus of elasticity for unidirectional glass-reinforced plastics in tension. Polymer Mechanics, 3(2), 161-166.
33. Bažant, Z. P. (1968). Effect of Curvature of the Reinforcing Fibers on the Moduli of Elasticity and Strength of Composites. Polymer Mechanics, 4(2), 251-258.
34. Lin, K. Y., & Zhang, X. J. (1992). Effect of fiber waviness on the compressive strength of laminated composites. In The Second International Symposium on Composite Materials and Structures(pp. 120-125).
35. Wisnom, M. R. (1990). The effect of fibre misalignment on the compressive strength of unidirectional carbon fibre/epoxy. Composites, 21(5), 403-407.
36. Camponeschi, E. T. (1991). Lamina waviness levels in thick composites and its effect on their compression strength. Composites.
37. Lo, K. H., & Chim, E. M. (1992). Compressive strength of unidirectional composites. Journal of Reinforced Plastics and Composites, 11(8), 838-896.
38. O'Hare Adams, D., & Hyer, M. W. (1993). Effects of layer waviness on the compression strength of thermoplastic composite laminates. Journal of Reinforced Plastics and Composites, 12(4), 414-429.
39. Rai, H. G., Rogers, C. W., & Crane, D. A. (1992). Mechanics of curved fiber composites. Journal of reinforced plastics and composites, 11(5), 552-566.
40. Bogetti, T. A., Gillespie Jr, J. W., & Lamontia, M. A. (1992). Influence of ply waviness on the stiffness and strength reduction on composite laminates. Journal of Thermoplastic Composite Materials, 5(4), 344-369.

41. Bogetti, T. A., Gillespie Jr, J. W., & Lamontia, M. A. (1994). The influence of ply waviness with nonlinear shear on the stiffness and strength reduction of composite laminates. Journal of Thermoplastic Composite Materials, 7(2), 76-90.
42. Chan, W. S., & Wang, J. S. (1994). Influence of fiber waviness on the structural response of composite laminates. Journal of Thermoplastic Composite Materials, 7(3), 243-260.
43. Chan, W. S., & Chou, C. J. (1995). Effects of delamination and ply fiber waviness on effective axial and bending stiffnesses in composite laminates. Composite structures, 30(3), 299-306.
44. Garnich, M. R., & Karami, G. (2005). Localized fiber waviness and implications for failure in unidirectional composites. Journal of composite materials, 39(14), 1225-1245.
45. Hsiao, H. M., & Daniel, I. M. (1996). Effect of fiber waviness on stiffness and strength reduction of unidirectional composites under compressive loading. Composites science and technology, 56(5), 581-593.
46. Hsiao, H. M., & Daniel, I. M. (1996). Nonlinear elastic behavior of unidirectional composites with fiber waviness under compressive loading. Journal of Engineering Materials and Technology, 118(4), 561-570.
47. Hsiao, H. M., & Daniel, I. M. (1996). Elastic properties of composites with fiber waviness. Composites Part A: Applied Science and Manufacturing, 27(10), 931-941.
48. Seon, G. (2009). Finite element-based failure models for carbon/epoxy tape composites (Doctoral dissertation, Georgia Institute of Technology).
49. Nikishkov, Y., Makeev, A., & Seon, G. (2013). Progressive fatigue damage simulation method for composites. International Journal of Fatigue, 48, 266-279.
50. Evans, F. J. (1969). U.S. Patent No. 3,485,706. Washington, DC: U.S. Patent and Trademark Office.
51. Sainsbury-Carter JB. Braided composites: a material form providing low cost fabrication techniques. In: National SAMPE symposium and exhibition (proceedings), vol. 30; 1985. p. 1486–97.
52. Masters, J. E., Naik, R., & Minguet, P. J. (1995). Effects of preform architecture on modulus and strength of 2-D triaxially braided textile composites
53. Minguet, P. (1994, July). A comparison of graphite/epoxy tape laminates and 2-D braided composites mechanical properties. In 36th Structures, Structural Dynamics and Materials Conference (p. 1158).
54. Jackson, W. C., & Portanova, M. A. (1995). Out-of-plane properties.
55. Whitcomb, J., & Srirengan, K. (1996). Effect of various approximations on predicted progressive failure in plain weave composites. Composite structures, 34(1), 13-20.
56. Yushanov, S. P., & Bogdanovich, A. E. (2000). Fiber waviness in textile composites and its stochastic modeling. Mechanics of Composite materials, 36(4), 297-318.
57. Tarnopol'skii, Y. M. (1991). Spatially reinforced composites. CRC Press.
58. Bogdanovich, A., Pastore, C. M., & Pastore, C. (1996). Mechanics of textile and laminated composites: with applications to structural analysis. Springer Science & Business Media.
59. Arumugam, V., Kumar, C. S., Santulli, C., Sarasini, F., & Stanley, A. J. (2013). Identification of failure modes in composites from clustered acoustic emission data using pattern recognition and wavelet transformation. Arabian Journal for Science and Engineering, 38(5), 1087-1102.

60. O'Brien, T. K. (1984). Interlaminar Fracture of Composites (No. NASA-TM-85768). NATIONAL AERONAUTICS AND SPACE ADMINISTRATION HAMPTON VA LANGLEY RESEARCH CEN TER.
61. King, Y. (1991). Delamination analysis of a laminated composite tapered beam. Texas Univ., Arlington, TX (United States).
62. Wilkins, D. J., Eisenmann, J. R., Camin, R. A., Margolis, W. S., & Benson, R. A. (1982). Characterizing delamination growth in graphite-epoxy. In Damage in Composite Materials: Basic Mechanisms, Accumulation, Tolerance, and Characterization. ASTM International.
63. Lagace, P., Brewer, J. O. H. N., & Kassapoglou, C. (1987). The effect of thickness on interlaminar stresses and delamination in straight-edged laminates. Journal of Composites, Technology and Research, 9(3), 81-87.
64. O'Brien, T. K. (1984). Mixed-mode strain-energy-release rate effects on edge delamination of composites. In Effects of defects in composite materials. ASTM International.
65. Wang, A. S. D., & Crossman, F. W. (1977). Some new results on edge effect in symmetric composite laminates. Journal of Composite Materials, 11(1), 92-106.
66. Pipes, R. B., & Pagano, N. J. (1994). Interlaminar stresses in composite laminates under uniform axial extension. In Mechanics of composite materials (pp. 234-245). Springer, Dordrecht.
67. AC09036782, A. (Ed.). (2007). Standard test method for mode I interlaminar fracture toughness of unidirectional fiber-reinforced polymer matrix composites. ASTM Internat..
68. WK22949, A. S. T. M. (2009). New Test Method for Determination of the Mode II Interlaminar Fracture Toughness of Unidirectional Fiber-reinforced Polymer Matrix Composites using the End-notched flexure (ENF) Test. American Society for Testing and Materials, West Conshohocken.
69. Jain, L. K., & Mai, Y. W. (1995). Determination of mode II delamination toughness of stitched laminated composites. Composites Science and Technology, 55(3), 241-253.
70. Massabo, R., & Cox, B. N. (1999). Concepts for bridged mode II delamination cracks. Journal of the Mechanics and Physics of Solids, 47(6), 1265-1300.
71. Massabò, R., Mumm, D. R., & Cox, B. (1998). Characterizing mode II delamination cracks in stitched composites. International Journal of Fracture, 92(1), 1-38.
72. Song, S. J., & Waas, A. M. (1995). Energy-based mechanical model for mixed mode failure of laminated composites. AIAA journal, 33(4), 739-745.
73. Lu, T. J., Xia, Z. C., & Hutchinson, J. W. (1994). Delamination of beams under transverse shear and bending. Materials Science and Engineering: A, 188(1-2), 103-112.
74. Martin, R. H., & Jackson, W. C. (1993). Damage prediction in cross-plied curved composite laminates. In Composite Materials: Fatigue and Fracture, Fourth Volume. ASTM International.
75. Massabò, R., & Cox, B. N. (1999). Bridged Delamination Cracks in Curved Beams and Mixed-Mode Bending Specimens. Proc. ICCM12, Paris.
76. Bruno, D., Carpino, R., Greco, F., & Lonetti, P. (2006). Energy release rate and mode partition for interlaminar crack in circular laminated beams. International journal of solids and structures, 43(5), 1201-1223.
77. Shams, S. (2016). Experimental, Analytical and Numerical Characterization of Effects of Fiber Waviness Defects in Laminated Composites.
78. Chun, H. J. (2002). Evaluation of fiber waviness in thick composites by ultrasonic test. In Recent Advances in Experimental Mechanics (pp. 433-442). Springer, Dordrecht.

79. Chun, H. J., Shin, J. Y., & Daniel, I. M. (2000). Nonlinear behavior of thick composites with uniform fiber waviness. AIAA journal, 38(10), 1949-1955.
80. Ye, T., Jin, G., Ye, X., & Wang, X. (2015). A series solution for the vibrations of composite laminated deep curved beams with general boundaries. Composite Structures, 127, 450-465.
81. González-Cantero, J. M., Graciani, E., Blázquez, A., & París, F. (2014, June). Analytic evaluation of radial stresses in unfolding failure of composite materials. Comparison with numerical solutions. In Proceedings of the 16th European Conference on Composite Materials ECCM16 (pp. 22-26).
82. González Cantero, J. M. (2017). Study of the unfolding failure of curved composite laminates.
83. Abaqus/Standard, V6.14-2, is a trademark of ABAQUS, Inc.
84. Makeev, A., Seon, G., Nikishkov, Y., Nguyen, D., Mathews, P., & Robeson, M. (2015). Analysis Methods for Improving Confidence in Material Qualification for Laminated Composites. Journal of the American Helicopter Society, 64(1), 1-13.
85. Rybicki, E. F., & Kanninen, M. F. (1977). A finite element calculation of stress intensity factors by a modified crack closure integral. Engineering fracture mechanics, 9(4), 931-938.
86. Benzeggagh, M.L. and M. Kenane. 1996. "Measurement of Mixed-Mode Delamination Fracture Toughness of Unidirectional Glass/Epoxy Composites with Mixed-Mode Bending Apparatus." Comp Sci & Tech, 56(4):439-449.
87. Allegri, G., Wisnom, M. R., & Hallett, S. R. (2013). A new semi-empirical law for variable stress-ratio and mixed-mode fatigue delamination growth. Composites Part A: Applied Science and Manufacturing, 48, 192-200.
88. Vasiliev, V. V. and R. M., Jones. Chapter 4 in Mechanics of Composite Structures, Taylor & Francis, Washington, DC, 1993.
89. Barbero, E.J. Chapter 8 in Introduction to Composite Materials Design, Taylor & Francis, Washington, DC., 1998.
90. Kollar, L. P. and G. S. Springer. Chapter 8 in Mechanics of Composite Structures, Cambridge University Press, UK, 2003.
91. Liberscu, L. and O. Song. Thin-Walled Composite Beams-Theory and Application, Springer, the Netherlands, 2006.
92. Hodges, D. Nonlinear Analysis of Composite Structures, Cambridge University Press, UK, 2008.
93. Wu, X.-X. and C. T. Sun. “Simplified Theory for Composite Thin-Walled Beams’ AIAA Journal, 1992. Vol. 30, No. 12, pp 2945-2951.
94. Yu, W., D. H. Hodges, V. V. Volovoi, and D. F. Eduardo. "A Generalized Vlasov Theory of Composite Beams," Thin-Walled Structures, vol. 43, no. 9, pp.1493-1511. 2005.
95. Yu, W.. J. C. Ho, and D. H. Hodges. "Variational Asymptotic Beam Sectional Analysis -- An Updated Version," International Journal of Engineering Science, vol. 59, pp. 40-64. 2012.
96. Drummond, J. A., and W. S. Chan. “Fabrication, Analysis, and Experimentation of a Practically Constructed Laminated Composite I-Beam under Pure Bending”, Journal of Thermoplastic Composite Materials, May Issue, pp. 177-187. 1999
97. Jung, S. N., and J. Y. Lee.“Closed-form Analysis of Thin-walled Composite I-beams Considering Non-classical Effects”, Composite Structures Vol.60, 2003, pp. 9–17. 2003.
98. Rios, G. and W.S. Chan.“A Unified Analysis of Stiffener Reinforced Composite Beams”, 25th Annual Technical Conference of American Society for Composites. 2010.

99. Parambil, J.C., W.S. Chan., K.L. Lawrence, V. Sanghai."Stress Analysis of Composite I-Beam by a Non –Conventional Method", Proceedings of the American Society for Composites 26th Technical Conference, paper No. 1027. 2011.
100. Sanghai, V. and W.S. Chan. "Torsional Analysis of a Composite I-Beam", Proceedings of the American Society for Composites 28th Technical Conference. 2013.
101. Syed, K. A., and W. S. Chan. September 2006. "Analysis of Hat-Sectioned Reinforced Composite Beams", Proceedings of the 28th Technical Conference of American Society for Composites, Paper No. 1055.
102. T.H.G. Megson, Aircraft Structures for engineering students, Third edition, Butterworth Heinemann publications, 1999.
103. https://www.fxsolver.com/browse/formulas/Torsion+constant+%28Rectangle%29
104. Walter D. Pilkey and K. Kevent. "Notes on the Linear Analysis of Thins-walled Beams". University of Virginia, 1996.
105. Robert L. Ketter, George C. Lee and Sherwood P. Prawel, Jr., Structural Analysis and design, McGraw-Hill Inc, 1979
106. Singh, S."A Novel Stress Analysis Method For Laminated Composite Stiffener With Asymmetric Z-Section Under Mechanical And Thermal Loading Conditions", Master thesis of Aerospace Engineering program, Department of Mechanical and Aerospace Engineering, The University of Texas at Arlington. 2016.
107. Lu, W. T., Singh, S., & Chan, W. S. (2019). A novel stress analysis method for composite Z-stiffeners under mechanical and thermal loads. Journal of Composite Materials, 0021998319846947.
108. Sanghavi, V. M. S. (2013). Torsional Analysis of a Composite I-beam.
109. Kollár, L. P., & Springer, G. S. (2003). Mechanics of composite structures.
110. ANSYS Academic Research, Release 17.2. 2017: Canonsburg, Pennsylvania Cambridge university press.
111. Lu, W. T. "Effects Of Transverse Shear Deformation On Composite Beams With Various Laminate Configurations And Boundary Conditions". Master thesis of Aerospace Engineering program, Department of Mechanical and Aerospace Engineering, The University of Texas at Arlington. 2015
112. Gl´aucio C. Pereira , P. Leboulluec , W. T. Lu , M. I. Yoshida, Ana P. Alves and Antˆonio. F. Avila. "Spring-Back Behavior on L-shaped Composite Structures: a statistical analysis of angular recovery as a function of time and residual cure", Composites Part A: Applied Science and Manufacturing.